APPLICATION OF IMPROVED CORE LOSS FORMULATIONS TO MACHINE DESIGN

UNIVERSITY OF CAPE TOWN

A Dissertation

BY

Mr. Marubini J. Manyage

Doctor of Philosophy
Department of Electrical Engineering

Supervisor

Professor Pragasen Pillay

Department of Electrical Engineering

Thesis prepared in fulfillment of the requirements for Doctoral degree in Electrical Engineering at the University of Cape Town.

June 2008

DECLARATION

I hereby:

(a) Grant the University free license to reproduce the above thesis in the whole or part, for the purpose of research.

(b) Declare that:

(i) The above thesis is my own unaided work, both in conception and execution, and that apart from the normal guidance of my supervisor, I have received no assistance.

(ii) Neither the substance nor any part of the thesis has been submitted in the past, or is being, or is to be submitted for a degree in the University or any other University.

Signature:..... Date:.....

Marubini J. Manyage

ACKNOWLEDGEMENTS

All thanks to the Almighty God, by His grace I made it through each day. I would like to gratefully acknowledge the enthusiastic supervision and guidance of Professor Pragasen Pillay throughout the project. He provided me with international exposure and introduced me to the best people in the field. My sincere thanks to my lovely wife, Julia, for her love, emotional support, encouragement and sacrifice. My two daughters, Phathutshedzo and Tshilidzi, all born during this period, put a smile on my face everyday and I dedicate this thesis to them. I am most indebted to my parents, Azwidohwi and Ntshengedzeni Manyage and my grandmother, Vho-Emma Manyage, for their understanding, prayers and encouragements after leaving work to pursue my PhD degree full time. I am also grateful to my sisters, Tshilidzi, Livhuwani, Tendani, Emma, and my brothers, Tshidaho, Thisikhawe, Lesley, Hulisani and Mulalo for their love and support.

Many thanks to my colleagues and friends; Dr. T. L. Mthombeni, Dr. A. Khan, Dr. P. Barendse, Dr. A.B Sebitosi, Dr. H. Douglas, Dr. A. Gebrigergis, Dr. T. Surgevil, Dr. R. Naidoo, Mr. L Dosiek, Dr. H. Li, Mr. Yu Zhang, Ms. K. Masemola, Ms. M. Maunye, Mr. B. Enayathi, Mr. Y. Tsegay, Dr. R. Batane, Mr. P. Mudau, Mr. M. Munzhelele, Mr. R Khumeleni, Mr. K. Maphodo, Mr. T. Munonde, Mr. M. Ratshikuni, Mr. P. Booi and many more.

The PhD research work was funded by the South African Electricity Supply Commission (ESKOM) and the National Research Funding (NRF) through the University of Cape Town postgraduate funding office. I would also like to thank Mrs. L. Rossow, Mrs. L. Vranas, Mrs. M. Joubert, Mrs. N. Moodley, Mrs. B.J Cecot and Mrs. K. Kelly for taking care of the administrative work.

ABSTRACT

The electrical energy consumed by electrical machines constitutes the largest % of the total electrical energy produced in South Africa. As the world embarks on strategies to reduce emissions, one initiative with significant impact is to investigate the potential efficiency gains by improving electrical machine efficiencies in the design process. The efficiency is improved by accurate quantification and minimization of all the loss components (winding, core and mechanical losses) in the motor. The winding losses are easy to quantify whereas core losses are still a subject of intense interest in both measurements and modeling stages. The core loss is the second dominant loss component, and has a direct impact on motor efficiency and sizing. The primary focus of this thesis is in core loss measurement and modeling techniques and their impact in machine design.

In practice, steel manufacturers usually supply core loss data either at 50/60Hz, 1.5T or curves (core loss vs. flux density) at 50 and/or 60Hz. There is growing need for lamination characterization at high flux densities (2T) and high frequencies (3.2 kHz) for novel electric machine designs operating at high speeds. The core loss measurement concept is reviewed first. Two core loss measurement formulae are compared using core loss results from different testing frames and materials. A new 200-turn non-traditional Epstein frame has been developed and measures losses at high frequencies and high flux densities with acceptable accuracy, surpassing the standard 352-turn frame and the recently developed 280-turn frame capabilities.

The Epstein, Toroid and Single Sheet Tester (SST) test frames are also compared using the new commercial Donart system and the advanced laboratory test bench system. The SST core loss results are averaged for comparison with Epstein results. The core loss results measured from small unannealed toroidal fixtures are higher than the standard Epstein, a representation of the practical situation in motor design. Better correlation with standard Epstein is observed with the large toroid. The effects of

laminations configuration, annealing and core loss correction factors on core loss measurements are also addressed.

The impact of the availability and accuracy of measured core loss data on core loss models is examined. A detailed description and analysis of conventional core loss models used in design softwares are presented. The original Steinmetz and classical formulae predict the same core losses provided the loss coefficients are recalculated at each frequency of concern. The skin effect must be accounted for when using classical formula at high frequencies. The Steinmetz's constant, n=1.6, is not generically applicable to all materials. The modified Steinmetz model (used in SPEED PCBDC) does not necessary predicts better results that the original Steinmetz's formula, especially at high flux densities - contrary to what is expected. Berttoti's formula (used in Flux2D) shows improvement when compared to the classical model, especially when estimation is done with limited loss data. However, Bertotti's formula still under estimates losses at high flux densities. Also, the formula is invalid at high frequencies. The improved model performs better than all the models under both sinusoidal and non-sinusoidal excitations.

The applicability and accuracy of the improved core loss model are examined in electrical machines. The new model shows good alignment with experimental data from the induction motor and toroid frame. An alternative method of calculating core losses without using the formulae is also presented and tested in electrical machines with acceptable accuracy.

Three software packages are compared in the design of a Low Voltage High Current Permanent Magnet Synchronous traction motor. The core loss model used in the PCBDC software under estimates core losses during load conditions in salient pole machines. The core losses and back EMF are affected by skewing and temperature. The manufacturing of the laminations and core assembly techniques affect the core loss results and there are no generic scaling factors. The procedure to integrate the new formula into Flux2D is highlighted.

TABLE OF CONTENTS

LIST OF FIGURES

CHAPTER 2:

CHAPTER 3:

CHAPTER 4:

CHAPTER 5

LIST OF TABLES

NOMENCLATURE

ASTM	:	American Society of Testing and Materials
EMERF	:	Electric Motor Education and Research Foundation Consortium
EMF	:	Electro Motive Force
FE	:	Finite Element
FEA	:	Finite Element Analysis
MATLAB	:	Matrix laboratory
PCBDC	:	PC Brushless Direct Current software
PMSM	:	Permanent Magnet Synchronous Motor
rms	:	Root Mean Square
SMMA	:	The Motor and Motion Association
SPEED	:	Scottish Power Electronics and Electric Drives
SST	:	Single Sheet Tester
%FF	:	Percentage Form Factor

Chapter 1

1. INTRODUCTION

1.1 RESEARCH BACKGROUND

The electrical energy consumed by electrical machines constitutes the largest % of the total electrical energy produced in developed or developing countries. For example, the South African industrial sector accounts for 47% of the total energy with an estimate of 64% of the total electrical energy being consumed by industrial motorized applications [36]. Similar energy estimates has been reported in the US. The electrical energy in South Africa is derived mainly from coal and it is expected to increase as the country develops even further, and in turn increase the CO_2 emissions. As the world embarks on strategies to reduce emissions, one initiative with significant impact is to investigate the potential efficiency gains by improving electrical machine efficiencies in the design process. A 1% increase in efficiency of machine has a huge impact on energy savings and emission reduction.

The electrical motor efficiency is improved by accurate quantification and minimization of all the loss components in the motor. The major losses are winding and core losses in addition to mechanical losses. The winding losses are easy to quantify under both sinusoidal and non-sinusoidal supplies whereas core losses are still a subject of intense interest in both measurements and prediction/modeling stages [4]-[26] [29]-[31]. The core loss is the second dominant loss component and in some cases higher than the winding losses; it therefore has a direct impact on motor efficiency and sizing. The primary focus of this thesis is in core loss measurement and modeling techniques and their impact in machine design.

1.1.1 Core Loss Measurement

The three test frames that are used to measure core losses in electrical steels are the Epstein, Toroid and Single Sheet Tester (SST). The Epstein

frame is the most common and well accepted by the steel manufacturers. One of the advantages is that it allows various laminations to be tested quickly without modifying the frame unlike when using a Toroid. Some machine designers are however in favor of the toroidal frame since its shape resembles that of the motor laminations. The SST is the least common used since its results are calibrated by the Epstein frame results. The American Society of Testing and Materials (ASTM) [4] has standardized these frames with detailed description of the frame and test sample sizes but made no distinction of the preferred method. Moreover, the core loss test results are not included in the standard in order to clarify the differences and the impact of these methods of testing.

In practice, steel manufactures and/or distributors usually supply core loss data either at 50/60Hz, 1.5T or curves (core loss vs. flux density) at 50 and/or 60Hz. The loss data are measured when the material is subjected to sinusoidal flux density waveforms using the industrial standard 700-turn or 352-turn Epstein frames. This is because the motor (yoke and teeth) and transformer cores operate around these points (50/60Hz, 1.5T) with sinusoidal supplies. The development of the core loss models are also limited to low frequency applications [1] [2] [3] [10]. Furthermore, recent machines have non-sinusoidal flux densities in the core, which add additional complications to the old models and result to sub-optimised design.

There is growing need for lamination characterization at high frequencies and high flux densities for novel electric machine designs operating at high speeds. For example, the magnitude of 2T, 3.2 kHz has been of interest by the Electric Motor Education and Research Foundation Consortium (EMERF) of the Motor and Motion Association (SMMA). Therefore, test frames capable of core loss measurements at high frequencies and high flux densities have to be developed and tested. A 280-turn Epstein frame has been developed recently and the test results are presented in [6]. Various materials have

been tested at frequencies up 1kHz [6]. The benefits are 1). reduced lamination preparation time as it accommodates only one lamination per side and 2). low voltage requirement in order to achieve high flux densities and frequencies. The core loss measurements are extended from 1 kHz to 6 kHz using the same 280-turn frame in this thesis. A new small 200-turn non-traditional Epstein frame capable of achieving core loss measurements at high frequencies and high flux densities has been developed. The comparison between the various Epstein frames is made and reported in this thesis.

The test frames (Epstein, Toroid and SST) discussed above are components of the core loss measurement system/equipment. A new commercial state of the art core loss measuring equipment, which has not being used before, is used to measure core losses with various frames. The equipment has been provided by the Donart Company and is capable of measuring high flux densities at frequency ranges from 20Hz to 4kHz with sinusoidal excitations. Lamination testing under non-sinusoidal excitations is of interest since the motor flux density waveforms are hardly sinusoidal (e.g. Permanent magnet motor, switch reluctance motor and any saturated machine). An advanced laboratory testing equipment capable of measuring core losses from any arbitrary waveform and frequency (within limits) has been developed and is presented here. Its control is flexible and allows non-sinusoidal core loss testing thereby surpassing the commercial test systems, which are limited to sinusoidal excitations only.

1.1.2. Core Loss Modeling

In the design of electric machines, predicting core losses has always been a difficult task. Various core loss models have been developed based on the work of Steinmetz [1] [3] [12] [13] [19] [21]. The Steinmetz's initial model has been developed based on the phenomenological principle known as loss separation; hence it is composed of two terms, which are the hysteresis and eddy current loss components [1]. The model has been developed by curve fitting the experimental data and is in the form of

$$\overline{P} = k_h B_p{}^n f + k_e B_p{}^2 f^2 \tag{1.1}$$

where $\overline{P}$ is the average loss per unit mass at frequency f and peak flux density B_p, n is the Steinmetz's constant, k_h and k_e are hysteresis and eddy current loss constant coefficients respectively.

Another two-term model with physical basis was developed where the eddy current coefficient is material dependent [2]. The model was later improved to a three-term model developed by Bertotti [2]. A third term known as excess loss was introduced. The origin was determined based on the domain wall theory and this loss component was due to inhomogeneous flux density inside the material. The model is in the form of

$$\overline{P} = k_h B_p{}^2 f + \frac{\sigma \pi^2 d^2}{6\rho} B_p{}^2 f^2 + k_{ex} B_p{}^{1.5} f^{1.5} \tag{1.2}$$

where k_{ex} is the excess loss constant coefficient, which depend on material intrinsic parameter and dimensions. The model was tested up to 100Hz and was not expected to work for all materials and frequencies [10].

Since then, many core loss models have been developed and refined [11]-[14] [18]-[21]. In some models, loss coefficients vary with flux density or frequency or both. The core loss data used are for materials subjected to sinusoidal flux density waveforms. Based on the number of research papers produced, it is clear that mathematically, a large number of core loss models can be developed. Although, good results are obtained from these models, they lack a physical basis to explain the variation of loss coefficients. Most of these models are tested for sinusoidal flux waveform cases only using one or two materials and therefore lack wide representation of the model. To calculate core losses under non-sinusoidal flux densities, the Fourier series technique is used in these models.

1.2 PURPOSE OF THIS THESIS

A new model which has a physical basis for the variation of loss coefficients with alternating flux density and/or frequency has been developed by Lotten [7] using the laboratory test bench results. The purpose of this thesis is to examine the applicability and accuracy of the new model using the recent core loss results from the new testing equipment and frames. The model is tested in induction and permanent magnet synchronous machines.

1.3 THESIS OBJECTIVES

The objectives of this thesis are:

- To characterize laminations at high frequencies and high flux densities using the new Epstein frame. To compare the Epstein, Toroid and Single Sheet Tester (SST) core loss test frames in order to determine their impact on core loss measurement and modeling.

- To provide a detailed description and comparison of conventional core loss models used in SPEED PCBDC and Flux2D softwares using the new testing equipment and various materials.

- To examine the applicability and accuracy of the new core formula in the design of induction machines and permanent magnet machines.

- To compare three machine design softwares in the permanent magnet traction motor design with stringent requirements. To propose a strategy to integrate the new formula into Flux2D Software.

1.4 CONTRIBUTION OF THIS THESIS

The contributions of this thesis are:

- Examination of the applicability and accuracy of the new core loss formula using recent core loss results at low and high frequencies,

sinusoidal and non-sinusoidal excitations. The model is tested in toroids, induction and permanent magnet synchronous machines.

- Development of an alternative method of core loss prediction in machine design without using the core loss formulae.

- Design and analysis of a Low Voltage High Current traction motor with stringent requirements.

1.5 THESIS OUTLINE

The brief description of each chapter:

Chapter 2: Description of the core loss measurement concept. Comparative study of the test frames and testing equipment. Analysis of the effect of frame and sample configuration on core loss measurements.

Chapter 3: A full description and comparison of old and recent core loss models. Development and testing of new core loss formula using resent core loss results at low and high frequencies, sinusoidal and non-sinusoidal excitations.

Chapter 4: Application of the improved model in induction machines and PM synchronous machines. Development of an alternative method of core loss prediction in machine design without using the core loss formulae.

Chapter 5: PM synchronous machine design using different sofwares and integration of new formula into Magsoft Flux2D

Chapter 6: Conclusions and Recommendations

Chapter 2

2. CORE LOSS MEASUREMENTS

2.1 OVERVIEW

The availability and accuracy of measured core loss data using an Epstein, Toroid or Single Sheet Tester (SST) have a direct impact on loss calculation, heating and motor efficiency. The purpose of this chapter is to compare the three core loss test frames and equipment, and to characterize laminations at high frequencies and high flux densities using the new Epstein frame. The core loss measurement concept is discussed first together with the comparison of two measurement formulae. Then, two new core loss testing equipment are described and compared. A new 200-turn non-standard high frequency Epstein frame is presented and compared with the commercial 352-turn and recently developed 280-turn frames. The core loss results obtained from the Epstein, Toroidal and SST testing fixtures are also compared and analyzed. Finally the effects of strips or laminations configuration, preparation, arrangement, annealing and core loss correction factors are addressed.

2.2 CORE LOSS MEASUREMENT CONCEPT

It has been found as early as 1890's [1] through experiments that when an applied magnetic field H_a is cycled in a magnetic material, energy is converted to heat and sound due to the magnetic hysteresis of the material. The hysteresis phenomenon is best described by a four-quadrant hysteresis loop in Figure 2.1, also known as the BH loop; where the area inside the loop represents the energy loss per cycle [2] [3].

Different types of material have different shapes of hysteresis loop but the overall energy per cycle (W.s/cycle) per unit volume, E_{loop} , is given by

$$E_{loop} = \oint H_a dB \qquad (2.1)$$

Therefore, the power loss or core loss in watts per unit volume, P_c, will be

$$P_c = f \oint H_a dB \tag{2.2}$$

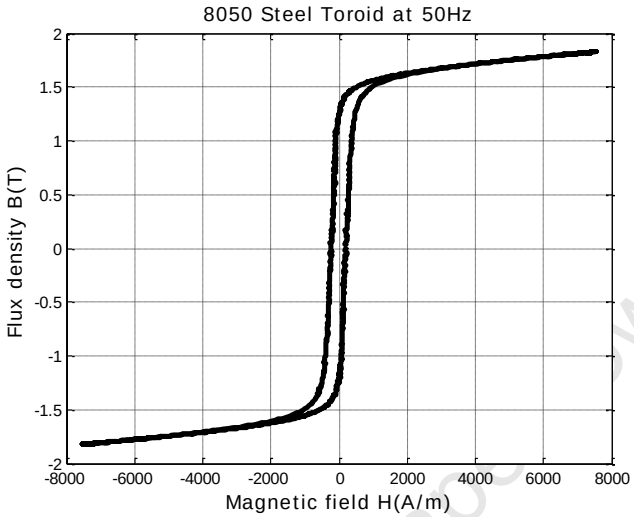

Fig. 2.1 AC Hysteresis Loop of a 8050 steel at 50Hz

where B is the alternating flux density observed over one electrical cycle of frequency f. The core loss formula (2.2) represents the total loss in a material, that is, it includes hysteresis, eddy current and excess losses [2]. Therefore, hysteresis losses should not be confused with the hysteresis loop in Figure 2.1. The loss measurement concept is based on the transformer-like electromagnetic circuit shown in Figure 2.2. The circuit is used in Epstein, Toroidal and SST test frames.

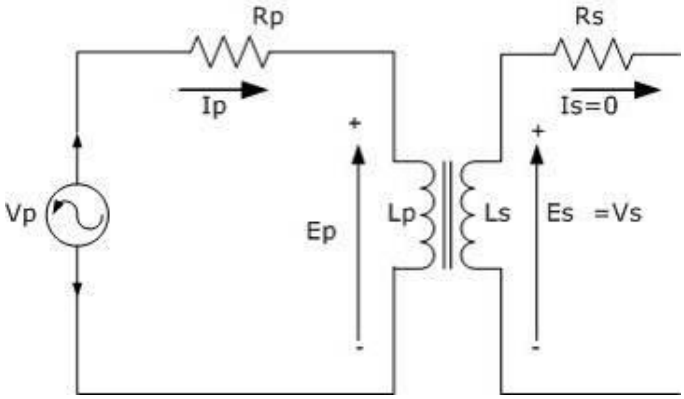

Fig. 2.2 Core loss measurement electromagnetic circuit

V_p, I_p, E_p, R_p and L_p are primary voltage, current, back *EMF (*all in *rms)*, resistance and inductance respectively*.* E_s, V_s, i_s, R_s and L_s are secondary voltages, current, winding resistance and inductance respectively.

Commercial hysteresisgraphs are available, that calculate the applied magnetic field H_a from the instantaneous primary current $i_p(t)$ and average flux density B from secondary voltage $v_s(t)$ and then calculates the area of the hysteresis loop and the subsequent core loss using (2.2). However, the standardized method by the American Society of Testing and Material (ASTM) [4] is the wattmeter method, where $i_p(t)$ and $v_s(t)$ are measured and the average power, $\overline{P}$, is given by

$$\overline{P} = \frac{1}{T}\int i_p(t)\cdot v_s(t)dt \qquad (2.3)$$

Equation (2.3) represents core losses in the material provided that the secondary current I_s = 0. Equations (2.2) and (2.3) are compared using the Epstein and Toroidal test frames for different materials at different frequencies. Both equations yield similar results as indicated by the relative error in Table 2.1, however, (2.3) is easier to compute than (2.2), hence its popularity. Equation (2.3) is used in the core loss measurements reported in this thesis.

Table 2.1 Comparison of core loss measurement formulae

8050 Steel at 50Hz (Toroid)				**M36_26G at 60Hz (Epstein)**				**M19_29G at 4kHz (Epstein)**			
B	HdB	VIdt	error	B	HdB	VIdt	error	B	HdB	VIdt	error
(T)	(W/kg)	(W/kg)	(%)	(T)	(W/kg)	(W/kg)	(%)	(T)	(W/kg)	(W/kg)	(%)
0.20	0.21	0.21	0.19	0.20	0.10	0.10	-0.50	0.18	34	34	0.00
0.40	0.74	0.75	0.07	0.30	0.21	0.21	-0.34	0.40	147	148	0.68
0.80	2.29	2.29	0.02	0.50	0.50	0.50	-0.34	0.80	628	632	0.55
1.00	3.24	3.24	-0.01	0.60	0.68	0.67	-0.30	1.02	1122	1123	0.16
1.20	4.46	4.46	0.08	0.70	0.88	0.88	-0.30	1.22	1784	1784	0.01
1.55	7.28	7.29	0.14	0.90	1.37	1.37	-0.25	1.44	2930	2927	-0.09
1.71	8.96	8.99	0.28	1.30	2.73	2.72	-0.34	1.72	5693	5682	-0.20
1.72	9.09	9.11	0.26	1.40	3.28	3.27	-0.35	-	-	-	-
1.80	9.79	9.82	0.34	1.60	5.12	5.05	-1.27	-	-	-	-
1.83	10.13	10.17	0.36	1.70	6.34	6.27	-1.14	-	-	-	-

2.3 CORE LOSS MEASUREMENT EQUIPMENT

Two core loss testing equipment are used during the core loss measurement and analysis process. The description, capabilities and comparison of the two systems are given below.

2.3.1 Donart System

The Donart system in Figure 2.3 is the new commercial computerized equipment capable of automatic core loss measurement at low and high flux densities and wide frequency range. It consists of a signal generator, AE Techron amplifier, computer, controller, current/voltage measurement outputs and three test frames (Epstein, Toroid and Single Sheet Tester).

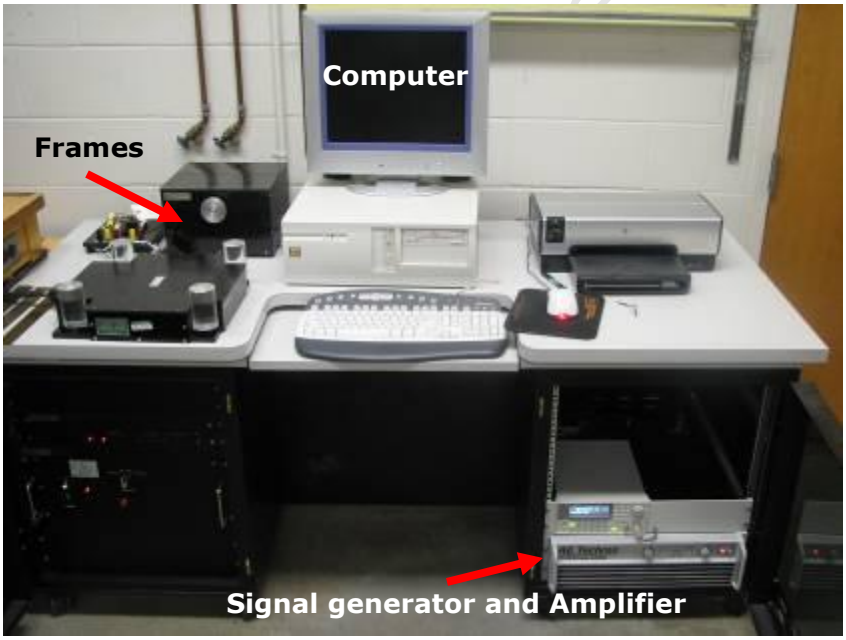

Fig. 2.3 Donart testing equipment

The Donart system core loss measurement is based on the ASTM standard [4], thus adopting the ASTM schematic in Figure 2.4 but with modern instrumentation. Its drive capability is limited at 120V, 15A with a signal generator with frequency range from 20Hz to 4kHz. AC Hysteresis

loops as shown in Figure 2.1 are possible from 20Hz to 400Hz. The Donart system accommodates three test frames addressed next.

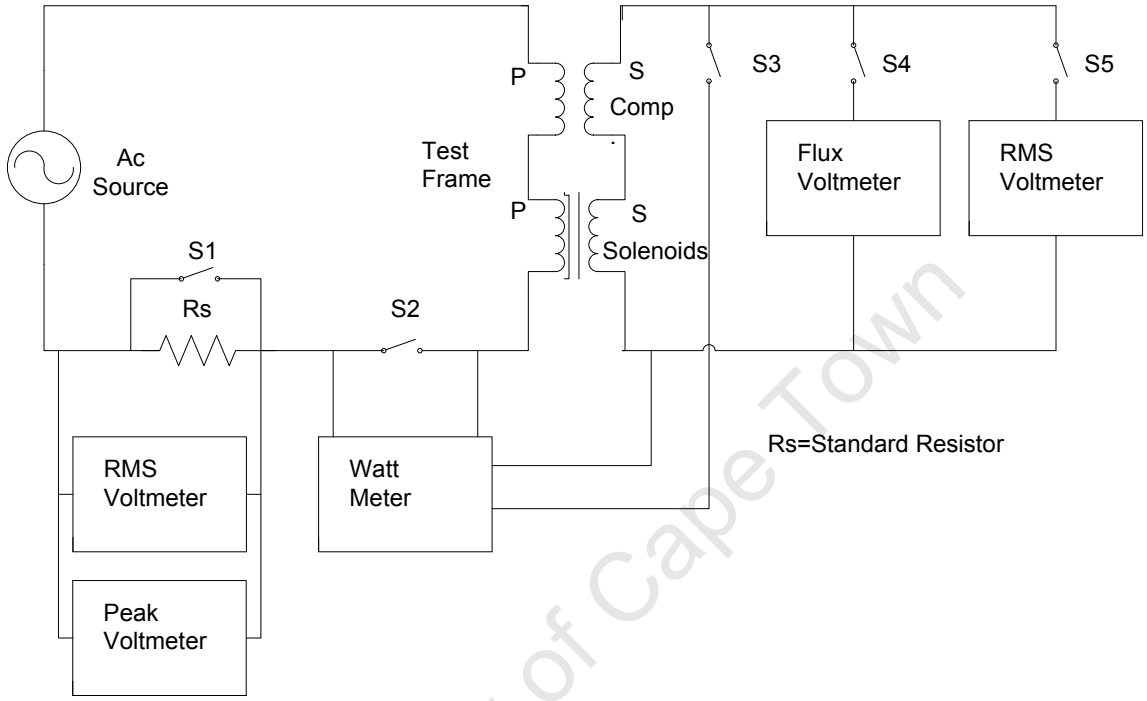

Fig. 2.4 ASTM Schematic for core loss measurement [4]

A. Standard Epstein Frame

An industrial standard Epstein frame is usually a 25-cm, four-sided frame, with equal winding turns on each side as shown in Figures 2.5a and 2.6a. The primary and secondary windings have the same number of turns. The frame magnetic path length is approximated to be 94-cm [4] [5]. Test samples or strips are cut to dimensions regulated by the ASTM standards and inserted in each side/limp of the frame. The strips must be of multiples of four and overlap each other at the end as shown in Figure 2.6b. The Epstein frame is the most common and well accepted by lamination producers and design engineers despite lack of uniformity of magnetization at the corners and path length [5].

The Donart system allows testing using the commercial 700-turn frame from 20Hz to 400Hz with maximum of 64 strips and the 352-turn frame from 20Hz to 4kHz with a maximum of 24 strips. Other frame sizes can only be tested after reprogramming the system internal control software.

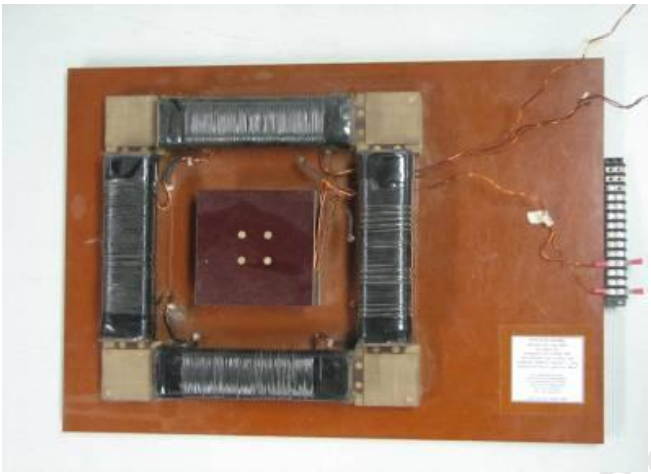

Fig. 2.5a 700-turn Epstein frame

Fig. 2.5b 30.5cm long, 3cm wide strip

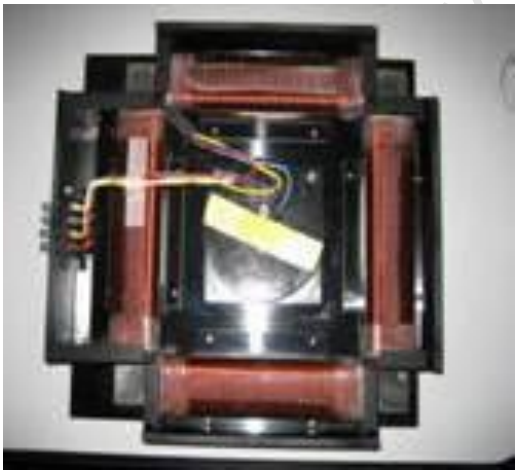

Fig. 2.6a 352-turn Epstein frame

Fig. 2.6b Strips lapped joints, 5 per limp

B. Toroid Frame

Toroidal laminations are continuous with no airgaps unlike the Epstein frame as shown in Figure 2.7b. The shape resembles motor laminations and favored

by some motor designers. The Donart system allows small toroidal samples with 120/120 or 240/240-turns or some other combination of this to be connected to the frame with capabilities from 20Hz to 4kHz.

Fig. 2.7a Toroid frame and test sample

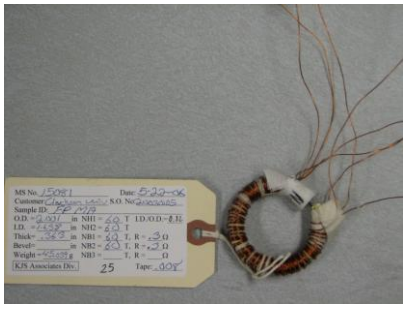

Fig. 2.7b Toroidal sample

C. Single Sheet Tester

The Single Sheet Tester (SST) in Figure 2.8 consists of a single strip and a core to complete the magnetic circuit. This method requires less sample mass, reducing sample preparation time, however, its results are calibrated by the Epstein frame results. Also, the test material does not represent the test steel well since only one strip is tested. The Donart system allows testing of the SST from 20Hz to 400Hz.

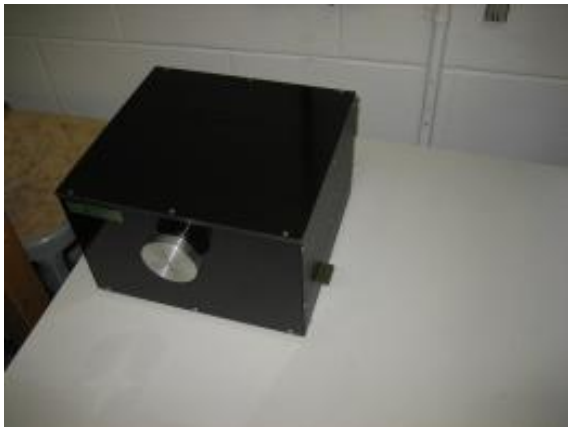

Fig. 2.8 Single Sheet Tester (SST) and test sample

2.3.2 Test Bench System

The test bench system in Figure 2.9 is a powerful testing equipment capable of measuring core losses with any arbitrary waveforms and frequencies (within limits). Its control is flexible and allows non-sinusoidal core loss testing thereby surpassing the commercial test systems, which are limited to sinusoidal excitations only. It consists of computer with dSpace board (DS1104), AE Techron high bandwith linear amplifier and measuring instruments (DL750 scope and wattmeter).

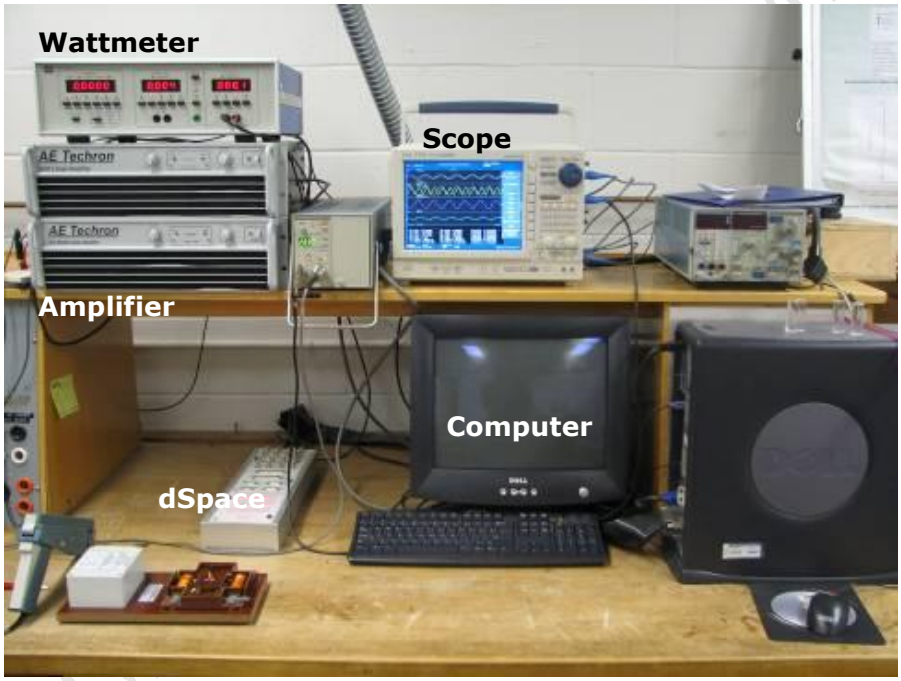

Fig. 2.9 Test bench testing equipment

The diagram in Figure 2.10 shows the test bench system connection more clearly. Signals are generated in MATLAB\Simulink interfaced with dSPACE for real-time control, and applied to the frame under test (Epstein or Toroid). All the test frames discussed above can be used together with the newly developed high frequency 280-turn and 200-turn Epstein frames in Figures 2.11a and 2.12a. The description and the need for high frequency Epstein frames are discussed next and the comparison of the Epstein frames is made in section 2.4.

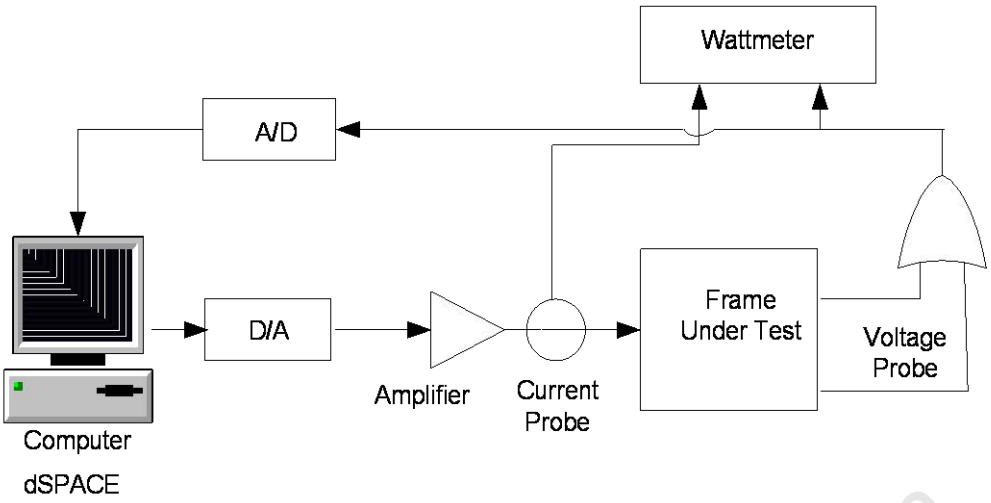

Fig. 2.10 Test bench schematic

2.3.3 High Frequency Epstein Frames Description

There is growing need for lamination characterization at high frequencies and high flux densities for novel designs. The magnitude of 2T, 3.2kHz has been of interest by the Electric Motor Education and Research Foundation Consortium (EMERF) of the Motor and Motion Association (SMMA). The EMERF group developed a 280-turn 25-cm frame with a maximum of one strip per limp/side as shown in Figures 2.11a and 2.11b [5]. The benefits are; the reduction of sample preparation time and reduced voltage requirement to reach high flux densities. The frame has been tested up to 1kHz in [6]. Further testing up to 6kHz is done and reported in section 2.4.

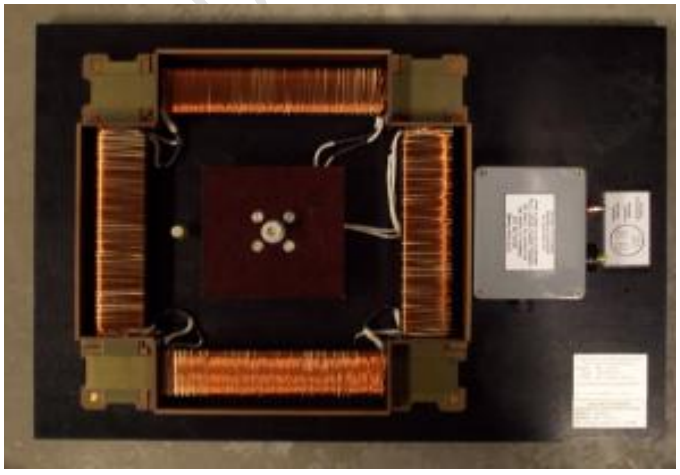

Fig. 2.11a 280-turn Epstein frame

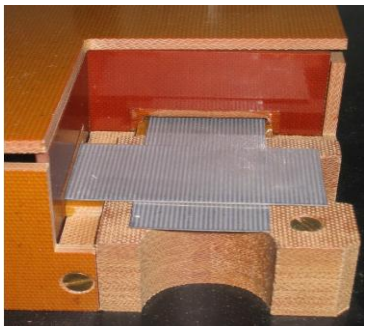

Fig. 2.11b One strip per limb

A new 200-turn non-traditional Epstein frame with 30.5-cm path length instead of the standard 94-cm has been developed as shown Figure 2.12. The ASTM has standardized the 100-turn and 200-turn frames at 94-cm for high frequency use although no lamination manufacturer claims to own one [4] [7].

Fig. 2.12a 200-turn Epstein frame

Fig. 2.12b Three strips per limb

The design philosophy of the new frame is based on the circuit in Figure 2.2 and Faraday's law of induction given by

$$v_s(t) = N_s A \frac{dB(t)}{dt} \tag{2.3}$$

Where $v_s(t)$ is the instantaneous secondary voltage, N_s is the number secondary turns and A is the area of the sample. Core loss measurements are usually performed when a material is subjected to sinusoidal flux density waveforms in order to compared different types of materials. Assuming a sinusoidal flux density waveform

$$B(t) = B_p \sin(2\pi ft) \tag{2.4}$$

and substituting its derivative into (2.3) result in another sinusoidal waveform given by

$$v_s(t) = N_s A 2\pi f B_p \cos(2\pi ft)\ . \tag{2.5}$$

The *rms* secondary voltage V_s from (2.5) is given by

$$V_s = \sqrt{2}\pi N_s A f B_p \tag{2.6}$$

In order to test a material at frequency *f,* the desired peak flux density B_p values are chosen from 0.1 to 2T or higher. The *rms* voltage V_s is required at the secondary terminals to achieve the predetermined B_p. Furthermore, V_s determines the required excitation or primary voltage of the frame. Testing at high frequencies and flux densities requires high voltage as indicated in (2.6). The voltage requirement can be reduced by optimizing the number of turns and the area of the sample. It this case, the number of turns is reduced to 200 instead of the normal 352, and laminations are made smaller to represent small geometries. The new frame has a technical advantage over the other frames. The frame was manufactured by KJS Associates Company.

The physical size of the new frame and test samples are much smaller when compared to the standard frame as shown in Figure 2.13. The test results of this new frame in comparison with the 280-turn and 352−turn are reported in section 2.4.

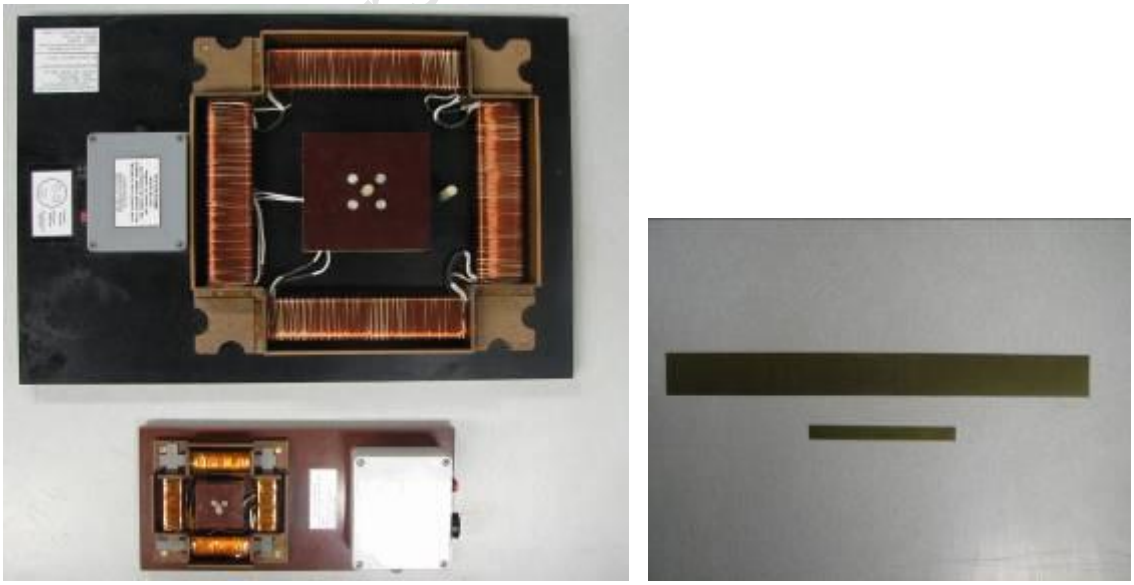

Fig. 2.13 Comparison of the frames and sample physical sizes

2.3.4 Donart System and Test Bench Comparison

The two systems are compared using different materials, frames and frequencies. Figures 2.14 – 2.16 show the results obtained using M19_29 Gauge steel and M36_36 Gauge steel, with frequencies as high as 4kHz. Good correlation with average deviation below 5% has been observed in several materials tested. Slight deviations can be expected since the two systems are not identical. The Test bench is capable of reaching higher flux densities at high frequencies than possible with commercial frame as shown in Figure 2.16.

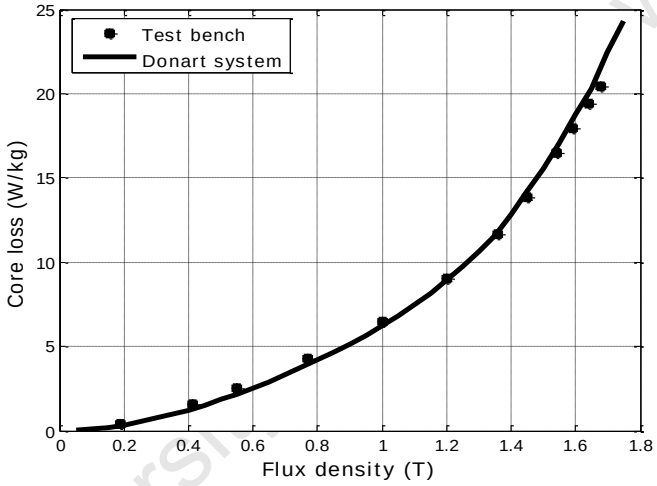

Fig. 2.14 Donart and Test bench comparison: Epstein M19_29G at 200Hz

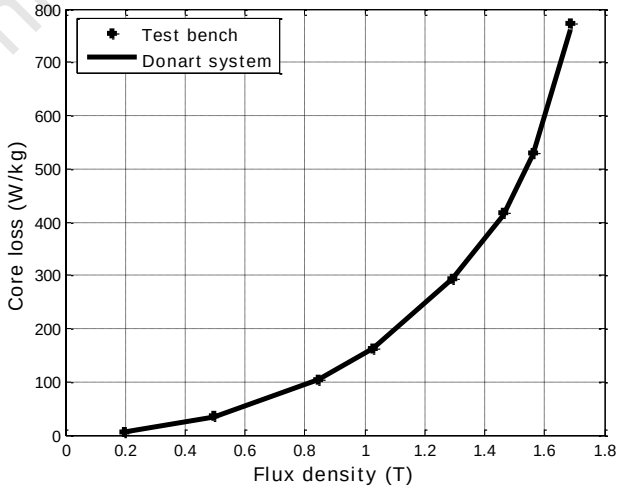

Fig. 2.15 Donart and Test bench comparison: Epstein M36_26G at 1kHz

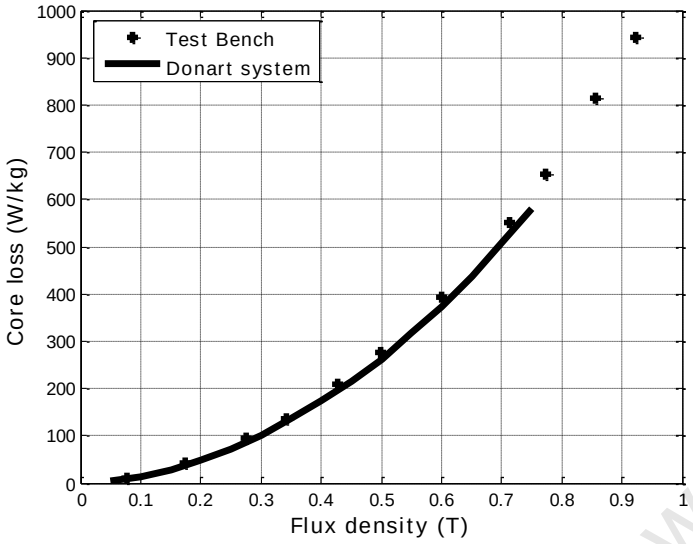

Fig. 2.16 Donart and Test bench comparison: Toroid M19_29G at 4kHz

2.4 HIGH FREQUENCY EPSTEIN FRAMES COMPARISON

The recent development of the new non-traditional 200-turn Epstein frame in Figure 2.12a for high frequency and high flux density core loss measurements has allowed a comparative study with the standard 352-turn commercial frame and the EMERF 280-turn frame. Before the comparative results are presented, the effect of the number of strips is discussed. The tests are performed using the laboratory Test bench system since the Donart system is not programmed to accept the 200-turn and 280-turn non-standard frames.

2.4.1 Effect of number of strips: 200-turn Frame

The 200-turn Epstein frame accommodates a maximum of 3 strips per side therefore a set of 4, 8 and 12 strips are possible. Figures 2.17 and 2.19 show the effect of the number of strips on core losses. A high number of strips reduces the flux density or secondary voltage distortion, thus reducing the losses especially that of the eddy current component which is dependent on the shape of the waveform. The % form factor (%FF) in Figures 2.18 and 2.20 is a simplified ASTM [4] method for indicating the deviation of a

waveform from its sinusoidal reference, that is, a measure of distortion. The %FF is calculated using *rms* quantities and is given by

$$\%FF = \frac{(E_s - E_{flux})}{E_{flux}} 100 . \tag{2.7}$$

Where E_s is the *rms* voltage obtained from the actual secondary voltage and E_{flux} is the rms voltage obtained from the sinusoidal waveform set-point. The reduction of %FF in Figure 2.18 when increasing the number of strips seems to be related to the reduction of core losses in Figure 2.17, however, it is possible for two waveforms to have the same %FF and yield different core loss results. This means that the %FF is not a true measure of the effect of distortion on losses.

The use of higher number of strips in the 200-turn frame yields results closer to sinusoidal at higher flux densities. The core loss results below 10% form factor are considered acceptable by the ASTM standard [4]. Therefore, 12 strips are used in this comparison with the 280-turn and 352-turn frames.

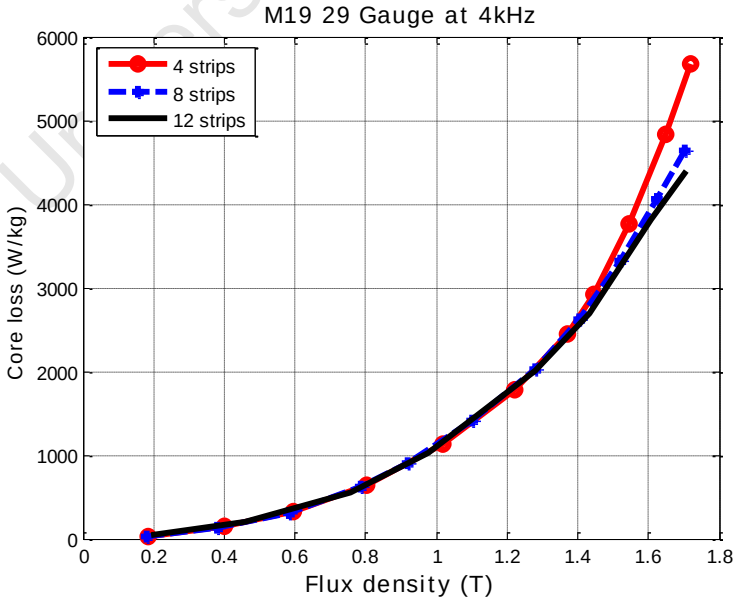

Fig. 2.17 Core loss comparison for 4, 8 and 12 strips at 4kHz

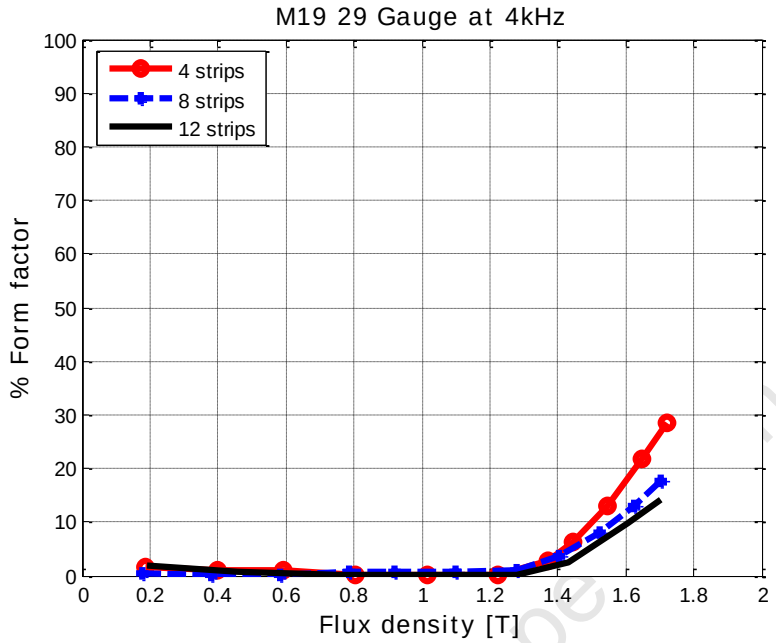

Fig. 2.18 % Form factor comparison for 4, 8 and 12 strips at 4kHz

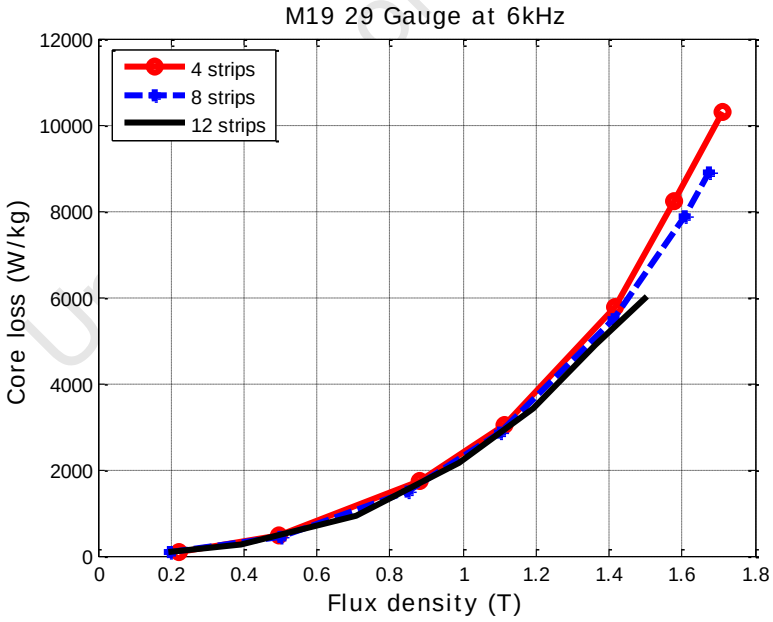

Fig. 2.19 Core loss comparison for 4, 8 and 12 strips at 6kHz

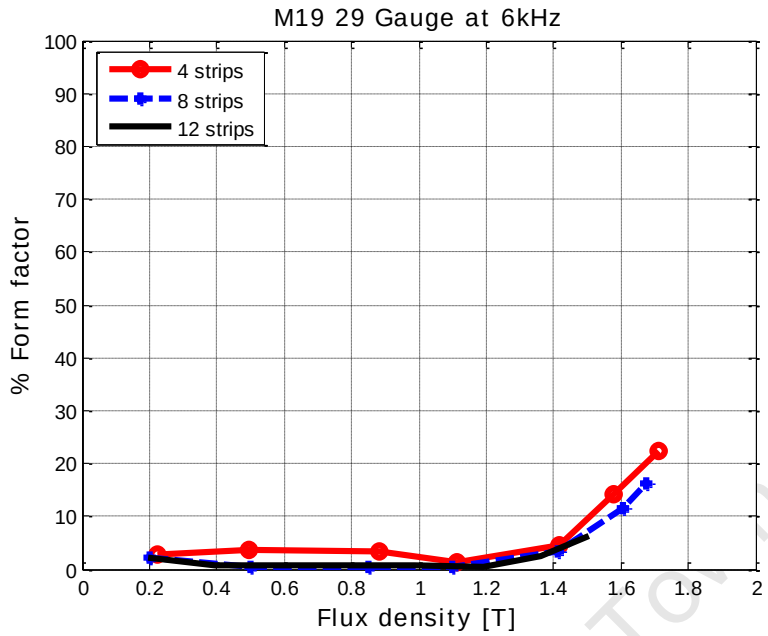

Fig. 2.20 % Form factor comparison for 4, 8 and 12 strips at 6kHz

2.4.2 Epstein frame comparison: 200, 280 and 352 - turn Frames

The 200-turn frame is compared with the 280-turn and 352-turn frames using M19_29 Gauge steel at 4kHz and 6kHz. Figures 2.21 and 2.22 show the comparison. The 280-turn and 352-turn frame results are approximately the same, with the 280-turn frame achieving higher flux densities than the 352 − turn frame as expected. The 280-turn frame results in Figures 2.21 and 2.22 are new results extended from [6], which were limited to 1kHz. The 200-turn frame has a 10% averaged deviation for the M19_29G material and reaches higher flux densities. The deviation is attributed to the difference in geometry, especially the size of the strip width which is 3 times lower than the standard strip and more prone to cutting stresses. The stresses pin the magnetic domains from moving and results in higher losses. The 200-turn frame results represent what will happen in small scale geometries, for example, small motors or transformers, where efficiencies are poor. The 280-turn Epstein frame can successfully replace the 352-turn frame at high frequencies and the 200-turn can be used to reach high flux densities and frequencies.

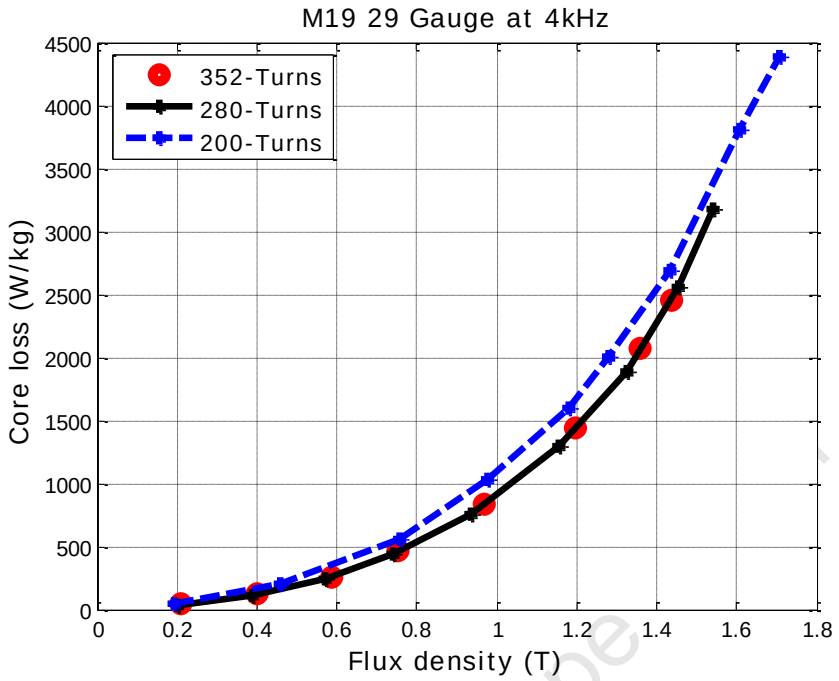

Fig. 2.21 352, 280 and 200-turn Epstein frames comparison at 4kHz

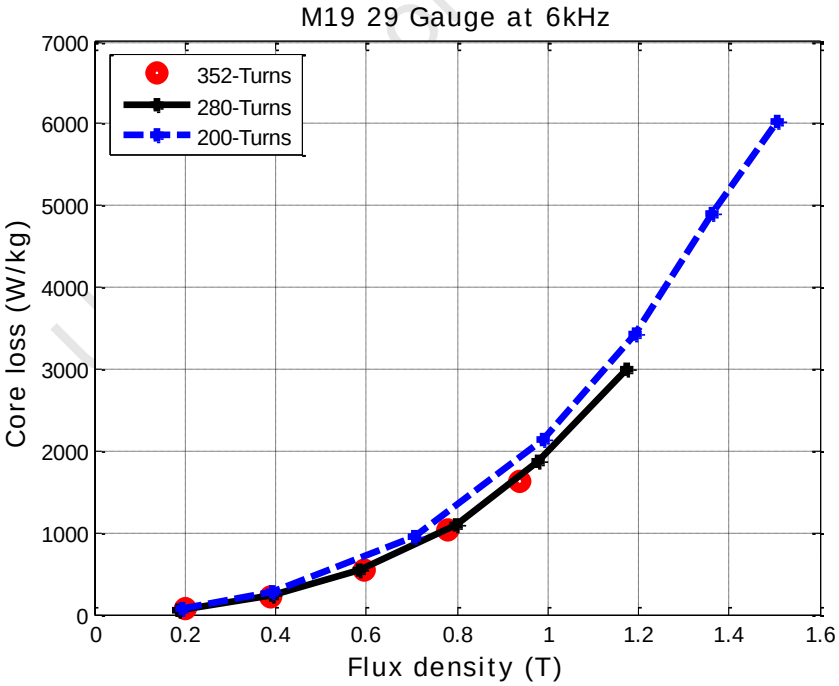

Fig. 2.22 352, 280 and 200-turn Epstein frames comparison at 6kHz

2.5 TOROID, EPSTEIN AND SST COMPARISION

A commercial 352-turn Epstein frame is used in this comparative study. The idea is to also compare the Epstein results with results from other lamination manufactures (e.g. AK steel) using similar frames. Figure 2.23 shows the size of the toroidal lamination in relation to the 30.5 cm and 11cm long Epstein samples. The test frequencies presented here are 50/60Hz (conventional motors) and 400Hz (airplane frequency). High frequency results also yield similar relationships.

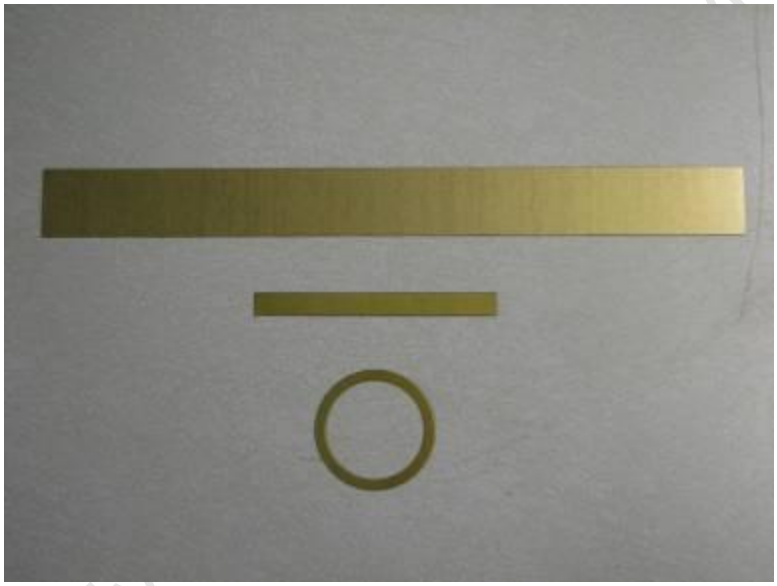

Fig. 2.23 Epstein 30.5cm (Top), Epstein 11cm (center) and Toroid (5mm Width) test samples

2.5.1 Epstein Frame and SST Comparison

The Epstein strips in Figure 2.23 can be cut in the rolling direction known as the L (longitudinal) direction or 90º to the rolling direction, known as T (transverse) direction. The L direction has favorable magnetic properties as indicated by the permeability in Figures 2.25 and 2.27 when the flux density is oriented along this direction, whereas the T direction has less favorable magnetic properties. In Epstein tests, the L and T strips are inserted in opposite limps. This arrangement emulates motor laminations. When using

the SST, two tests are done; one with the L strip and another one with the T strip. The results are averaged and are close to the Epstein results with maximum difference of <3.5% as shown in Table 2.2.

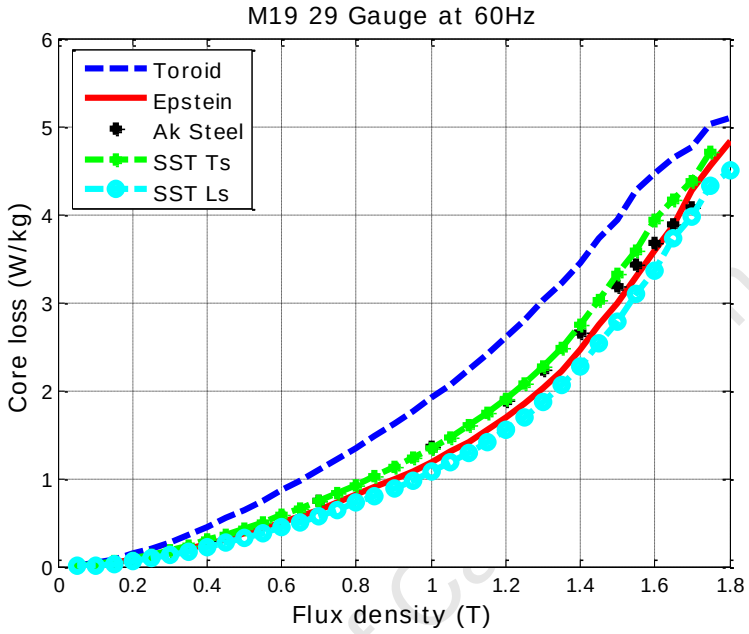

Fig. 2.24 Epstein, Toroid and SST core loss comparison at 60Hz

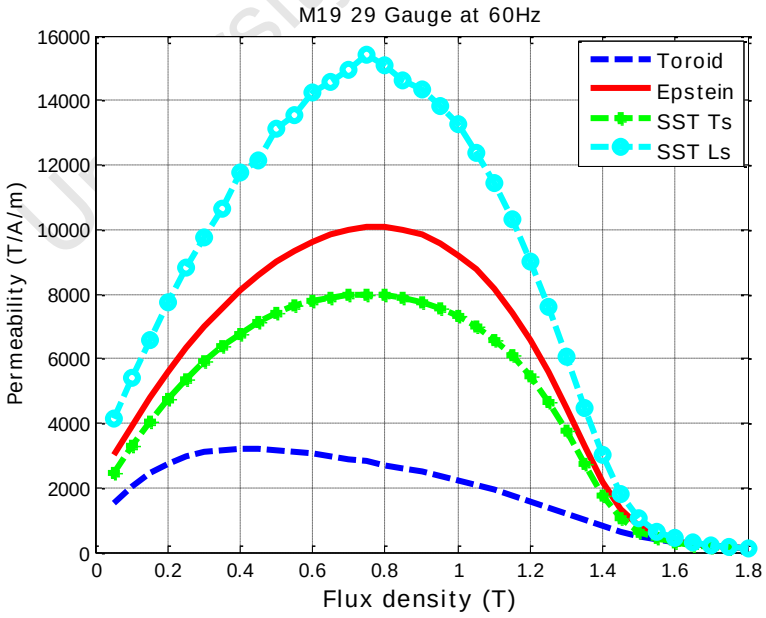

Fig. 2.25 Epstein, Toroid and SST permeability comparison at 60Hz

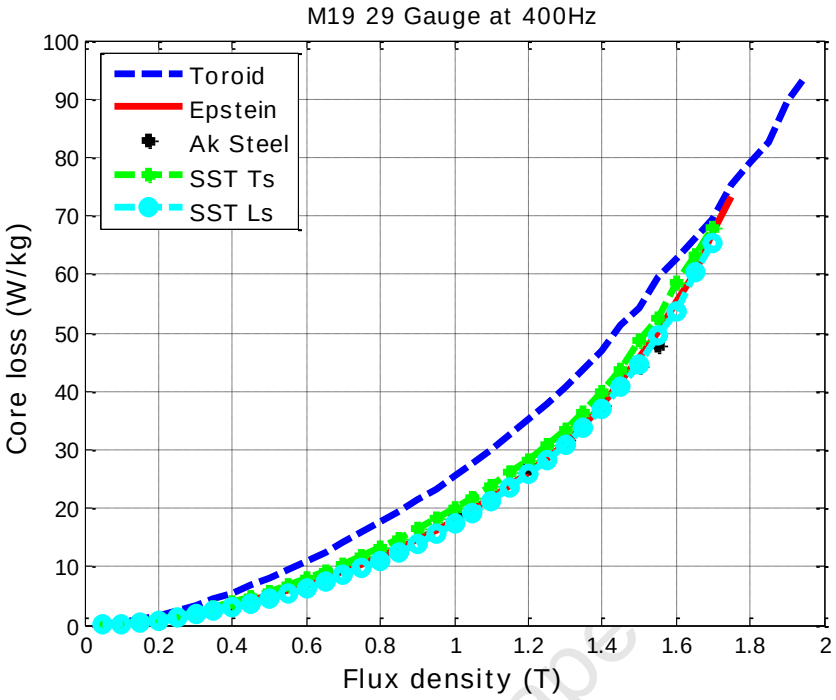

Fig. 2.26 Epstein, Toroid and SST core loss comparison at 400Hz

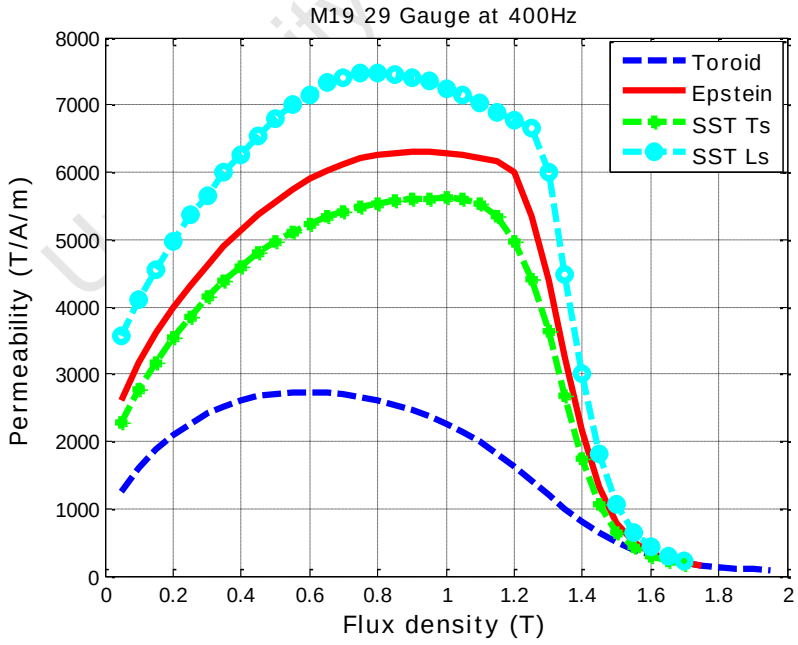

Fig. 2.27 Epstein, Toroid and SST permeability comparison at 60Hz

Table 2.2 SST and Epstein frame comparison

M19_29G 60Hz						M19_29G 400Hz				
B	SST Ts	SST Ls	Average	Epstein	Diff*.	SST Ts	SST Ls	Average	Epstein	Diff*.
(T)	(W/kg)	(W/kg)	(W/kg)	(W/kg)	(%)	(W/kg)	(W/kg)	(W/kg)	(W/kg)	(%)
0.30	0.18	0.13	0.16	0.15	-2.71	2.31	1.79	2.05	2.01	-2.21
0.50	0.43	0.32	0.38	0.37	-1.83	5.75	4.57	5.16	5.03	-2.46
0.70	0.75	0.57	0.66	0.65	-1.96	10.44	8.51	9.48	9.21	-2.92
0.90	1.13	0.89	1.01	0.99	-1.83	16.45	13.90	15.17	14.68	-3.35
1.00	1.35	1.07	1.21	1.19	-1.78	20.02	17.30	18.66	18.03	-3.49
1.30	2.27	1.86	2.06	2.02	-2.09	33.40	30.97	32.19	31.21	-3.11
1.50	3.33	2.79	3.06	3.00	-2.05	48.56	44.49	46.52	45.58	-2.07
1.55	3.58	3.09	3.34	3.28	-1.57	52.49	49.47	50.98	50.09	-1.77
1.60	3.94	3.35	3.65	3.60	-1.43	58.66	53.71	56.18	55.03	-2.10
1.65	4.17	3.72	3.95	3.87	-2.02	63.22	60.34	61.78	59.97	-3.00
1.70	4.37	3.97	4.17	4.27	2.34	67.90	65.44	66.67	66.17	-0.76

The % difference in Table 2.2 is the difference between the averaged SST results and Epstein, with Epstein results as reference. The Epstein results also have good correlation with the measured loss from AK steel lamination manufacturer, a good indication of repeatability.

2.5.2 Epstein Frame and Toroid Comparison

The core loss results of an M19_29G small toroid (5mm width) in Figure 2.24 and 2.26 are higher than the Epstein test at flux densities below saturation. The flux density waveforms are sinusoidal in both tests (% FF < 1%), therefore the distortion is not a factor. The permeability curves in Figures 2.25 and 2.27 indicate that the toroid is less permeable when compared to the Epstein. The percentage loss difference in shown in Table 2.3 for M19_29G steel at 60Hz and 400Hz. The core loss difference can be interpreted as the toroid requiring higher magnetic field strength H_a to achieve the same flux density point, leading to high losses. Figure 2.28 shows the core loss results of a toroid with 20mm width. The averaged % difference is 9% and significantly lower that the 5mm toroid results.

The toroidal geometry is different from the standard 94-cm Epstein frame. With small toroidal fixtures, cutting stresses may propagate to the center of

the toroidal strip, making it difficult for the magnetic domains to align in the direction of the applied field without applying high H_a (or current). The results from the small toroid are however close to the results obtained using the new 200-turn Epstein frame. This is because the size of the samples is small and comparable.

Table 2.3 Toroid and Epstein frame comparison

	M19_29G 60Hz			M19_29G 400Hz			8050 50Hz		
B	Toroid	Epstein	Diff.	Toroid	Epstein	Diff.	Toroid	Epstein	Diff.
(T)	(W/kg)	(W/kg)	(%)	(W/kg)	(W/kg)	(%)	(W/kg)	(W/kg)	(%)
0.30	0.28	0.15	45.91	3.36	1.99	40.69	0.46	0.38	16.90
0.50	0.65	0.37	42.93	8.06	5.01	37.86	1.08	0.97	10.02
0.70	1.10	0.65	41.04	14.10	9.18	34.90	1.83	1.55	15.48
0.90	1.62	0.99	38.77	21.37	14.64	31.48	2.72	2.42	11.14
1.00	1.92	1.19	37.82	25.51	17.99	29.46	3.23	2.93	9.39
1.30	3.02	2.02	33.07	40.83	31.18	23.65	5.14	4.69	8.78
1.50	3.94	3.00	23.97	54.10	45.65	15.63	6.82	6.35	6.83
1.55	4.27	3.28	23.00	59.40	50.26	15.38	7.29	6.85	6.04
1.60	4.46	3.60	19.44	62.77	55.37	11.79	7.79	7.40	4.99
1.65	4.63	3.87	16.52	66.14	60.30	8.82	8.31	7.85	5.53
1.70	4.77	4.27	10.48	69.44	67.03	3.47	8.85	8.50	3.97
1.75	5.03	4.55	9.61	75.36	73.13	2.95	-	-	-

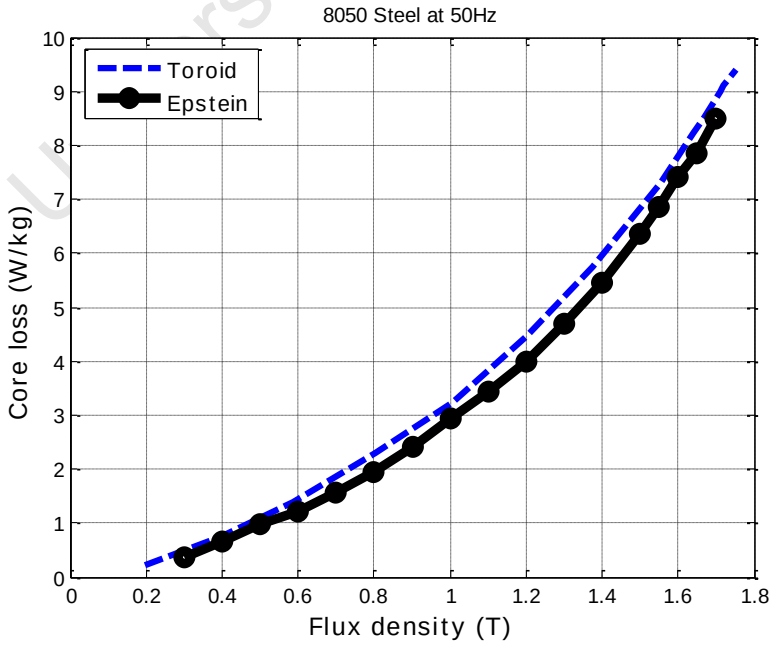

Fig. 2.28 Toroid and Epstein frame comparison

2.6 EFFECTS OF FRAMES AND TEST SAMPLES ON CORE LOSS MEASUREMENTS

2.6.1 Frames and Samples Configuration

The Toroid, Single Sheet Tester and Epstein frames are different testing fixtures, which may result in different core loss measurements as shown in the previous analysis. Epstein frame is widely used in industry but also have errors associated with path length and sample discontinuity at the joints [5]. The SST core loss results depends on the sample used, that is, whether it is a T (90º), L (0º) or diagonal (45º) cut strip. The user is obligated to know the conditions in which the losses are measured. Also, the SST results are calibrated by the Epstein results, rendering it dependent on the Epstein for verification. In many cases, the toroidal fixtures give higher losses than the two, and are becoming available through the ongoing EMERF project. The user has to be aware of the source of the core loss data and associated BH curves for correct application.

2.6.2 Samples Preparation and Arrangement

Samples are either punched or laser cut to dimension regulated by the ASTM standards [4]. The two processes can affect the core loss results. One such case is observed on a 35H300 Japanese steel. One set of 16 strips is laser cut and another set is punched from the same batch of material. Tests are performed using the 352-turn Epstein frame on the Donart system. Figure 2.29 shows the effect of punching and laser cutting of strips at 60Hz. In this case, the laser cut strips show higher losses with an average difference of 26.6%. Similar differences are also observed at 50Hz, 200Hz and 400Hz. The designer has to be aware of the difference in order to model the losses accurately, especially when the prototype laminations are laser cut and the production laminations are punched.

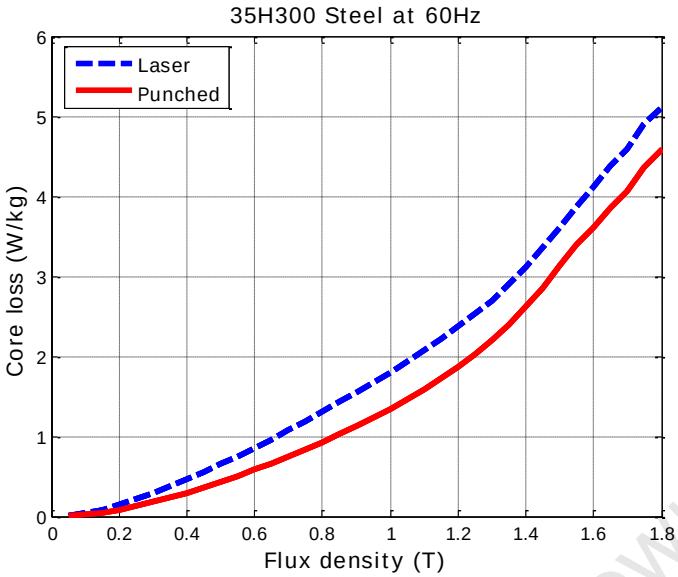

Fig. 2.29 Comparison of core loss results for punched and laser cut strips at 60Hz

The arrangement of strips is also been investigated. Beside the T and L strips arrangement, motor laminations are sometimes flipped over and unaligned, with burrs forming short circuits when forming a core. The effect of flipping and unaligned strips is investigated on a M19_29 Gauge toroidal fixture at 400Hz and 1kHz. High frequencies are chosen to include heating effects in the measurements. Figure 2.30 indicates that there is no difference in losses; this is true when there are no short circuits between adjacent strips.

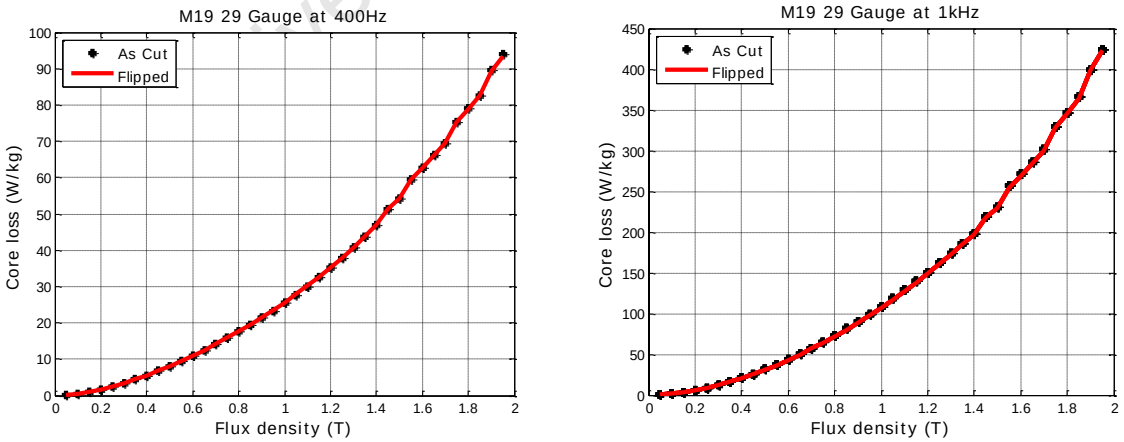

Fig. 2.30 Comparison of core loss results for As-cut and flipped strips at 400Hz and 1kHz

2.6.3 Sample Annealing

Annealing is a process that improves the material magnetic properties either at the production stages (Fully-processed materials) or after cutting the laminations. Motor manufacturers using fully-processed materials tend not to anneal motor laminations after cutting. This is to reduce manufacturing time and associated cost, and also the belief that since the material is annealed before cutting it has not degraded significantly.

The effect of annealing has been reported in detail in [8]. The tests were done using test bench system. Figure 2.31 shows core loss measurement performed on unannealed Epstein and toroidal fixtures. The strips were then annealing and retested. A 50% and 60% reduction in losses is observed in Figure 2.32 for the Epstein and Toroid respectively. The annealing process improved the magnetic properties and also relieved cutting stresses, hence the reduction in core loss. This is true for the small toroidal fixtures which are more susceptible to cutting stresses.

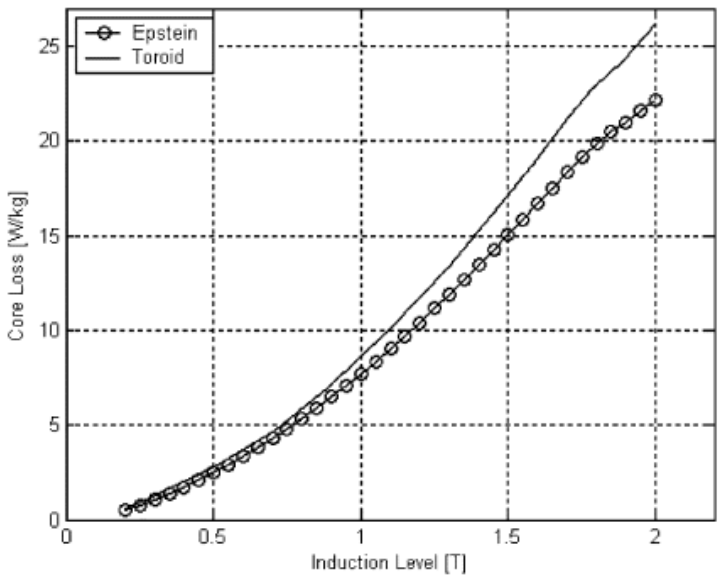

Fig. 2.31 Core loss results for unannealed steel at 60Hz [8]

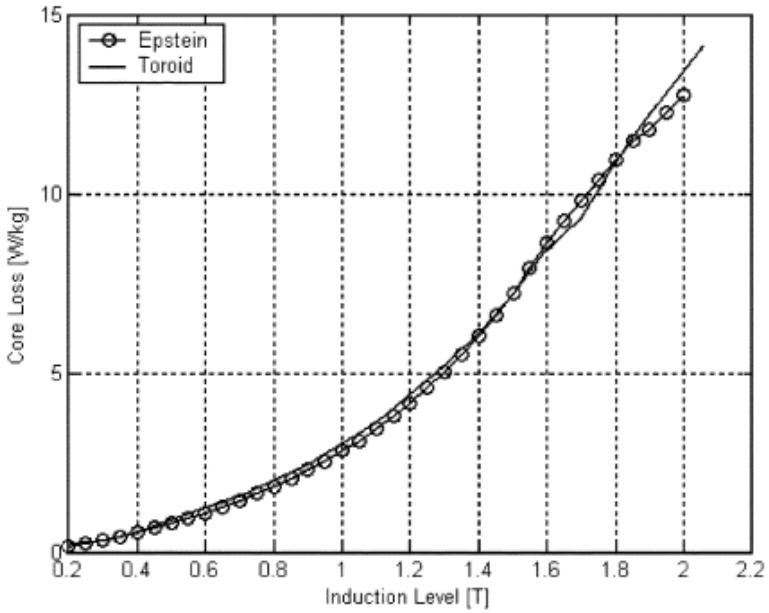

Fig. 2.32 Core loss results for annealed steel at 60Hz [8]

2.6.4 Core Loss Results Correction Factor

Core loss results are usually reported for materials subjected to sinusoidal flux densities at various frequencies for comparison purposes. However, as the material saturates, the flux density waveform becomes nonsinusoidal or distorted. At low frequencies, feedback is sometimes used to keep the secondary voltage sinusoidal, thus minimizing the distortion or %FF while achieving high flux density values. The ASTM standard has defined a loss correction factor for cases where the %FF is greater that 1% and less that 10% [4]. The correction factor is given by

$$P_{corrected} = \frac{P_{measured}}{\left(h + \left(\frac{E_s}{E_{flux}}\right)^2 e\right)} 100 \qquad (2.8)$$

h and *e* are % hysteresis and % eddy current losses respectively. $P_{measured}$ is the actual measured loss before correction. $P_{corrected}$ is supposed to present the loss without distortion, however this is not trivial since the split of hysteresis and eddy current loss is difficult to quantify. Figure 2.33 shows the effect of different splits on the core loss results, achieved by varying the % eddy current loss *e* (h = 100 − e). The ASTM standard has typical values of *e*, which in this case is about 24% for non-oriented steel with 0.36mm thickness. The corrected factor which satisfies the sinusoidal conditions is 50%, which means the ASTM *e* values are not generic. The user has to be aware of the effect of correction factor, as it affects losses at high flux density. One way to avoid using (2.8) is to use proper feedback or report core loss results with %FF < 1%

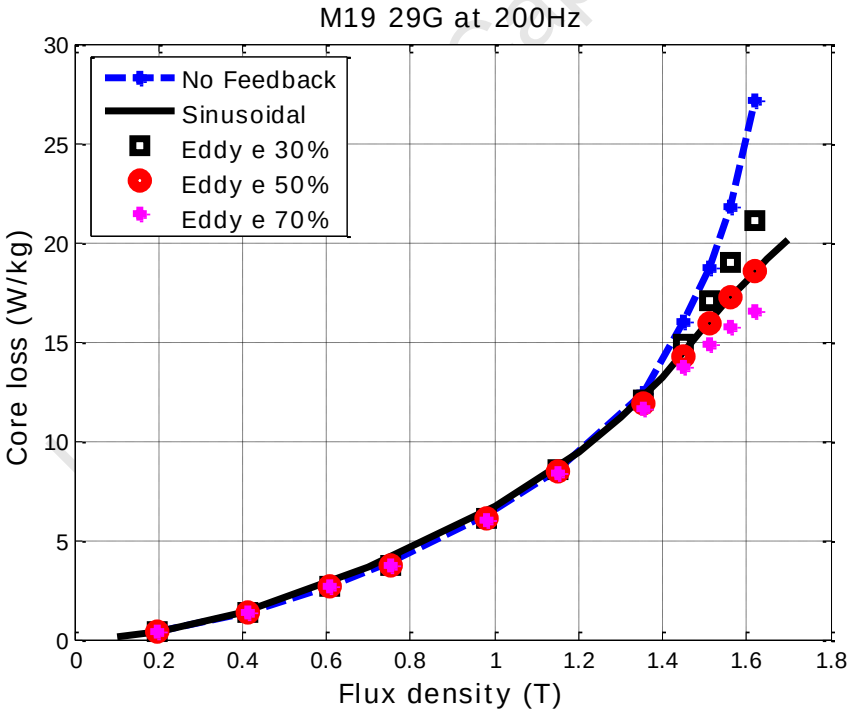

Fig. 2.33 Effect of the correction factor on core loss results

2.7 CONCLUSIONS

- The two core loss measurement formulae yield similar results for different testing frames and materials at various frequencies. The core loss results from the developed laboratory test bench shows good correlation with the new commercial Donart test equipment. The repeatability of the two test equipment is acceptable.

- The new 200-turn non-traditional Epstein frame measures losses at high frequencies and high flux densities with acceptable accuracy, surpassing the 352-turn and 280-turn frames capabilities. The 280-turn EMERF Epstein frame results are extended from 1kHz to 6kHz and achieved higher flux density than the standard 352-turn frame.

- The Single Sheet Tester core loss results are averaged for comparison with Epstein results. The SST is calibrated by the Epstein results. The core loss results measured from small unannealed toroidal fixture are higher than Epstein, a representation of the practical situation in motor design. Better correlation with standard Epstein is observed with the large toroid.

- Core loss measurements are affected by frame and sample configuration, preparation, arrangement, annealing and correction factors. The user has to be aware of these effects in order to make a proper choice before designing and adjustment during the design process.

Chapter 3

3. CORE LOSS MODELING

3.1 OVERVIEW

In electric machine design, accurate core loss formulae are required in order to predict core losses when calculating the performance of the machine and for design optimization. Several core loss models have been developed in literature [1] [8]-[14]. This chapter presents the comparison of the models used in popular commercial motor design softwares such as SPEED PCBDC and Flux2D using the resent core loss results. The original Steinmetz's two-term formula is reviewed and analyzed first. The modified Steinmetz' formula used in PCBDC is reviewed next and compared with the original Steinmetz formula revealing interesting results. Bertotti's formula used in Flux2D is also addressed, starting from the eddy current loss classical model with physical basis and the domain wall theory. Finally, the new formula, extended from Berttoti's approach, is presented and tested under low and high frequencies sinusoidal and non-sinusoidal excitations with good accuracy.

3.2 CONVENTIONAL CORE LOSS MODEL ANALYSIS

3.2.1 Steinmetz's Two-Term Model

The first core loss formula originated from Steinmetz's work [1] in 1892. He performed several core loss experiments on different magnetic circuits excited with sinusoidal currents of frequencies up to 205Hz [1]. From the experimental results, core loss per cycle is plotted vs. flux density at various frequencies and a mathematical expression is sought through curve fitting - an Engineering approach. The idea was to develop a simple formula which depends only on the flux density and frequency. A formula composed of hysteresis and eddy current components was deduced and is given by

$$\overline{P} = k_h B_p{}^n f + k_e B_p{}^2 f^2 \tag{3.1}$$

where $\overline{P}$ is the average loss per unit mass at frequency f and peak flux density B_p, Steinmetz's constant n = 1.6, k_h and k_e are hysteresis and eddy current loss constant coefficients respectively. The coefficients k_h and k_e are obtained from measured core loss data at each frequency and averaged where applicable to get a generic formula applicable for all tested frequencies. 10% maximum deviation from measured results has been reported in [1]. For engineering applications, only two measured core loss data are required to calculate k_h and k_e with n = 1.6 or known, else a minimum of three data points is required.

3.2.2 Classical Model with Physical Basis

Work has been done in studying the physical origin of eddy current losses and modeling these losses using a physics based approach [2] [9]. The eddy current losses are caused by the currents generated by the voltages due to changes in magnetic flux density. Therefore, the eddy current loss component was derived using a set of Maxwell's equations below,

$$\begin{aligned} \nabla \times \vec{H} &= \vec{J} \\ \nabla \times \vec{E} &= -\frac{\partial \vec{B}}{\partial t} \\ \vec{J} &= \sigma \vec{E} \end{aligned} \tag{3.2}$$

where $\vec{H}$, $\vec{E}$, $\vec{J}$ and $\vec{B}$ are magnetic field, electric field, current density and flux density vectors. Uniform flux density in the lamination is assumed and the impact of skin effect is neglected. The full derivation is found in [2]. The origin of the work is not known but Graham [9] assumed it to be from Steinmetz's work because of similarities.

Under sinusoidal flux densities, the classical eddy current loss, $\overline{P}_{cl}$, takes a form of

$$\overline{P}_{cl} = \frac{\sigma \pi^2 d^2}{6\rho} B_p{}^2 f^2 = k_{cl} B_p{}^2 f^2 \tag{3.3}$$

where σ, ρ and d are material conductivity, density and thickness respectively. Substituting (3.3) into the eddy current components in (3.1), results in a classical model given by

$$\overline{P} = k_h B_p{}^n f + \frac{\sigma \pi^2 d^2}{6\rho} B_p{}^2 f^2 \tag{3.4}$$

Only one measured loss data is required to calculate k_h, when n and material properties are known. Equation (3.4) is invalid when used to predict losses at high frequencies, especially with thick materials. The calculated eddy current loss component becomes much larger than the total measured losses (Hysteresis and dynamic losses) as shown in Figure 3.1 for the 8050 steel with 0.5mm thickness. This is because of higher loss coefficient k_{cl} compared to thin materials. It can be concluded that skin effect should be taken into account when using (3.4), especially with thick materials or high frequencies.

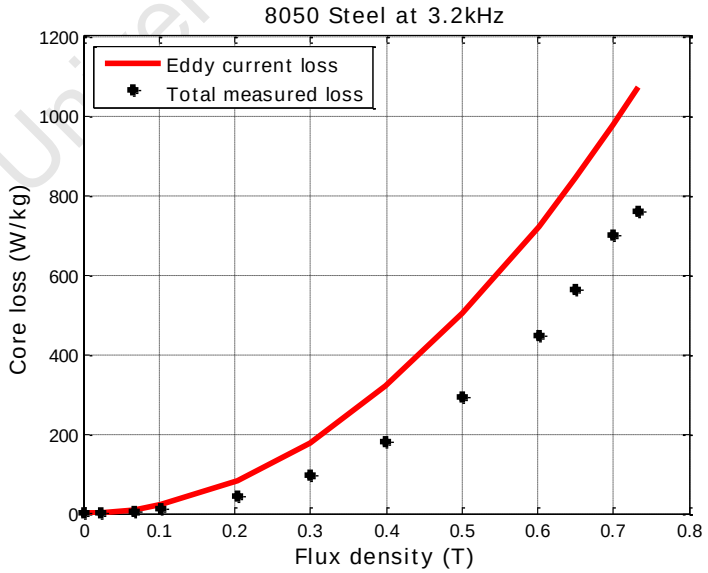

Fig. 3.1 Calculated eddy current loss and total measured loss comparison at 3.2kHz

3.2.3 Steinmetz and Classical Model Comparison

A comparison between equations (3.1) and (3.4) is now examined. In this case, the Steinmetz's formula (3.1) is compared with (3.4) for n = 1.6 in both equations. Steinmetz's test results are limited to 205Hz and an extension to high frequencies is made to test validity at high frequencies. Several materials (M19_29Gauge, M36_26G, 35H300, M45_29G and 8050 steel) are used in this study. The loss coefficients are recalculated at each test frequency to give the best possible loss estimates.

For a thin material such as M19_29Gauge (Epstein frame), the coefficients k_h and k_e are calculated at 1.5T, 60Hz and 1kHz and are all positive numbers. Equations (3.1) and (3.4) yield similar results at low and high frequencies as shown in Figures 3.2 despite the deviation from measured results.

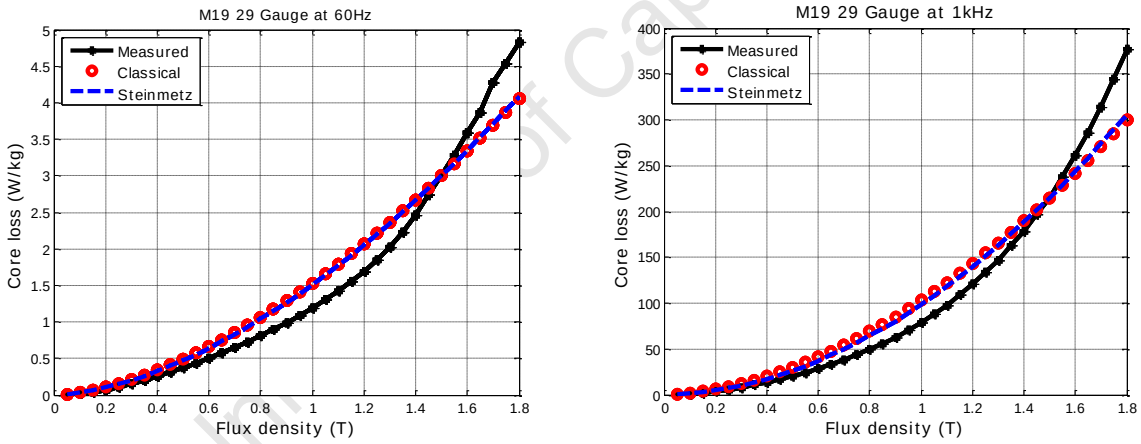

(a) 60Hz (b) 1kHz

Fig. 3.2 Steinmetz and Classical formulae comparison at 60Hz and 1kHz

For a thick material such as 8050 steel (Toroid frame), the coefficients k_h and k_e are calculated at 1.5T, 60Hz; 1T, 1kHz and 0.7T, 3.2kHz. Measured loss data are not available at high flux densities and frequencies, therefore, low flux density points are used. Figure 3.3a and 3.3b also show good correlation between the two formulae at 1kHz and 3.2kHz.

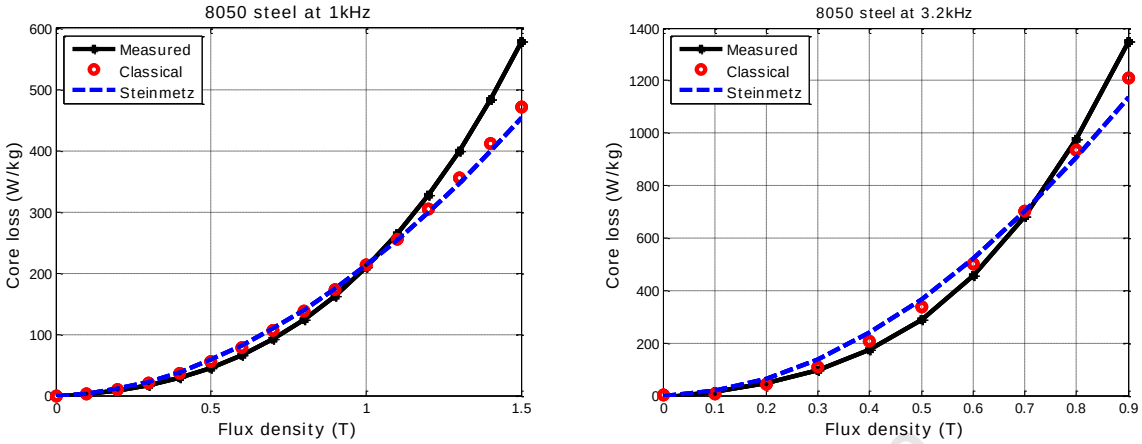

(a) 1kHz (b) 3.2kHz

Fig. 3.3 Steinmetz and classical formulae comparison at 1kHz and 3.2kHz

A negative hysteresis loss coefficient k_h is calculated at 3.2kHz using equation (3.4). This is because the calculated eddy current component is higher than the total measured losses as shown in Figure 3.1, and equation (3.4) compensates the error by subtracting the hysteresis component from the eddy current loss component. The overall predicted loss results in Figure 3.2b hide this invalidity, which seems to be good from the engineering or user's perspective but unacceptable from a physics point of view. Table 3.1 shows further comparison of the two formulae for various materials. The difference between the two formulae is small.

The Steinmetz's formula is tested at higher frequencies and does not produce negative loss coefficients like the classical formula. The invalidity observed in (3.4) at high frequencies can be avoided by considering the skin effect. Low frequency operation avoids the problem altogether. The two formulae under estimate losses at high flux densities.

3.2.4 Effects of Limited Data and Steinmetz's Constant Variations

In practice, many steel and lamination manufactures supply core loss data at 50 or 60Hz, 1.5T. The use of low frequency loss data affects the prediction at higher frequencies. Figures 3.4a and 3.4b show the loss results at 200Hz

with coefficients calculated at 1.5T, 50Hz and 60Hz. Equation (3.4) shows good correlation with the measured results at low flux densities and under estimates at high flux densities (above 1.2T), whereas the Steinmetz's formula predicts better than (3.4) at high flux densities.

Table 3.1 Steinmetz and Classical model comparison

	M36_26G at 60Hz			**M45_29G at 200Hz**			**35H300 at 400Hz**		
B	Classic	Steinmetz	Diff	Classic	Steinmetz	Diff	Classic	Steinmetz	Diff
(T)	(W/kg)	(W/kg)	(%)	(W/kg)	(W/kg)	(%)	(W/kg)	(W/kg)	(%)
0.10	0.02	0.02	-11.30	0.20	0.16	-23.38	0.45	0.38	-17.81
0.20	0.06	0.05	-9.04	0.62	0.53	-18.09	1.45	1.27	-13.55
0.40	0.19	0.17	-6.34	1.98	1.76	-12.21	4.71	4.33	-8.98
0.70	0.47	0.45	-3.84	5.06	4.72	-7.15	12.37	11.76	-5.18
1.00	0.85	0.83	-2.10	9.23	8.89	-3.82	23.01	22.40	-2.74
1.20	1.15	1.14	-1.17	12.58	12.32	-2.11	31.66	31.19	-1.50
1.30	1.32	1.31	-0.76	14.42	14.23	-1.35	36.43	36.08	-0.96
1.40	1.49	1.49	-0.37	16.36	16.25	-0.65	41.50	41.31	-0.46
1.50	1.68	1.68	0.00	18.40	18.40	0.00	46.86	46.86	0.00
1.55	1.77	1.77	0.18	19.46	19.52	0.31	49.65	49.76	0.22
1.60	1.87	1.87	0.35	20.54	20.67	0.61	52.51	52.73	0.43
1.65	1.97	1.98	0.51	21.65	21.85	0.90	55.44	55.79	0.64
1.70	2.07	2.08	0.67	22.79	23.06	1.18	58.44	58.93	0.83
1.80	-	-	-	-	-	-	64.65	65.45	1.21

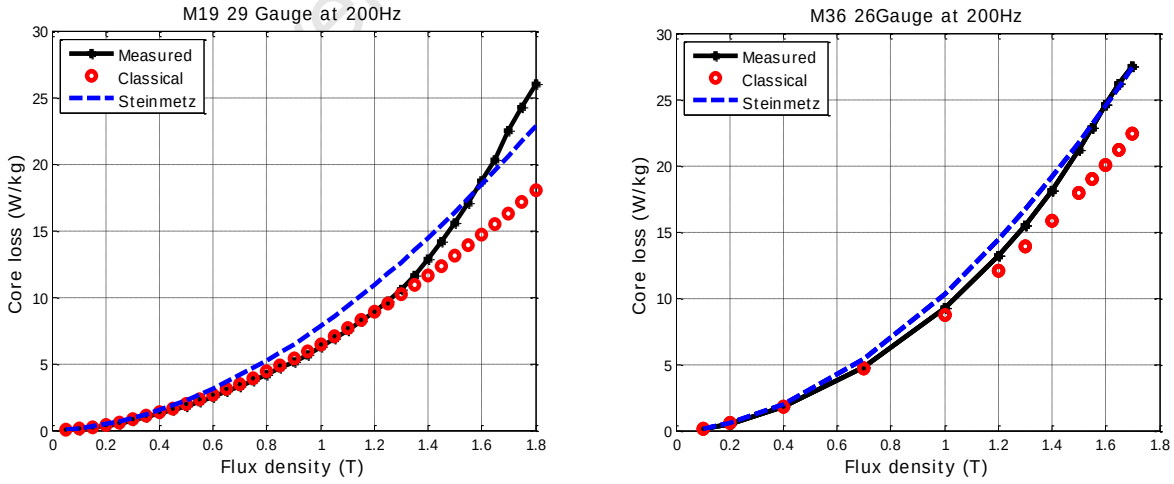

(a) M19_29G at 200Hz (b) M36_26G at 200Hz

Fig. 3.4 Effect of limited data at 200Hz: Steinmetz and Classical models

Beside the effects of limited loss data presented above, the use of Steinmetz's constant, *n = 1.6,* does not generally apply to all flux density ranges for all materials. A constant value of *n = 2* has been reported in [12] [13] irrespective of the electrical steel used and will therefore be compared with *n = 1.6* and *2.3* for this material. An improved prediction with *n = 2.3* is observed in Figure 3.5 indicating that the value of *n* depends on the material used and should be calculated together with k_h and k_e for better prediction.

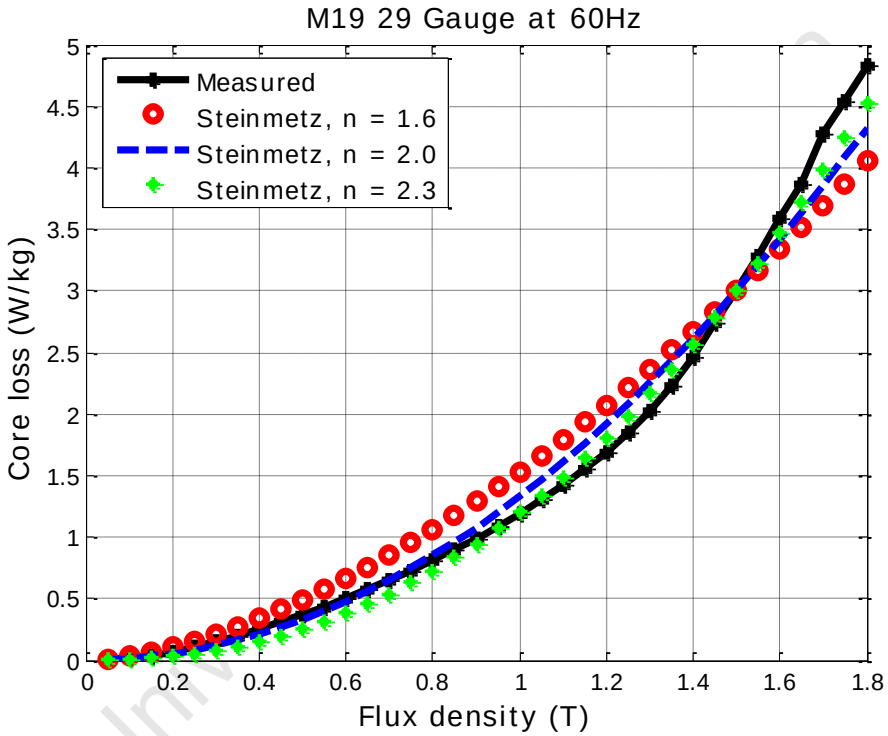

Fig. 3.5 Variation of Steinmetz's constant n at 60Hz using Steinmetz formula

3.2.5 Modified Steinmetz's Model

The Steinmetz's formula (3.1) has since been modified, reported and used in the commercial SPEED Brushless DC analytical software package (PCBDC) [15]. The modified Steinmetz's formula for sinusoidal flux density waveforms is given by

$$\overline{P} = k_h B_p^{\,a+bB_p} f + k_e B_p^{\,2} f^2 \qquad (3.5)$$

Where *a, b,* k_h are hysteresis loss coefficients and k_e is the eddy current loss coefficient. The Steinmetz's constant in (3.5) is defined as a function of peak flux density B_p to include different materials and the variation with flux density as observed in Figure 3.5. The coefficient calculation procedure requires a set of loss data points; loss vs. flux density at different frequencies or loss vs. frequency at different flux densities. Equation (3.5) divided by frequency gives

$$\frac{\overline{P}}{f} = k_h B_p{}^{a+bB_p} + k_e B_p{}^2 f = k_1 + k_2 f \tag{3.6}$$

where $k_1 = k_h B_p{}^{(a+bBp)}$ and $k_2 = k_e B_p{}^2$. The result is a linear relationship between loss per cycle (*P/f)* and frequency although this relationship is not followed by all materials. Plotting *P/f* vs. *f* at various flux densities (at least three *B* points) and extrapolating the curves to zero frequency yields three different values of k_1, which represents the hysteresis loss component. K_h, *a* and *b* are calculated using simple logarithmic expressions [14] [15]. The eddy current component k_2 is a slope of the three curves. Three values of k_e are calculated, then, they are either averaged or a maximum/minimum value is used. Figures 3.6 shows the loss results obtained from M19_29 Gauge and 35H300 electrical steels at 200Hz. The coefficients for the modified formula are calculated using the PCBDC software [15] with 20 − 400Hz, 0 − 1.8T loss data.

The Steinmetz' formula (3.1) prediction is better than the modified (3.5) at high flux densities for these materials although (3.5) predicts better in the low flux density range. The modified formula in PCBDC requires additional loss data and computation time. Moreover, the accuracy depends on the flux density points chosen for k_1, and whether k_e is averaged, minimized or maximized as shown in Figure 3.7. This trend is observed in several materials and it can be concluded that averaging coefficients result in better prediction. The Steinmetz' formula requires high flux density points, e.g.

1.5T, at frequencies of concern for better prediction. Both formulae under estimate the measured loss at high flux density and these findings has been observed on several materials tested.

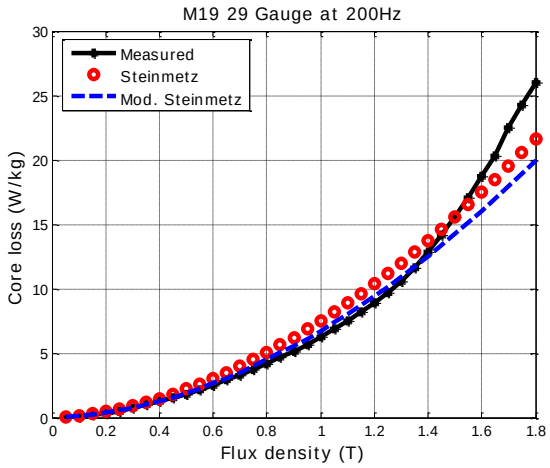

(a) M19_29G at 200Hz

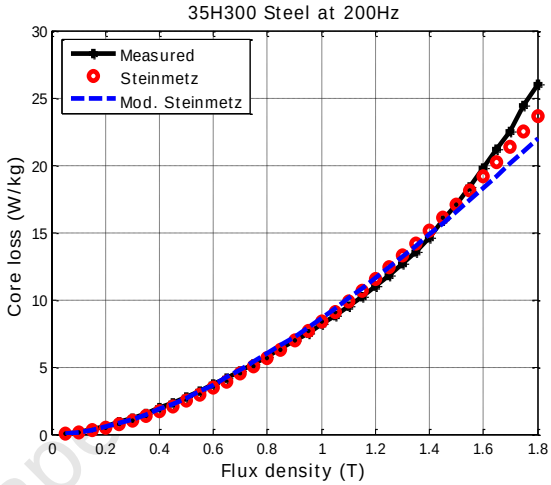

(a) 35H300 at 200Hz

Fig. 3.6 Steinmetz (3.1) and modified Steinmetz (3.5) formulae comparison at 200Hz

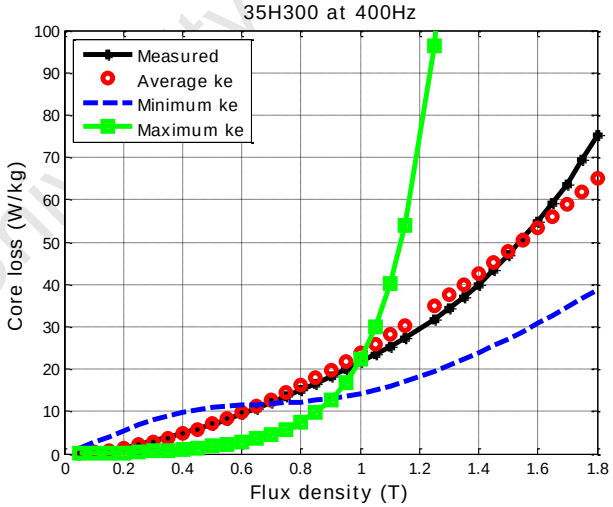

Fig. 3.7 Effect of averaging, maximizing or minimizing eddy current loss coefficient k_e

3.2.6 Bertotti's Three-Term Model

The Steinmetz's formula is based on the curve fitting engineering approach. Bertotti [1] [10] [16] [17] took a physicist's approach and began

his improvement from equation (3.4), which has a physical basis but under estimates losses. When dividing (3.4) by frequency, this results in a linear relationship between loss per cycle and frequency as shown in

$$\frac{\overline{P}}{f} = k_a + k_b f \tag{3.7}$$

where $k_a = k_h B_p^n$ and $k_b = k_{cl} B_p^2$. When observing the variation of measured loss per cycle with frequency, it has been found that the linear law is not always followed as shown in Figure 3.8. This meant that there are additional losses unaccounted for in (3.4). Equation (3.4) has been derived from a macroscopic approach i.e. without getting into microscopic details about the material intrinsic properties. Bertotti extended the work to a microscopic level, where a material is studied using the domain wall theory. The theory states that a magnetic material is made out of magnetic domains which move (expand and/or collapse) when magnetic field H_a is applied resulting in losses. A magnetic domain is described as a region in a material where the magnetic vectors **M** points in one direction and a domain wall as the separation between adjacent domains. In recent years, it has been made possible to view the domains on the surface of material as shown in Figure 3.9 [1].

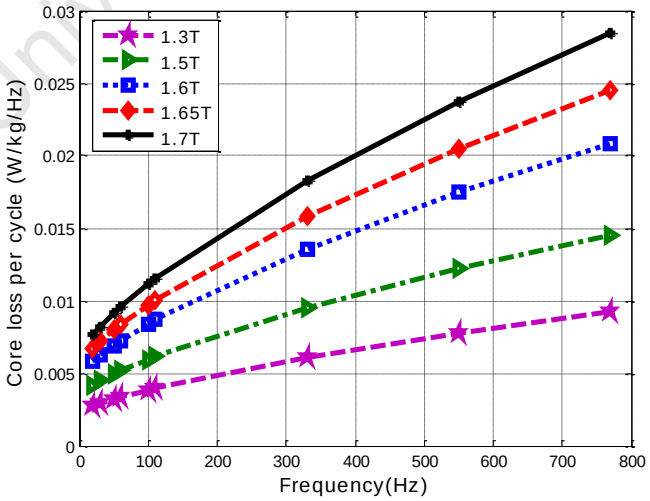

Fig. 3.8 Loss per cycle vs. frequency for M19_29 Steel

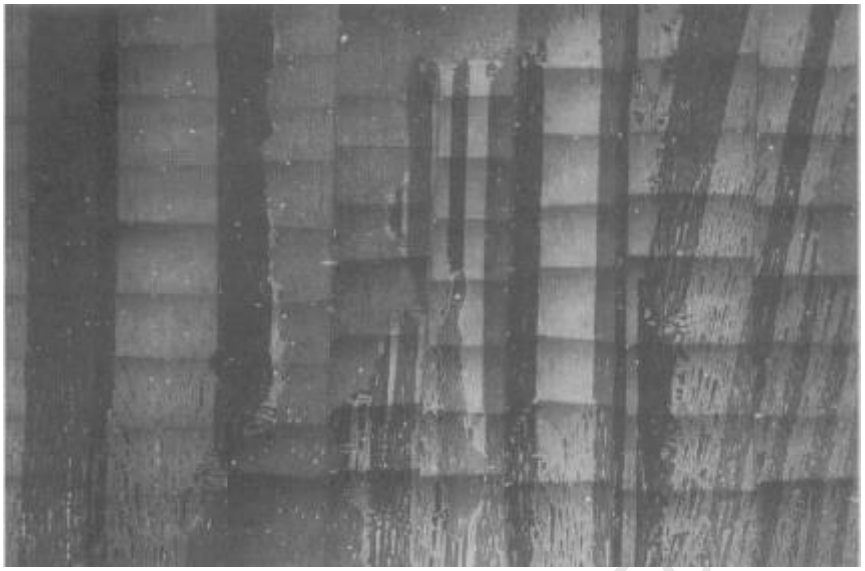

Fig. 3.9 Magnetic domain structure of a grain-oriented Si-Fe alloy [1]

When observing the behavior of loss per cycle as a function of frequency of different materials under sinusoidal flux densities as in Figure 3.8, Bertotti found that the loss behavior is described well by

$$\frac{\overline{P}}{f} = k_a + k_b f + k_c \sqrt{f} \tag{3.8}$$

where k_a, k_b and k_c are functions of peak flux density. From the magnetic domain theory and statistical approach, he deduced an expression given by [10]

$$\overline{P} \cong k_h B_p{}^2 f + \frac{\sigma \pi^2 d^2}{6\rho} B_p{}^2 f^2 + k_{ex} B_p{}^{1.5} f^{1.5} \tag{3.9}$$

$$where \quad k_{ex} = 8\sqrt{\sigma G S V_0}$$

which approximates core loss and agrees with the law in (3.8). The third term is the excess loss component due to the changes in local fields as the domain walls move, creating eddy currents which lead to losses and heating.

G and V_o are constants related to material intrinsic properties and S it the cross-sectional area. The second term will be referred to as classical eddy current loss component. Even though Bertotti derived his equation from physics he needed measured results to evaluate coefficients k_h and k_{ex} [2] [10]. The model calculates the average loss per electrical cycle of a steady-state simulation or measurements.

Bertotti tested the formula on different types of materials (grain-oriented, non-oriented and amorphous) under sinusoidal flux density up to 1.7T and frequency up to 100Hz [10]. The coefficients k_h and k_{ex} were calculated once from measured data at 0Hz and 50Hz, 1.5T. The formula showed good correlation at 1.5T. Figures 3.10, 3.11 and 3.12 show such comparison made on recent non-oriented M19_29 Gauge American steel at 60Hz and 200Hz, and 35H300 steel at 400Hz. Bertotti stated that the deviation above 1.5T was due to poor approximation (n = 2) of the hysteresis component and the deviation at low flux density is due to the neglected term *nVo/4* in the derivation of k_{ex} [10]. Bertotti's formula predicts better loss than the classical formula (3.4) at high flux densities but still under estimates the measured core losses.

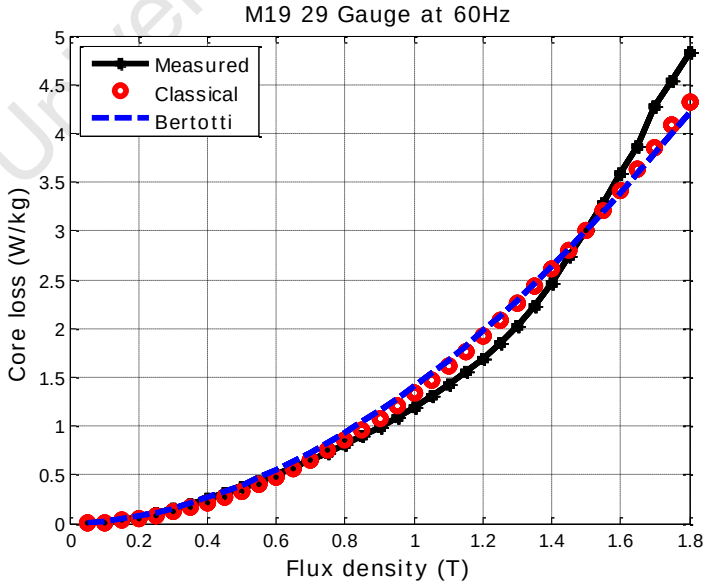

Fig. 3.10 Bertotti (3.9) and classical (3.4) formulae comparison at 60Hz

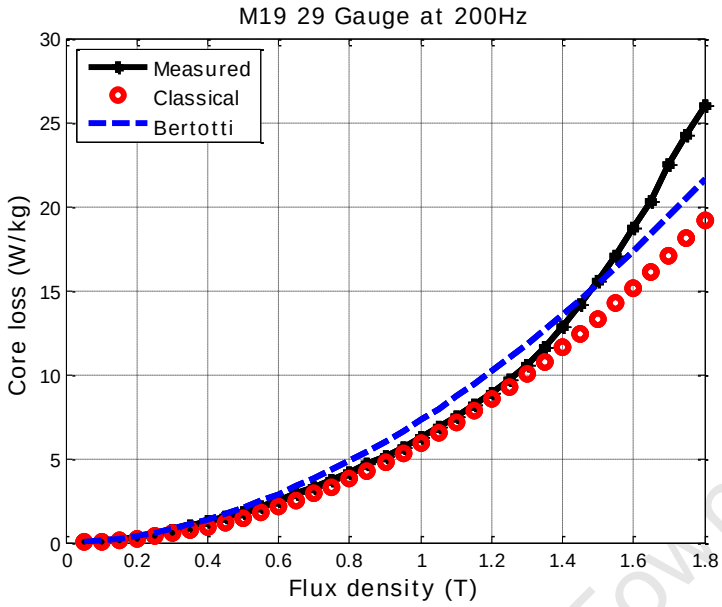

Fig. 3.11 Bertotti (3.9) and classical (3.4) formulae comparison at 200Hz

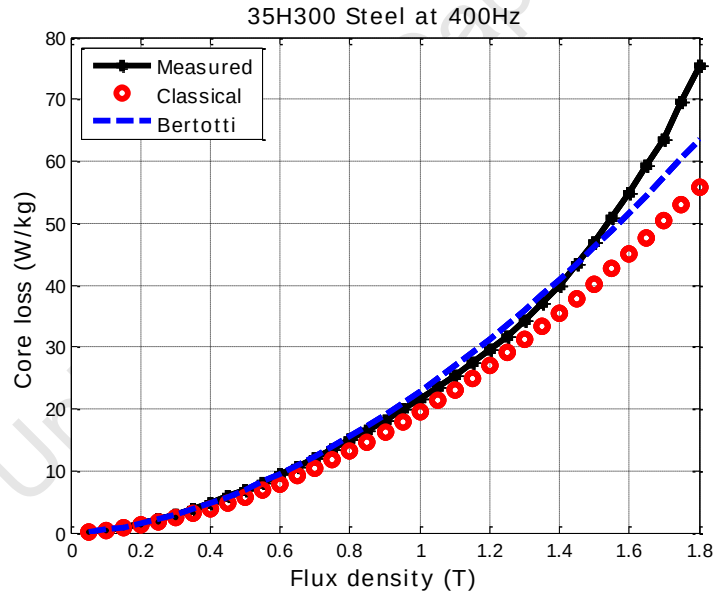

Fig. 3.12 Bertotti (3.9) and classical (3.3) formulae comparison at 400Hz

The introduction of excess loss component has improved Berttoti's model. From the mathematical point of view, it is clear that the accuracy depends on the selection of flux density and frequency values when calculating coefficients k_h and k_{ex}. In order to calculate losses at any arbitrary waveform, a generalized formula is given by

$$\overline{P} = k_h B_p{}^n f + \frac{\sigma d^2}{12}\frac{1}{T}\int\left(\frac{dB}{dt}\right)dt + \frac{k_{ex}}{\sqrt{2}\pi^{1.5}}\frac{1}{T}\int\left|\frac{dB}{dt}\right|^{1.5} dt \qquad (3.10)$$

where $\overline{P}$ is the average loss per electrical cycle of period *T*. The dynamic loss components (classical eddy and excess loss) are field rate (*dB/dt*) dependent, which means that they depend on the shape of flux density waveform. The hysteresis component is assumed to be field rate independent (or static) and only depends on the peak of flux density waveform [1] [7] [8]. This component can be assumed as losses obtained at constant field rate or field varying at very low frequencies 0 -1Hz (DC BH curve).

3.2.7 Other Core Loss Models

Little or no work has been reported or done to compare (3.10) with non-sinusoidal measured waveform results of various shapes and different materials. Furthermore, it follows that another shortcoming of (3.9) will be present in (3.10), i.e. calculating the coefficients at each flux density and frequency of interest in order to achieve high accuracy. This has led to the belief that the loss coefficients should vary with frequency and/or flux density [11]-[14]. From the physics point of view, the variation is justified as the material properties and behavior changes (skin effect, domains, etc) with flux density and frequency.

Based on the number of research papers produced [1] [8] [11]-[15] [18]-[21], it is clear that mathematically a large number of models may be developed. A few of these models are presented next.

$$\overline{P} = k_{ch} k_h B_p{}^{\alpha} f + \frac{k_e}{2\pi^2}\left(\frac{dB}{dt}\right)_{rms}^{2} + \frac{k_{ex}}{2\pi^{2\ \frac{3}{4}}}\left(\frac{dB}{dt}\right)_{rms}^{1.5} \qquad (3.11)$$

$$\overline{P} = k_h B_p{}^{a+bB} f + \frac{k_e}{2\pi^2}\left[\frac{dB}{dt}\right]_{rms} \tag{3.12}$$

$$\overline{P} = k_h B_p{}^{2} f + k_e B_p{}^{2} f^{2} + k_{ex} B_p{}^{1.5} f^{1.5} \tag{3.13}$$

$$\overline{P} = k_h B_p{}^{a+bB+cB^2} f + k_e B_p{}^{2} f^{2} + k_{ex} B_p{}^{1.5} f^{1.5} \tag{3.14}$$

$$\overline{P} = k_h(f,B) B_p{}^{\alpha(f,B)} f + k_e(B) B_p{}^{2} f^{2} + k_{ex}(B) B_p{}^{1.5} f^{1.5} \tag{3.15}$$

Equation (3.10) has been incorporated into Cedrat/Magsoft Flux2D/3D finite element (FE) software with n=2 irrespective of the material used – one of the shortcomings [27]. Equation (3.13), with n=2, has been incorporated in Ansoft Maxwell2D Finite Element software, where the eddy current coefficient k_e is calculated from measured loss data instead of material properties [28]. This resembles the same scenario found when comparing the Steinmetz's formula (3.3) and the classical formula (3.4).

Equation (3.11) is extended from Bertotti's model (3.9) to include minor loops in the hysteresis component [18]. Equation (3.12) has been incorporated in the SPEED PCBDC analytical software [15]. Equations (3.12) (3.14) and (3.15) are recent models with variable loss coefficients. Good results have been reported under sinusoidal excitations up to specified frequencies and flux densities with little or no the physical basis behind the variation of loss coefficients.

3.3 IMPROVED CORE LOSS MODEL

3.3.1 Model Development

An improved formula with a physical basis for the variation of loss coefficients with flux density and/or frequency developed by Lotten in [7] using the test bench results is presented and tested here. Furthermore, an

alternative averaging method of excess loss coefficient is presented as a modification in order to reduce the computation time. The new formula is an extension of Bertotti's formula in (3.10) addressing the shortcomings observed in Figures 3.10 - 3.12 and testing under non-sinusoidal flux density waveforms. The improved formula has good accuracy at high flux densities and frequencies, and takes a form of

$$\overline{P} = P_h(f,B) + k_e(f)B_p{}^2 f^2 + k_{ex}(f,B)B_p{}^{1.5} f^{1.5} \qquad (3.16)$$

The eddy current and excess loss coefficients k_e and k_{ex} are allowed to vary with frequency and with flux density. Variation of k_e with frequency accounts for skin effects at higher frequencies, this is especially important for thick materials. The excess loss coefficient varies with both flux density and frequency since flux density in the lamination is not uniform - contrary to what is commonly assumed. Moreover, at higher frequencies, the skin effect prevents flux from penetrating through the lamination. Hence, qualitatively, the dependence of k_{ex} on both frequency and flux density represents physical reality. It has been shown by Steinmetz in [1] that hysteresis losses per cycle does not vary significantly with frequency, hence extrapolating the *P/f* (total loss divided by frequency vs. frequency) curve in Figure 3.8 to zero frequency to determine hysteresis loss is justified. In this way, the material and operational dependence of n, the Steinmentz's constant, and k_h are implicitly included in the formula.

3.3.2 Core Loss Coefficients Calculation and Prediction

The hysteresis loss per cycle is determined by extrapolating the total loss per cycle in Figure 3.8 to zero frequency at various peak flux densities. The hysteresis loss per cycle is then plotted with flux density as shown in Figure 3.13. A minimum of five flux density points are required to improve the accuracy.

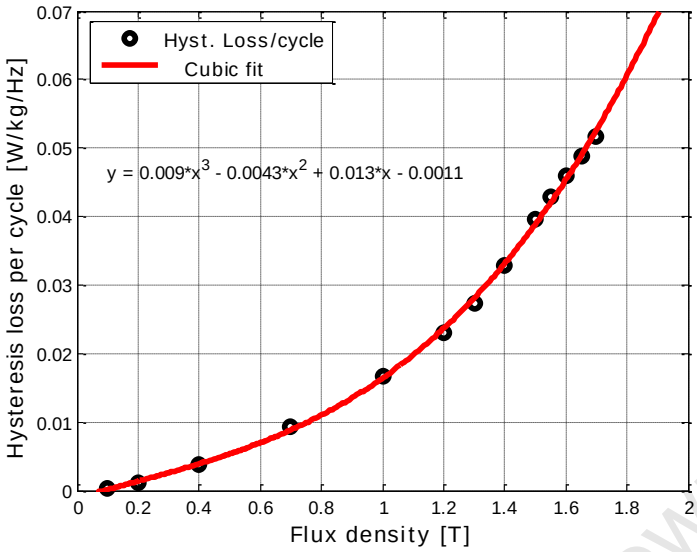

Fig. 3.13 Variation of hysteresis loss per cycle with flux density

Fitting a cubic curve in Figure 3.13 and multiplying the hysteresis loss per cycle by frequency results in

$$P_h = k_1 f + k_2 fB + k_3 fB^2 + k_4 fB^3 = P_h(f, B) \tag{3.17}$$

A lower order polynomial can be used or alternatively a single term power fit, all with reduced accuracy.

The variation of the classical eddy current coefficient k_e depends on skin effect. In this case, the skin depth is first calculated using

$$\delta = \sqrt{\frac{1}{f \pi \mu \sigma}} \tag{3.18}$$

where μ is the peak permeability. The choice of peak permeability is subjected to debate since μ varies with flux density. The skin depth δ is compared with lamination thickness d at frequency f. For $\delta \geq d$, k_e is calculated using

$$k_e = \frac{\sigma \pi^2 d^2}{6\rho} \tag{3.19}$$

which is the classical coefficient neglecting skin effect. For $\delta < d$, skin effects exist and k_e is estimated by [17]

$$k_e = \sigma \pi^2 K_{sk} \tag{3.20}$$

where k_{sk} is the effective thickness at a particular excitations with frequency, and is given by

$$K_{sk} = \left(\frac{\delta(e^{-\frac{2\delta - d}{\delta}} - e^1)}{e^{\frac{d}{\delta}} + 1} \right)^2 . \tag{3.21}$$

Equation (3.20) is more relevant to thick materials (e.g. 0.5mm) operating at high frequencies as this is where the skin effect is prevalent. Thin materials, although expensive, are preferred at high frequencies because they offer lower losses. The classical eddy current loss P_e is calculated using the second term in (3.16).

The variation of the excess loss coefficient with flux density and frequency results from loss separation is related to domain wall movements. In this case, knowing the hysteresis, classical eddy current and total losses from measured loss data, the excess loss P_{ex} can be separated as follows,

$$P_{ex} = P - P_h - P_e \tag{3.22}$$

The excess loss coefficient k_{ex} is then calculated using

$$k_{ex} = \frac{P_{ex}}{f^{1.5} B^{1.5}} \tag{3.23}$$

Figure 3.14 shows the variation of k_{ex} with frequency at different flux density levels.

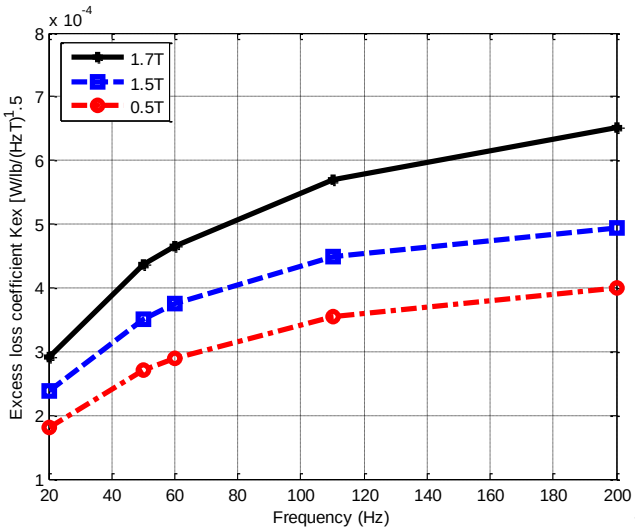

Fig. 3.14 Variation of excess loss coefficient with flux density and frequency

A logarithmic fit in Figure 3.14 can represent the variation of k_{ex} with frequency and flux density. The best-fit curve is in a form of

$$k_{ex}\ f, B_p = c\ B_p \ln\ f + d\ B_p \tag{3.24}$$

where $c\ B_p$ and $d\ B_p$ are flux density dependent coefficients. These coefficients are then plotted as a function of flux density as shown in Figure 3.15 and regression is applied in order to obtain a generalized expression for the $c\ B_p$ and $d\ B_p$ and subsequent $k_{ex}\ f, B_p$. The k_{ex} calculation is time consuming. Alternatively, the impact of the variation of k_{ex} with flux density can be represented by its average. This means that the k_{ex} will vary mainly with frequency. This method reduces accuracy when compared to the results obtained using (3.24) with variation of both frequency and flux density.

To summarize the coefficients calculation procedure, the hysteresis loss is subtracted from the total measured core loss data using extrapolation and can be predicted by (3.17). Eddy current loss coefficient k_e is calculated using (3.19) or (3.20) depending on skin depth, δ, thereafter eddy current loss is

calculated. The excess loss is calculated using (3.22) and k_{ex} is obtained through curve fitting and is described in (3.24).

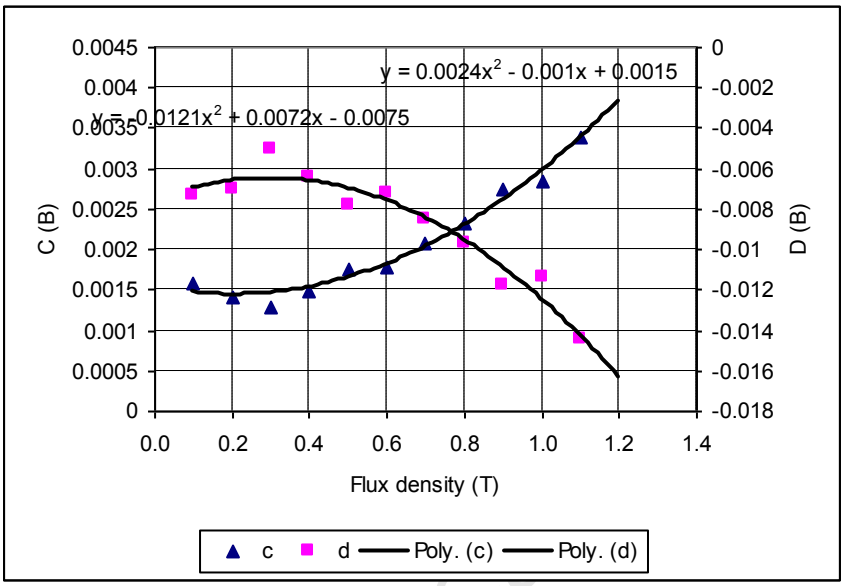

Fig. 3.15 Variation of coefficients c and d with flux density

Figures 3.16a and 3.16b show the comparison between the measured and calculated results using the improved formula (3.16). The calculated results show good correlation with the measured results from 60Hz – 4kHz. The materials tested here are used in the induction motor (8050 steel) in Chapter 4 and PM traction motor design in Chapter 5 (35H300 steel).

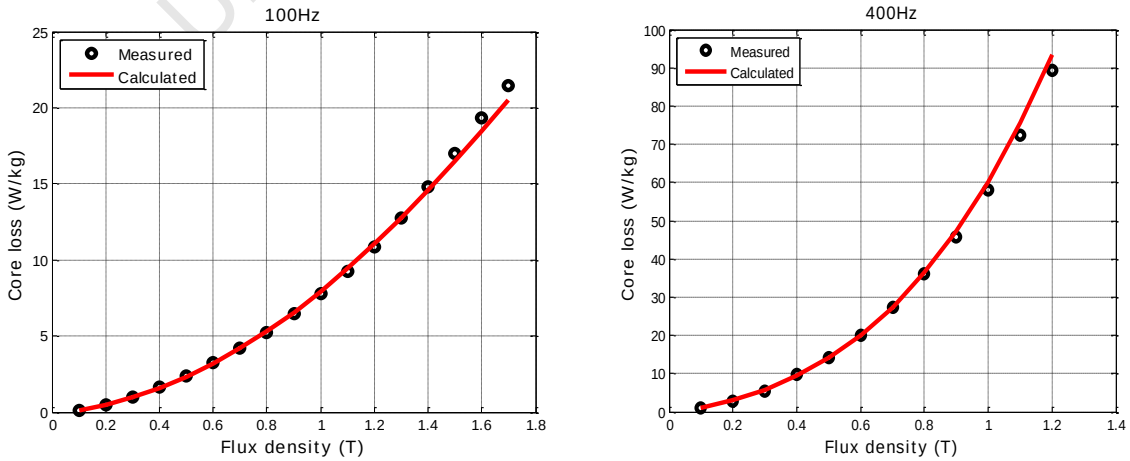

Fig. 3.16a Measured and calculated core loss results for 8050 steel

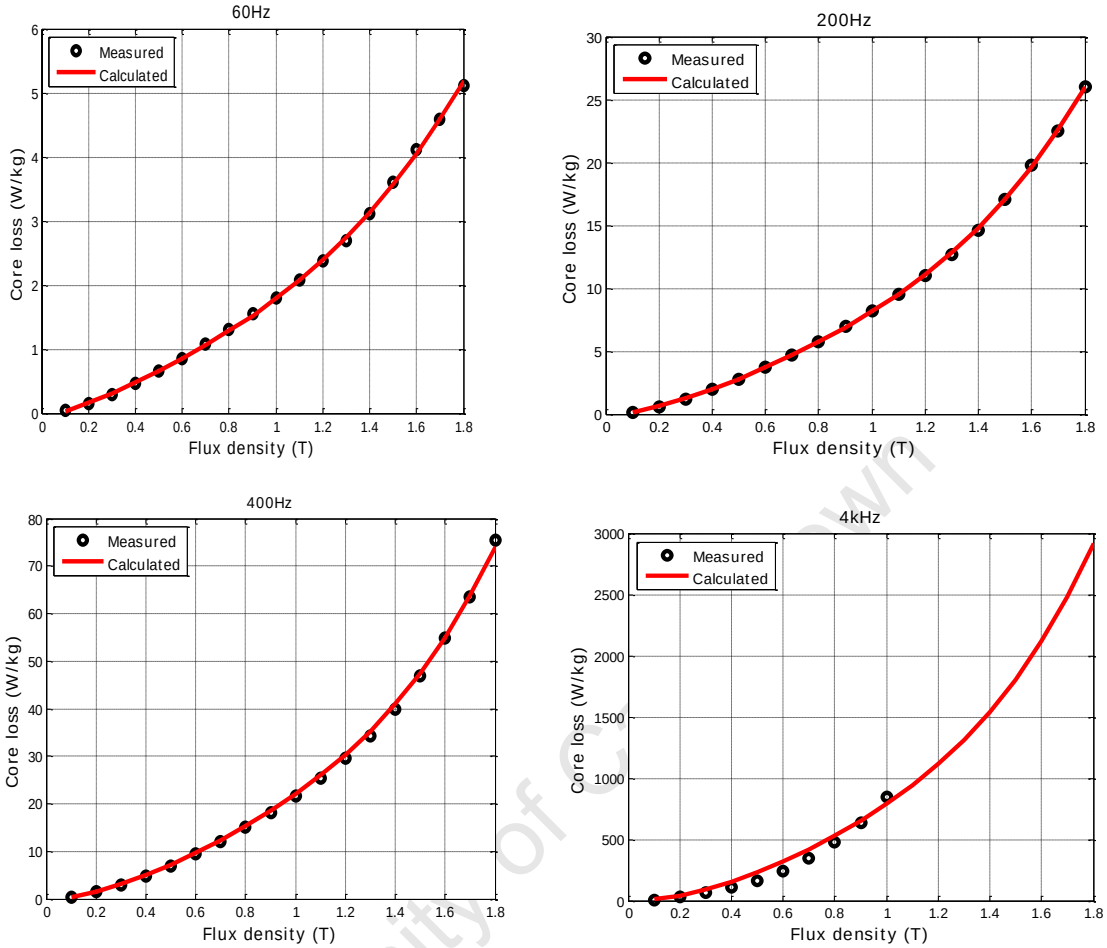

Fig. 3.16b Measured and calculated core loss results for 35H300 steel at 60 to 4kHz

3.4 CORE LOSS MODELS COMPARISON

3.4.1 Models Comparison under Sinusoidal Excitations

The new model is compared with the modified Steinmetz's (used in SPEED PCBDC) and Bertotti's formulae (used in Flux 2D) to determine their accuracy. The measured data are obtained from Epstein and toroid frame measurements. Figures 3.17– 3.19 show clearly that the new model predicts losses better at all flux densities that the other two models. The models maximum relative errors are shown in Tables 3.2 and 3.3. The errors are referenced to the measured results. The new model is satisfactory based on the general acceptable accuracy of +/-10%. The coefficients are calculated only once and better prediction accuracy is possible at all flux densities and

frequencies compared to the other two models. It can be concluded that the improved model is better than the conventional models.

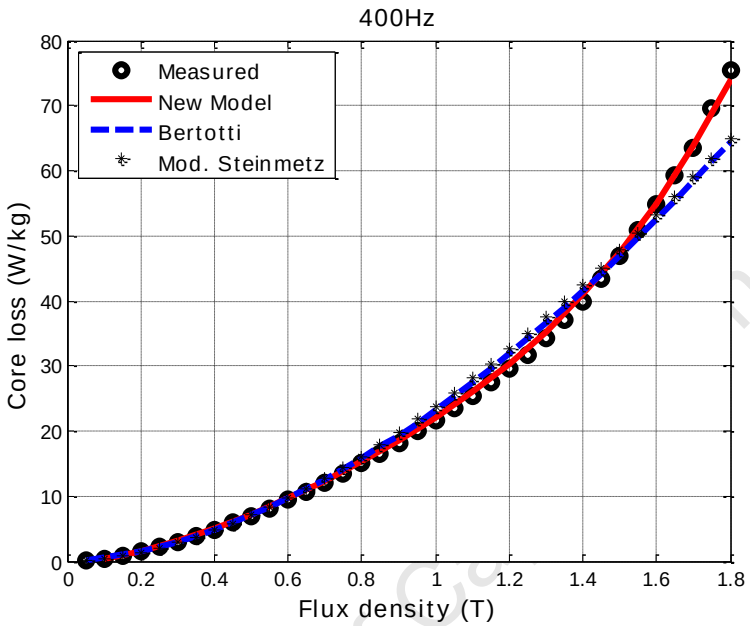

Fig. 3.17 Core Loss model comparison: 35H300 at 400Hz

Table 3.2 Core Loss model comparison: 35H300 at 400Hz

		35H300 at 400Hz					
B	Measured	Mod Stein.	Error	Bertotti	Error	New Model	Error
(T)	(W/kg)	(W/kg)	(%)	(W/kg)	(%)	(W/kg)	(%)
0.10	0.38	0.41	-7.82	0.49	-30.47	0.38	-0.50
0.20	1.45	1.38	4.82	1.54	-6.18	1.59	-9.50
0.40	4.84	4.73	2.26	4.90	-1.19	4.97	-2.71
0.70	12.10	12.75	-5.32	12.62	-4.30	11.91	1.58
1.00	21.64	23.80	-9.98	23.24	-7.39	21.44	0.95
1.20	29.47	32.63	-10.70	31.83	-7.98	29.57	-0.32
1.30	34.34	37.43	-9.00	36.56	-6.44	34.53	-0.53
1.40	39.77	42.49	-6.83	41.57	-4.51	39.99	-0.54
1.50	46.86	47.78	-1.96	46.86	0.00	46.71	0.32
1.55	50.94	50.51	0.84	49.61	2.60	50.76	0.34
1.60	54.74	53.29	2.65	52.43	4.23	54.46	0.53
1.65	59.29	56.13	5.33	55.32	6.71	59.08	0.36
1.70	63.62	59.03	7.22	58.27	8.41	63.98	-0.56
1.75	69.57	61.98	10.91	61.30	11.89	70.00	-0.62
1.80	75.34	64.98	13.76	64.39	14.54	75.40	-0.08

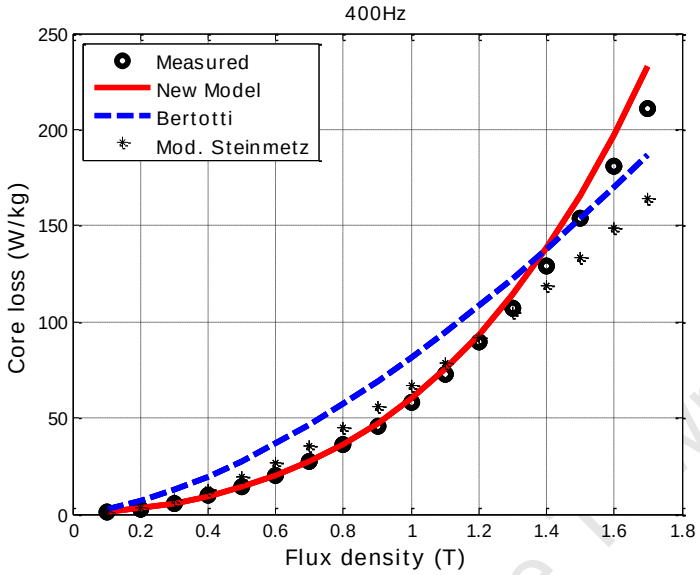

Fig. 3.18 Core Loss model comparison: 8050 steel at 400Hz

Table 3.3 Core Loss model comparison: 8050 steel at 400Hz

		8050 steel at 400Hz					
B	Measured	Mod Stein.	Error	Bertotti	Error	New Model	Error
(T)	(W/kg)	(W/kg)	(%)	(W/kg)	(%)	(W/kg)	(%)
0.10	0.94	0.91	3.97	2.36	-150.16	0.91	3.32
0.20	2.74	3.39	-23.57	6.79	-147.82	3.00	-9.35
0.30	5.46	7.32	-34.06	12.64	-131.64	5.82	-6.61
0.40	9.83	12.59	-28.00	19.67	-100.04	9.50	3.37
0.50	14.26	19.10	-33.96	27.75	-94.66	14.21	0.31
0.60	20.13	26.75	-32.87	36.79	-82.76	20.13	-0.02
0.70	27.39	35.43	-29.38	46.72	-70.59	27.47	-0.29
0.80	36.02	45.06	-25.11	57.49	-59.61	36.43	-1.14
0.90	45.90	55.56	-21.03	69.05	-50.43	47.25	-2.94
1.00	58.15	66.84	-14.95	81.38	-39.95	60.19	-3.51
1.10	72.40	78.86	-8.91	94.44	-30.43	75.49	-4.26
1.20	89.23	91.55	-2.60	108.21	-21.27	93.43	-4.70
1.30	107.88	104.88	2.78	122.66	-13.70	114.28	-5.93
1.40	129.34	118.83	8.13	137.78	-6.53	138.35	-6.97
1.50	153.56	133.36	13.15	153.56	0.00	165.93	-8.06
1.60	180.72	148.46	17.85	169.97	5.95	197.34	-9.19
1.70	211.02	164.14	22.22	186.99	11.39	232.90	-10.37

The loss coefficients used in the three models are calculated using measured loss data from 50 to 400Hz. The coefficients are all positive except the *b* coefficient in the modified Steinmetz's formula (3.5). Figure 3.19 shows the loss predictions for the 8050 steel at 3.2kHz. The new model in (3.16) estimates losses better than the other models even at frequencies not used in loss coefficient calculations. Calculating the loss coefficients at 3.2kHz using Bertotti's formula (3.9) results in a negative excess loss coefficient k_{ex} because the eddy current losses is larger than the total measured loss as shown in Figure 3.2. Therefore, it can be concluded that there is a frequency limit at which the coefficients can be calculated without Bertotti's formula becoming invalid. This limit is dependent on the type of material and thickness.

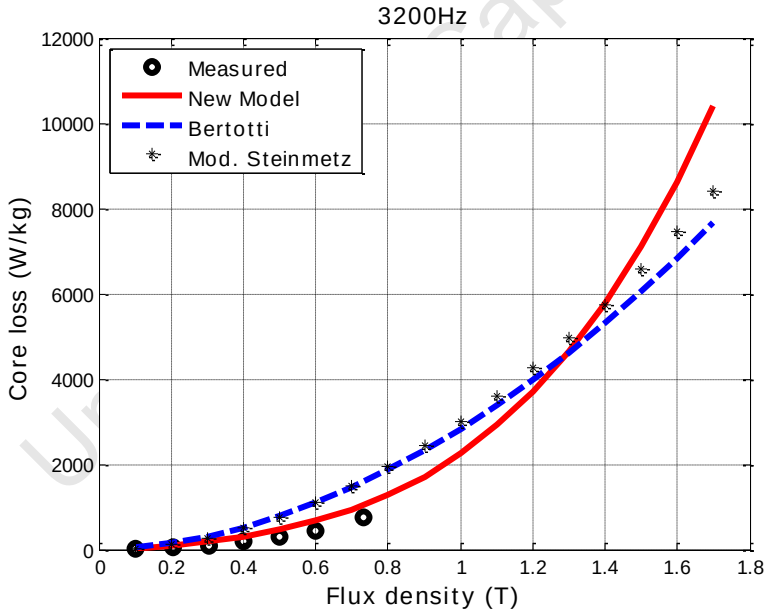

Fig. 3.19 Core Loss model comparison: 8050 Gauge steel of 3.2kHz

3.4.2 Model Comparison under Non-sinusoidal Excitations

The previous comparison has been done when the material is subjected to sinusoidal flux density waveforms. The flux density waveforms in electrical machine laminations are hardy sinusoidal as shown in the Traction motor

design in Chapter 5. Figure 3.20a shows the averaged flux density waveform found in the tooth of a Permanent Magnet Synchronous traction motor at 1.5T, 110Hz (35H300 steel). This is due to the presence of the magnets and control strategy generating non-sinusoidal current waveforms.

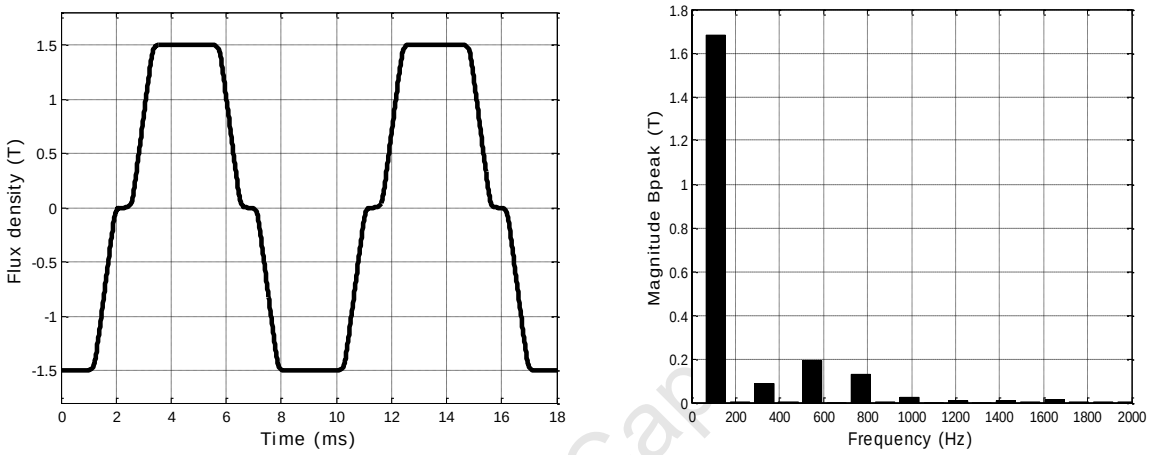

(a) flux density waveform (b) harmonic spectrum

Fig. 3.20 Tooth flux density waveform and harmonic spectrum at 110Hz

There are two methods used to estimate core loss under non-sinusoidal waveforms. The most common is the Fourier Series Method [11]-[13] despite the fact that the system in nonlinear. The second is the direct method where the dynamic losses (eddy and excess loss components) are expressed as rate of change of flux density - *dB/dt*. Each method is explored and results are presented below.

A. Fourier Series Method

In Fourier series method, the non-sinusoidal flux density waveform is decomposed into a series of sinusoidal waveforms. Figure 3.20b shows the spectrum of the waveform with 110Hz, 550Hz and 770 Hz as frequency of concern. Core loss calculations are done by calculating the loss at each harmonic and summing each loss to get the total loss. The shape of the waveform is not required.

The measured loss data has to be available at each frequency of concern to avoid data interpolation or extrapolation. This method has its limitations as the higher order harmonics are excluded and saturation effects included only to the extent of the additional harmonics, but superposition is still assumed. The idea here is to compare the models under non-sinusoidal excitations.

Table 3.4 shows the harmonic loss calculated at 110, 550 and 770Hz respectively. The total harmonic loss is 55% higher than the actual waveform measured loss, verifying the limitation of the Fourier method. The new model performs closely to loss harmonic values as shown by the relative error.

Table 3.4 Core loss calculation using Fourier series

Frequency (Hz)	B (T)	Loss Harmonic (W/kg)	Mod. Stein. (W/kg)	Error (%)	Bertotti (W/kg)	Error (%)	New Model (W/kg)	Error (%)
110.00	1.67	8.80	7.50	14.77	6.67	24.20	8.89	-1.02
550.00	0.19	1.37	1.53	-11.63	1.99	-45.19	1.37	-0.25
770.00	0.13	1.12	1.12	-0.41	1.55	-38.96	1.10	1.38
	Total	11.29	10.15	10.07	10.21	9.53	11.36	-0.69
Measured Loss: actual waveform 7.30 (W/kg)								

B. Rate of Change dB/dt Method

The improved model in (3.16) is generalized to include non-sinusoidal excitations and takes a form of

$$\overline{P} = P_h(f, B_p) + \frac{k_{ex}(f)}{2\pi^2}\frac{1}{T}\int\left(\frac{dB}{dt}\right)^2 dt + \frac{k_{ex}(f, B_p)}{\sqrt{2}\pi^{1.5}}\frac{1}{T}\int\left|\frac{dB}{dt}\right|^{1.5} dt \quad (3.25)$$

where P_h is the hysteresis loss, $\frac{dB}{dt}$ is the flux density rate of change over one cycle. Bertotti's formula and modified Steinmetz are also expressed in similar form in equations (3.10) and (3.12). The three formulae use the coefficients calculated with sinusoidal flux density because the loss data is readily available from manufacturers. The hysteresis loss is expressed as rate-

independent, depending only on the peak of the flux density waveform. The dynamic losses are rate dependant accounting for the shape of the flux density waveform. Expressing these terms in this manner is accepted by many researchers [2] [15] [18] [21].

The materials tested are the 35H300 Japanese steel and the 8050 Italian steel. The measured loss data for the 35H300 steel under non-sinusoidal waveforms are obtained by exciting the Epstein frame with the derivative of the flux density waveform as shown Figure 3.21 and measure losses at different magnitude and frequency. The relationship between voltage and flux density is given by the Faraday's equation as follows,

$$V_s = N_s A \frac{dB}{dt} \tag{3.26}$$

where N_s is the secondary turns and A is the area of the sample. During loss estimation, the flux density waveform over one electrical cycle is required. In this case, the voltage waveforms are captured during tests. dB/dt is calculated numerically (or analytically) and its value is substituted in the respective models. Alternatively, dB/dt can be replaced by $V_s/(N_sA)$, to avoid mathematical manipulations. The two representations yield the same results as indicated by (3.26). Similar procedure is followed for the 8050 steel loss measurements. The flux density waveforms for the 8050 steel are shown in Chapter 4.

Figures 3.22 and 3.23 show the predicted and measured results under non-sinusoidal excitations. Bertotti and modified Steinmetz formulae show similar relationships under sinusoidal excitation, which Bertotti's model predicts higher losses than Steinmetz at high flux densities. The new model produces better results and is applicable to any waveform; hence any machine topology is covered. For this material, Bertotti over estimates while

Steinmetz under estimates. The error becomes more evident when the specific core loss is multiplied by the total mass of the motor and also operating at high frequencies. The error also depends on the material used.

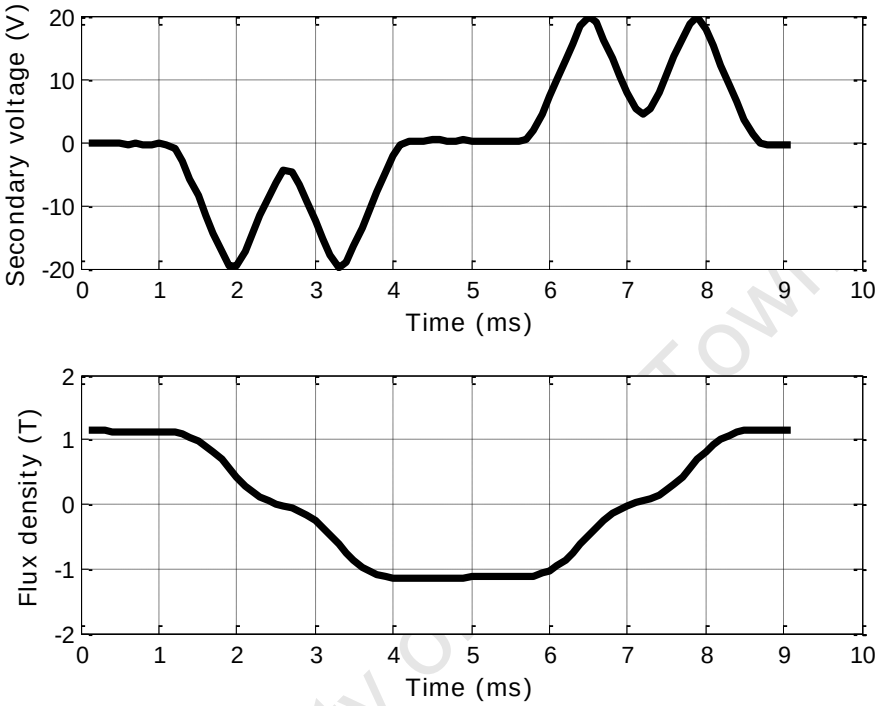

Fig. 3.21 Secondary voltage and flux density waveforms

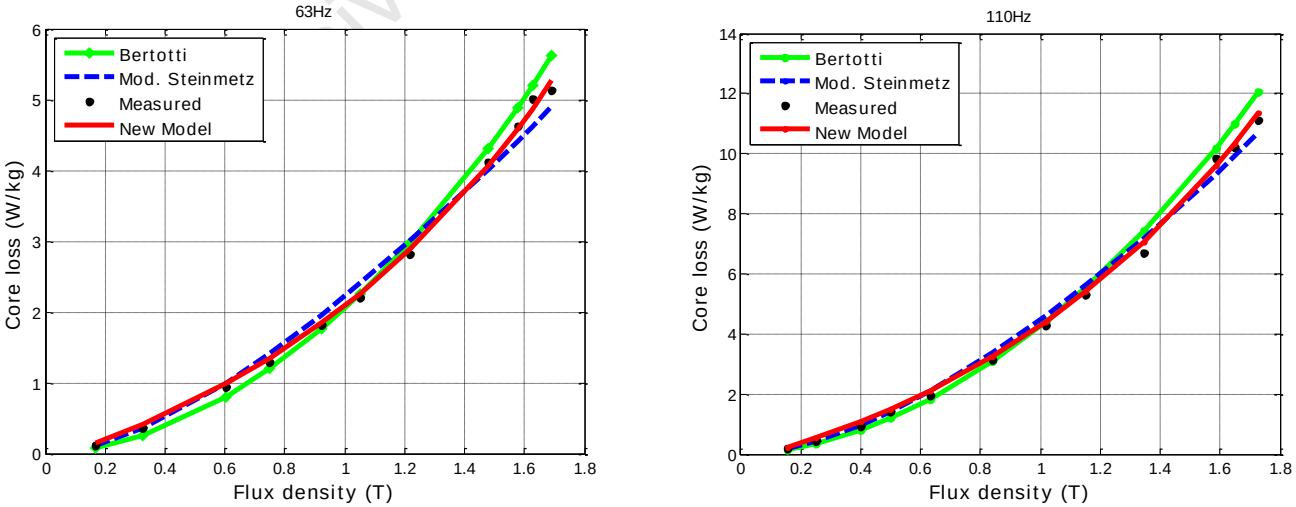

Fig. 3.22 Models comparison under non-sinusoidal excitation at 63Hz and 110Hz: 35H300 steel

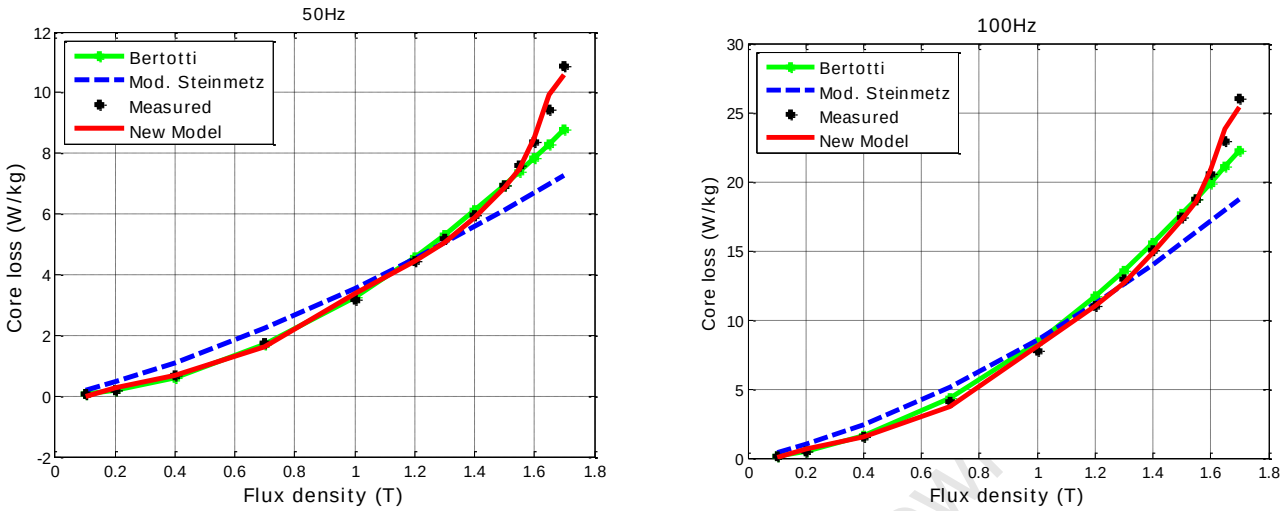

Fig. 3.23 Models comparison under non-sinusoidal excitation at 50Hz and 110Hz: 8050 steel

3.5 CONCLUSIONS

- The Steinmetz and classical formulae predict the same core losses at various frequencies and materials provided the loss coefficients are recalculated at frequency of concern. The skin effect must be accounted for when using classical formula at high frequencies. Limited loss data affect loss prediction at higher frequencies, resulting in a significant deviation from measurements, especially for the classical formula. The Steinmetz constant, n =1.6, is not generically applicable to all materials. The modified Steinmetz model does not necessary predict better results that the original Steinmetz's formula, especially at high flux densities.

- Berttoti's formula shows improvement when compared to the classical model with physical basis, especially when estimation is done with limited loss data. However, Bertotti's formula still under estimates losses at high flux densities. Also, the formula is invalid at high frequencies.

- Core loss prediction at frequencies not used during loss coefficient calculations is not recommended for conventional core loss models

- The proposed model performs better than the modified Steinmetz used in SPEED PCBDC Software and Bertotti's model used in Cedrat/Magsoft Flux 2D/3D. The model shows good correlation with measured results under both sinusoidal and non-sinusoidal excitations.

Chapter 4

4. APPLICATION OF IMPROVED LOSS CALCULATION IN INDUCTION AND PM MOTORS

4.1 OVERVIEW

The applicability and accuracy of the improved core loss calculation formula are examined on the toroidal fixture, induction motor test bench and permanent magnet synchronous motor (PMSM). The Flux2D finite element software is used to simulate the toroid and the motors. The accuracies of the Flux2D core loss formula (Bertotti's formula) and modified Steinmentz's formula are also examined and compared with the new formula. An alternative method of calculating core losses without using the formulae is also presented and tested in induction and PM motors with acceptable accuracy. The effect of core loss measured data on motor heating is also presented.

4.2 CORE LOSS CALCULATIONS FOR THE TOROID

The accuracy of the core loss models is examined using the toroid frame in Figure 4.1. The toroid core loss measurements and simulated results are presented next.

4.2.1 Core Loss Measurements

The core loss measurements are done using the laboratory test bench and also verified with the measurements from KJS Associates Company. The toroid consists of four strips of 8050 Italian steel of 0.5 mm thickness each. It has 600 primary turns and 400 secondary turns.. The thickness of the toroid is large enough to reduce the effect of cutting stresses, which affect the core loss measurement results and are difficult to model. A table of desired peak flux densities B_p (0.1 − 2T or higher) and secondary voltage V_s is developed using the formula given by

$$V_s = \sqrt{2}\pi N_s A f B_p \tag{4.1}$$

N_s is the number secondary turns, A is the area of the laminations and f is the test frequency. The primary excitation voltage is obtained by multiplying the turn ratio (600/140) by the secondary voltage.

4.2.2 Core Loss Predictions

The toroid is modeled using the Flux2D Finite Element (FE) package [27] as shown in Figure 4.1. The primary windings are excited with the same supply conditions used in the measurements using the simple circuit in Figure 4.1.

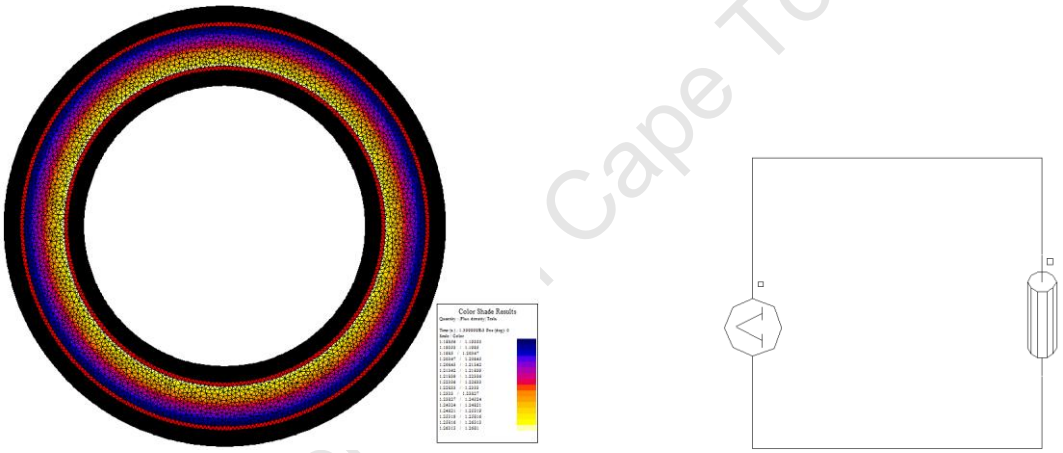

Fig.4.1 Toroid with 8050 steel and electrical circuit

$$\overline{P} = k_h B_p{}^2 f + \frac{\sigma d^2}{12}\frac{1}{T}\int\left(\frac{dB}{dt}\right)dt + \frac{k_{ex}}{\sqrt{2}\pi^{1.5}}\frac{1}{T}\int\left|\frac{dB}{dt}\right|^{1.5} dt \tag{4.2}$$

$$\overline{P} = k_h B_p{}^{a+bB} f + \frac{k_e}{2\pi^2}\left[\frac{dB}{dt}\right]_{rms} \tag{4.3}$$

$$\overline{P} = P_h(f, B_p) + \frac{k_{ex}(f)}{2\pi^2}\frac{1}{T}\int\left(\frac{dB}{dt}\right)^2 dt + \frac{k_{ex}(f, Bp)}{\sqrt{2}\pi^{1.5}}\frac{1}{T}\int\left|\frac{dB}{dt}\right|^{1.5} dt \tag{4.4}$$

The Flux2D software uses Bertotti's formula (4.2). The modified Steinmetz's formula (4.3) and the new formula (4.4) are modeled in MATLAB. The loss coefficients are calculated using the measured data from 50Hz to 400Hz. Figures 4.2 and 4.3 show the measured and calculated results at 100Hz and 400Hz respectively. There is an insignificant difference between Berttoti's model and the new model at low frequencies (<100Hz) for this material. This is not generic and is dependent on the material used as shown in Chapter 3. The maximum deviation of 20% is significant at high frequencies as shown in Figure 4.3, where the new formula estimates core losses better than the Bertotti's formula. The deviation at higher frequencies is due to the skin effect neglected by Bertotti's formula. The new formula deviates slightly from measurements as high flux densities as shown in Figure 4.3.

The modified Steinmetz's formula has been found to under estimates losses (0 - 35% error) at all tested frequencies as shown Figures 4.2 and 4.3. This has been observed in several material tested, some of which are shown in Chapter 3.

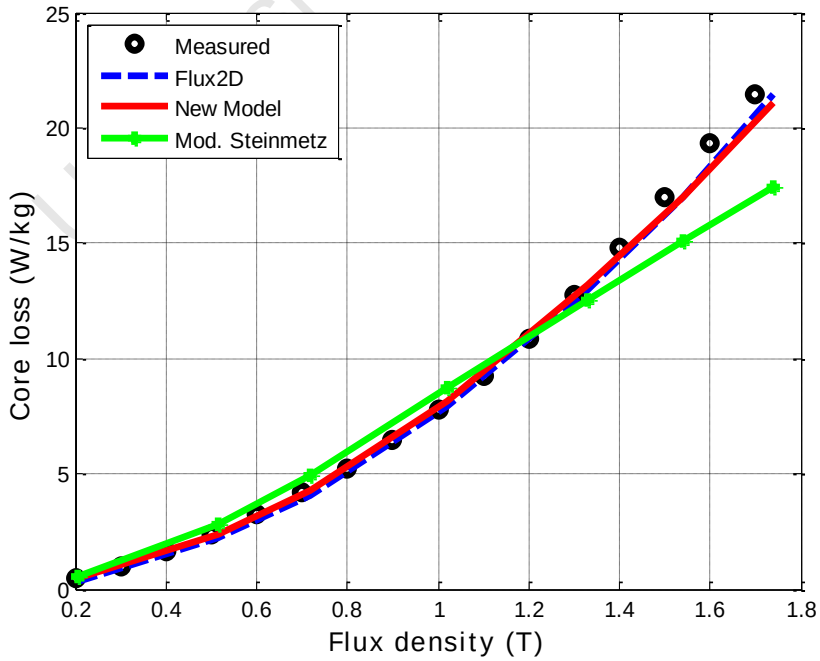

Fig.4.2 Toroid measured and calculated results at 100Hz

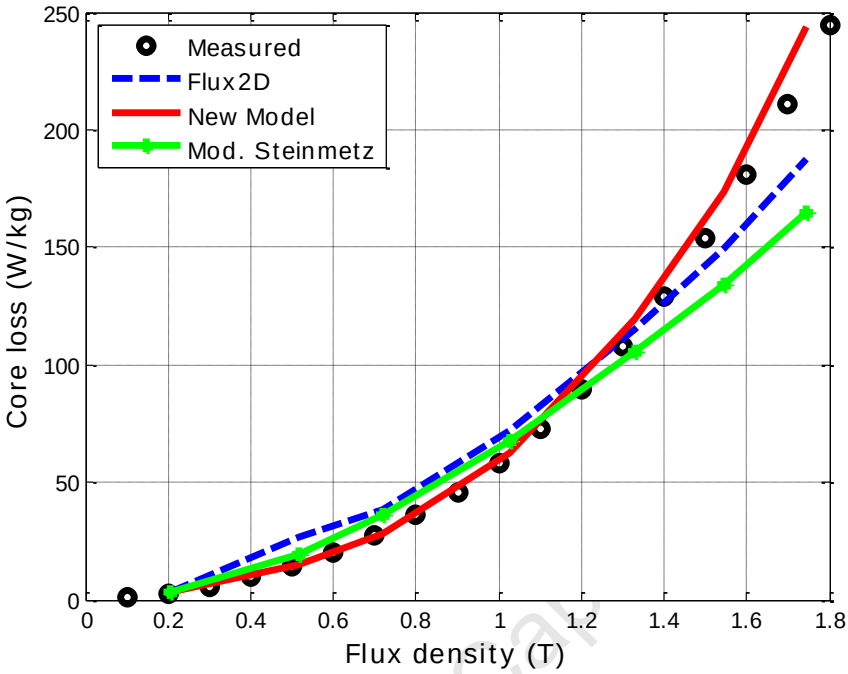

Fig.4.3 Toroid measured and calculated results at 400Hz

4.3 CORE LOSS CALCULATIONS FOR THE INDUCTION MOTOR

The accuracy and applicability of the new formula is also examined in an induction motor test bench.

4.3.1 Core Loss Measurements

The core loss measurement results from an 11kW, 400V, 50Hz induction motor test bench is used in this analysis. The test bench was developed and tested by Boglietti in [29]. A normal induction motor with 8050 electrical steel laminations of 0.5mm thickness was modified. The squirrel cage rotor bars were replaced with non-conductive material. Therefore, the motor cannot start on its own. The rotor slots are closed. The reason behind this modification was to be able to accurately remove the rotor winding and space harmonics losses from core loss measurements, which are otherwise difficult to calculate and separate. The induction motor test bench was connected to a

synchronous motor since it cannot run by itself and also to compensate for mechanical losses.

The core loss in an induction motor is measured by subtracting other losses calculated directly or indirectly from the input power as follows

$$P_{core} = P_{input} - P_{cu\_Stator} - P_{cu\_rotor} - P_{mech} \tag{4.5}$$

Core loss measurements were done at no-load when the motor is excited with 50Hz sinusoidal supply of variable voltage. The motor was run at synchronous speed and the core loss calculated using

$$P_{core} = P_{input} - P_{cu\_Stator} \tag{4.6}$$

since the rotor winding losses (copper losses) are zero and the mechanical losses are accounted by the synchronous motor.

4.3.2 Core Loss Prediction using Improved Formula

The induction motor lamination view is shown in Figure 4.4. It has 36 slots with distributed short pitched three phase windings and 28 rubber rotor bars. The motor is simulated and analyzed using the Flux2D software as shown in Figure 4.4. The simulations are performed in a transient magnetic mode with rotor motion to account for rotational effects in the stator tooth and yoke flux densities. The motor is excited with the same supply conditions used in the measurements. The excitation is provided by the electrical circuit coupled to geometry in Figure 4.5.

Bertotti's formula in (4.2) is already embedded in Flux2D and the new core loss formula in (4.4) is programmed in MATLAB to calculate core losses. Both formulae require flux density waveforms from the Flux2D postprocessor. The

loss coefficients must be known and are calculated prior to loss prediction using the 8050 steel measured loss data.

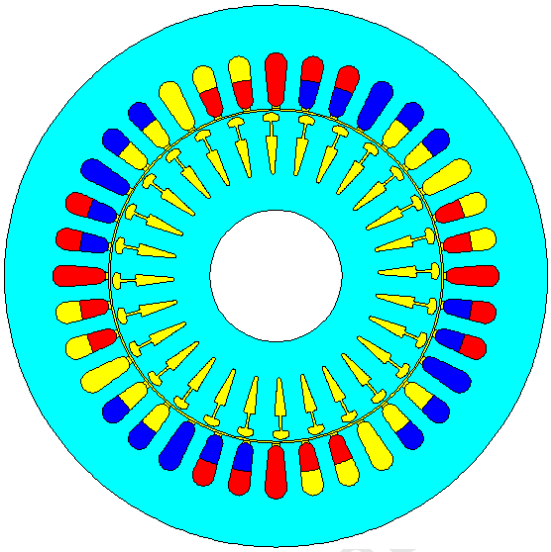

Fig. 4.4 Lamination view of the 11 kW induction motor

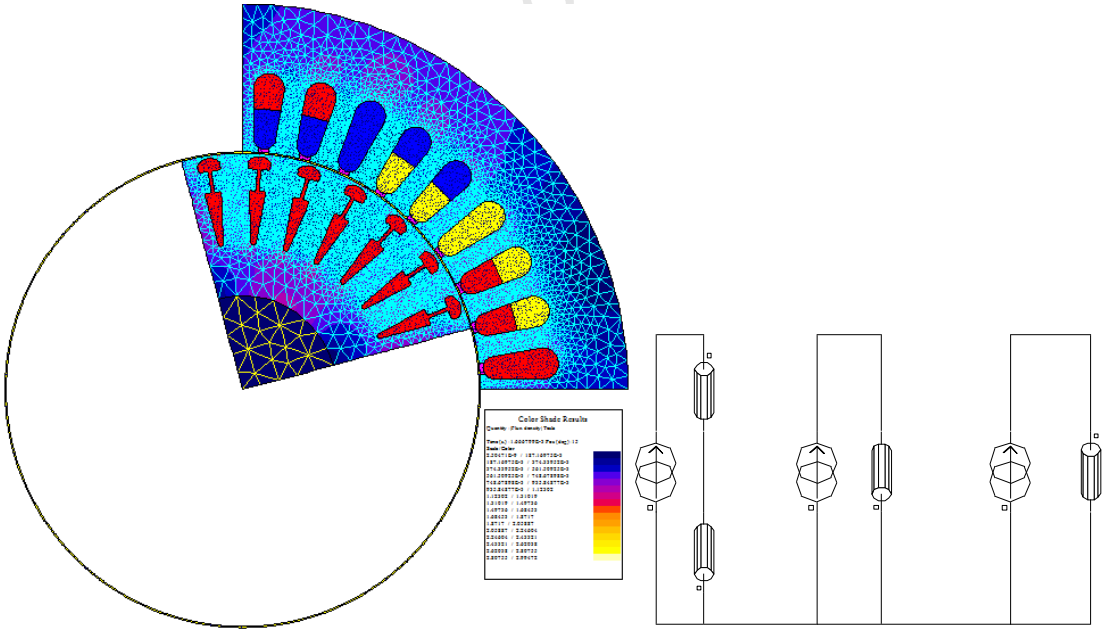

Fig. 4.5 Induction motor geometry and electrical circuit for excitation

Figure 4.6 shows the measured and predicted core loss results using the new formula. The new formula estimates core losses with good accuracy at all flux densities (or voltages). Figure 4.7 shows the comparison between the measured and core loss predictions using both formulae. The proposed model predicts losses better than Bertotti's model relative to the measured results. The deviation of Bertotti's model is visible and significant at high voltages, close to rated, and this is the operating point of the induction motor.

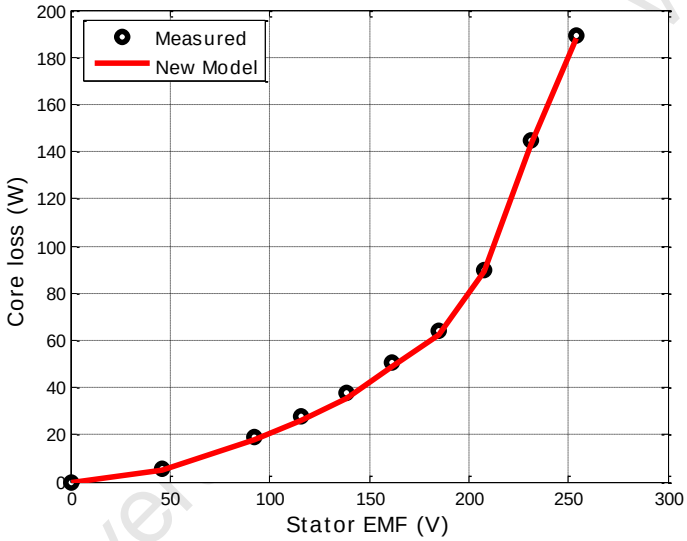

Fig. 4.6 11kW IM core loss results from measurement and new formula

The exact core loss values in Figures 4.6 and 4.7 are clearly shown in Table 4.1. The new model has a maximum deviation of 7.6% and Berttoti's model has a maximum deviation above 10% from measurement values. The new model shows improvement to the current Flux2D model.

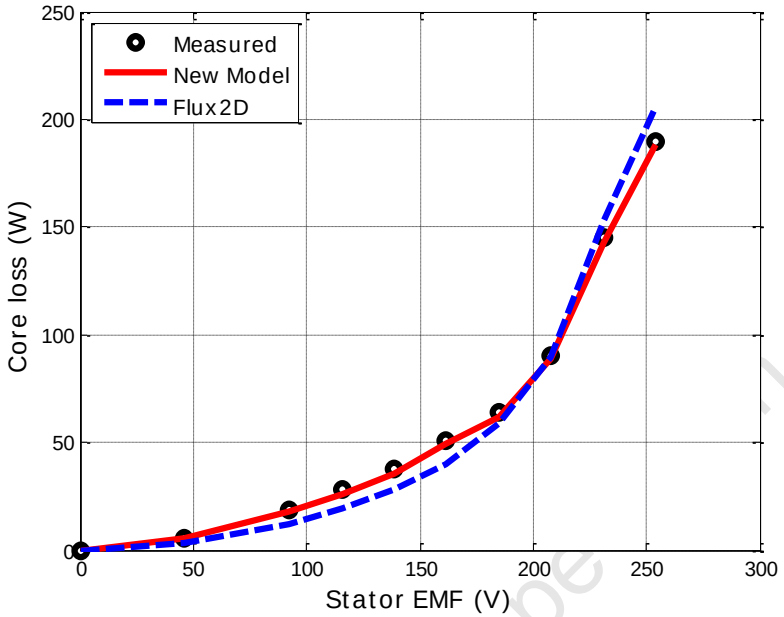

Fig. 4.7 Measured and predicted core loss results of the 11kw IM at no load

Table 4.1 Measured and predicted loss results of the 11kw motor at no load

EMF	Measured Loss	Predicted loss in W at 50Hz		% Error	
(V)	(W)	Flux 2D	New Model	Flux 2D	New Model
0	0	0	0	0	0
46	5.5	3.0	5.2	44.7	6.0
92	19.0	12.2	18.0	35.8	5.2
115	28.0	19.2	26.1	31.5	7.0
139	38.0	28.2	35.1	25.8	7.6
162	50.5	40.2	49.0	20.4	3.0
185	64.0	58.6	62.0	8.5	3.1
208	90.0	89.9	89.0	0.1	1.1
231	145.0	153.4	143.0	-5.8	1.4
254	190.0	206.1	188.0	-8.5	1.1

4.3.3 Core Losses from measurements using the Laboratory Test Equipment

An alternative method of determining motor core losses during the design process is also investigated. The core loss formulae are not used in this method. The motor is analyzed using finite element or analytical tools, and the resulting flux density waveforms are obtained for specific operational conditions. The associated voltage waveforms are then excited into a Toroid or Epstein frame and core losses measured. The specific losses (W/kg) from the frame are then multiplied by the weight (kg) of the stator yoke, teeth or any region of interest to determine the total motor core losses.

For the induction motor is the previous analysis, the flux density waveforms in the stator yoke and teeth are already available from the Flux2D postprocessor. Figure 4.8 and Figure 4.9 show the averaged stator yoke and tooth flux density waveforms for two electrical cycles. The waveforms in Figure 4.8 are obtained for a low voltage excitation and are sinusoidal as indicated by the respective harmonic spectra. The derivatives of these waveforms (voltage) can easily be calculated from

$$V = NA\frac{dB}{dt} \tag{4.7}$$

Where V is voltage, A is the sectional area of the geometry and N is the number of turns of the coil. The voltage waveforms are then excited into the primary winding of the 8050 steel Toroid frame in Figure 4.10 to measure specific losses. Alternatively, the manufacturer's specific loss data may be used, if available, since they are measured when the material is subjected to sinusoidal flux densities.

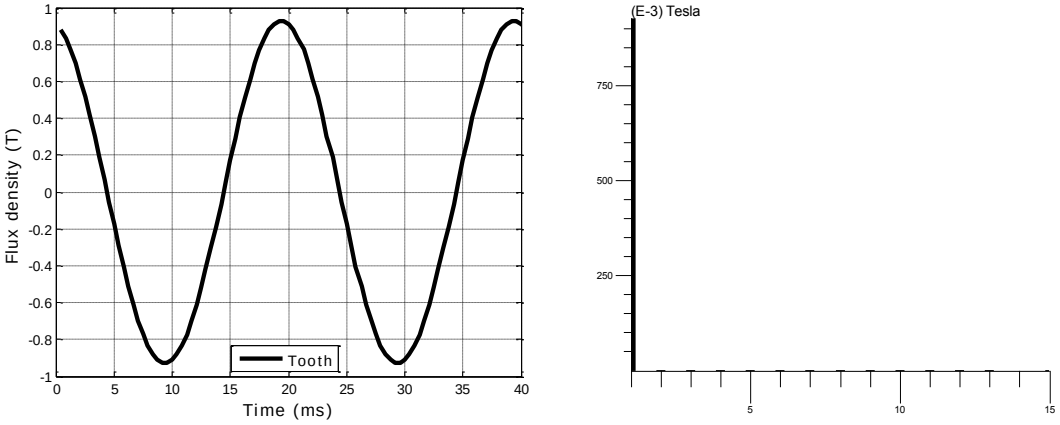

(a) Tooth

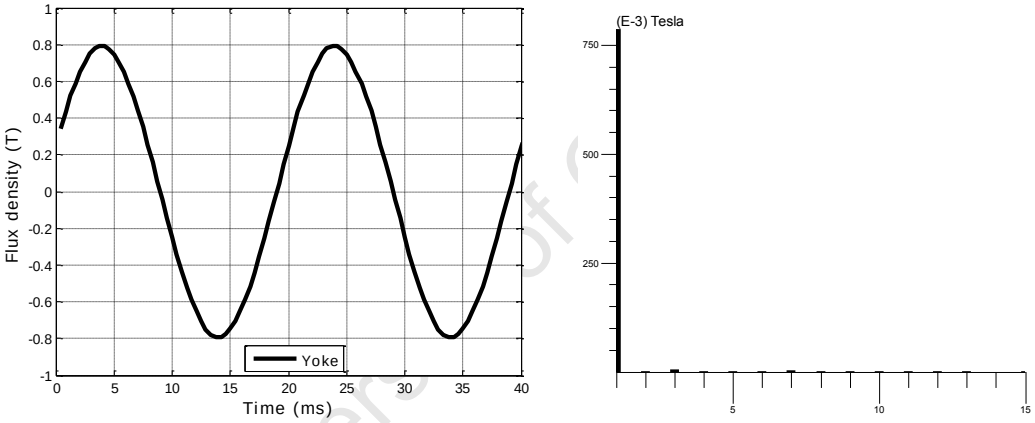

(b) Yoke

Fig. 4.8 Tooth and Yoke flux density waveforms and harmonic spectrum at low voltage

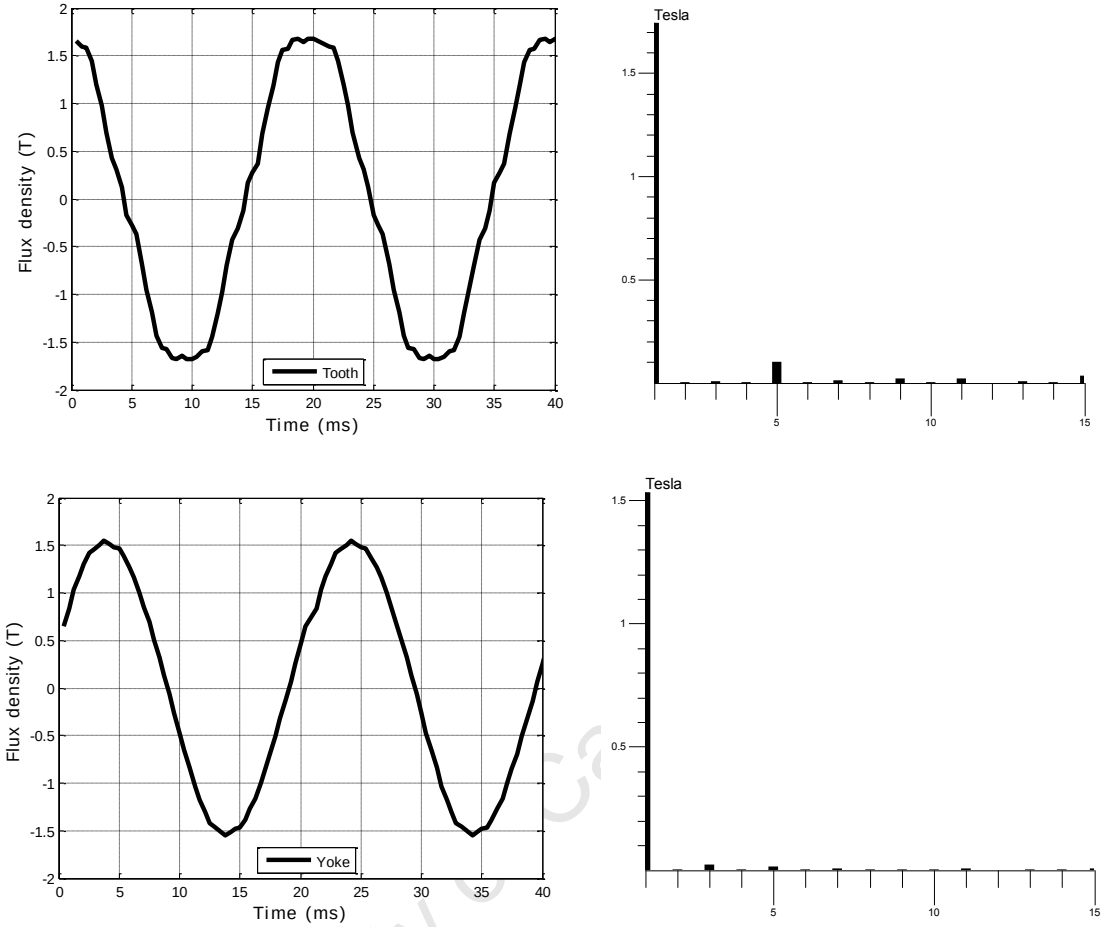

Fig. 4.9 Tooth and Yoke flux density waveform and harmonic spectrum at high voltage

Fig. 4.10 8050 electrical steel Toroid frame

The flux density waveforms in Figure 4.9 are obtained at higher voltages and are non-sinusoidal due to material saturation effects. The voltage waveforms are obtained using (4.7) and excited into the Toroid frame to measure specific core losses. The test bench discussed in Chapter 2 is used since it can generate arbitrary waveforms. Manufacturer's specific loss data are not available under non-sinusoidal flux densities. In this case, an alternative method is to use the harmonic spectra (Fourier series method) to determine specific losses. However, this method is not preferred due its limitation presented in Chapter 3.

Also, the flux density is a vector represented by radial and tangential components. Figure 4.11 shows the components obtained from the yoke section of the induction motor. In the tooth, the radial component B_{rad} is dominant and B_{theta} in the yoke. One assumption is to consider the effect of the dominant averaged component i.e. assumed that the flux density is alternating. Another assumption is to consider the flux density as rotational, measure specific core loss at each component and sum the results. The latter is well accepted in core loss calculation using formulae [11] [13] [30] [31] and therefore used here, although it is applied in measurements.

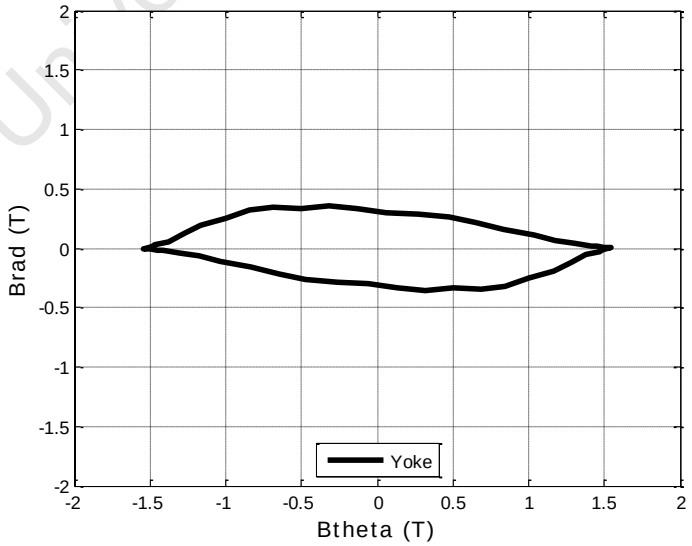

Fig. 4.11 Flux density B_{rad} and B_{theta} components

Figure 4.12 shows the measured and predicted results using the new formula and test frame specific core loss results ('direct method'). The direct method shows a good correlation with motor loss results (error <10%) as shown in Table 4.2. This method can be used on its own or to validate the formula provided that the core loss testing equipment and laminations are available.

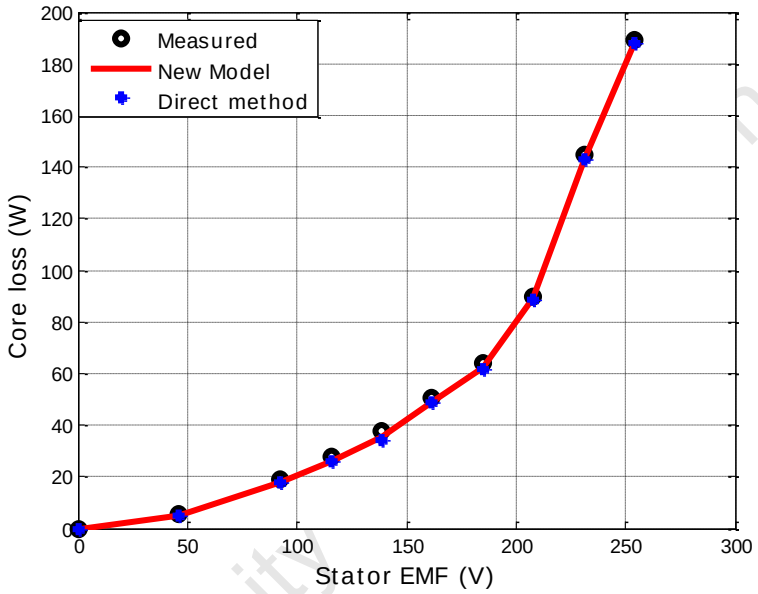

Fig. 4.12 No-load core loss measured results, 11kW IM motor and toroid

Table 4.2 Measured loss results from 11kw motor and toroid at no load

EMF (V)	Measured - Motor (W)	Measured - Toroid (W)	% Error
0	0.0	0.0	0.0
46	5.5	5.0	9.9
92	19.0	17.6	7.3
115	28.0	25.8	7.9
139	38.0	34.5	9.1
162	50.5	48.7	3.5
185	64.0	61.8	3.5
208	90.0	88.6	1.5
231	145.0	142.9	1.5
254	190.0	188.0	1.0

4.4 CORE LOSS CALCULATIONS FOR THE PM MOTOR

4.4.1 Core Losses from Measurements using the Laboratory Test Equipment

Further core loss calculations are also done in Permanent Magnet Synchronous Motor (PMSM) using equations (4.2) and (4.4), and the direct measurement method. Figure 4.13 shows the lamination view and flux density plot of a 4pole 24 slots PMSM at no-load. The lamination material is a 35H300 steel of 0.35mm thickness. The loss coefficients are also calculated before hand using the material loss data from the test bench.

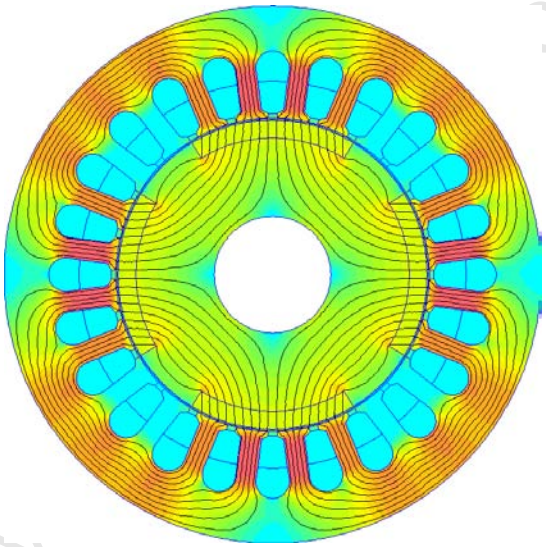

Fig. 4.13 Lamination view of a PM synchronous motor at no-load

The non-sinusoidal averaged tooth and yoke flux density waveforms are shown in Figure 4.14 and Figure 4.15. This is due to the presence of the magnets. The respective voltage waveforms required in the formulae (dB/dt term) and for excitation of the frames when using the direct method are also shown besides the flux density waveforms. In this case, the specific loss measurements are done using the Epstein frame at various frequencies up to 110Hz. The loss calculation procedure is the same as in the previous analysis.

The loss calculation in the PMSM is done from 0 - 3300rpm. Core loss prediction results using the two formulae and direct method are shown in Figure 4.16. Taking the direct method results as a reference, the improved model predicts better than Bertotti's model. Bertotti's model under estimate losses as frequency increases. Again, the new model shows improvement when compared to Bertotti's Model.

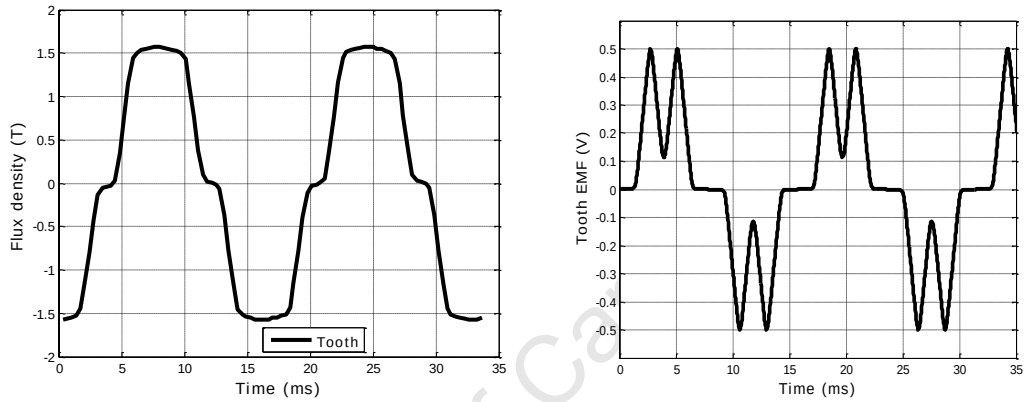

Fig. 4.14 Averaged stator tooth flux density and voltage waveform

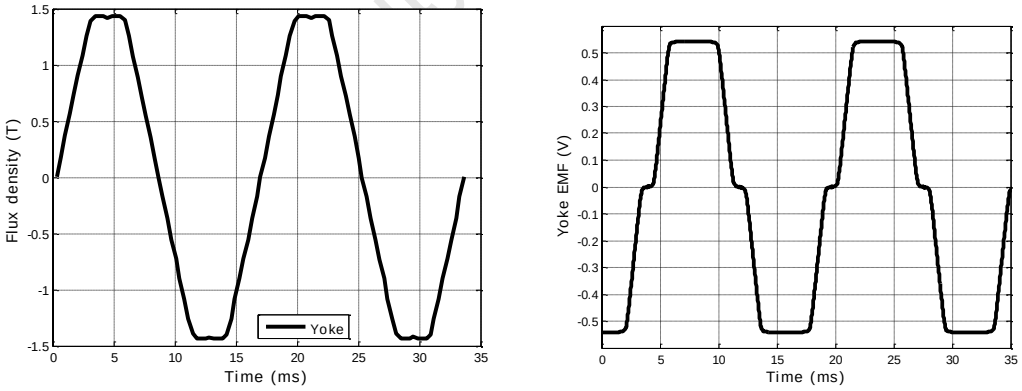

Fig. 4.15 Averaged stator yoke flux density and voltage waveform

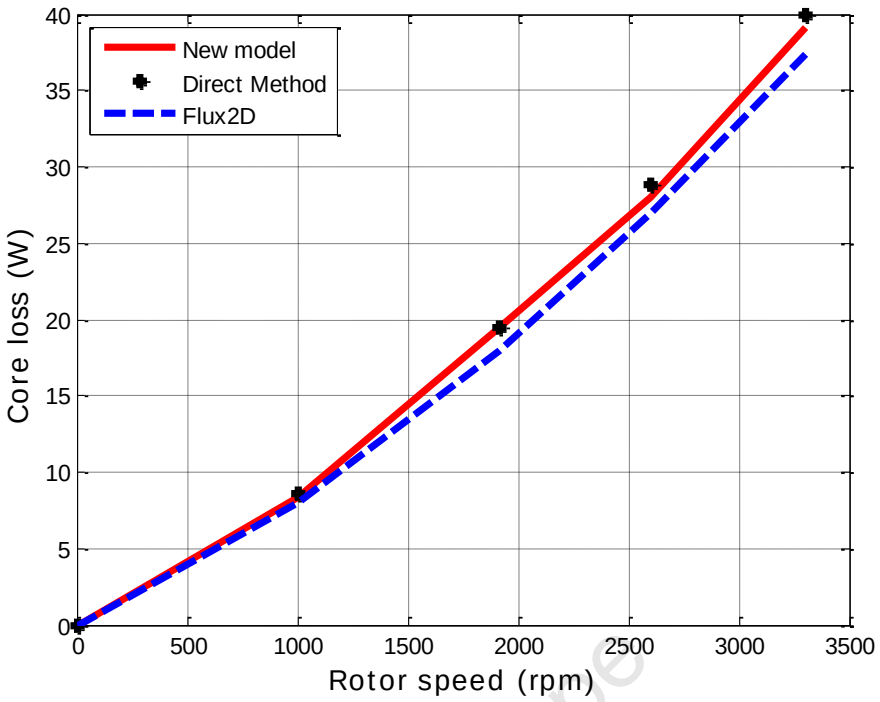

Fig. 4.16 PM Motor predicted core loss results using formulae and direct method

4.4.2 Effect of Core Loss Measurement Data

It has been mentioned in Chapter 2 that the core loss measurements are affected by frame and sample configuration, preparation, arrangement, annealing and core loss correction factors. In this case, the effect of sample preparation (laser and punched laminations) on core losses and heating is analyzed. Figure 4.17 shows the predicted core loss results at no load and rated load for the PM motors. The results are obtained using the laser and punched laminations core loss data from the same batch of material.

Figure 4.18 shows the temperature difference under load. It can be concluded that whenever there is core loss difference the heating will also be different. The core loss difference can be caused by using different formulas or using measured data from different testing frames (e.g. Epstein or Toroid). The temperature magnitudes will depend on the core loss magnitudes

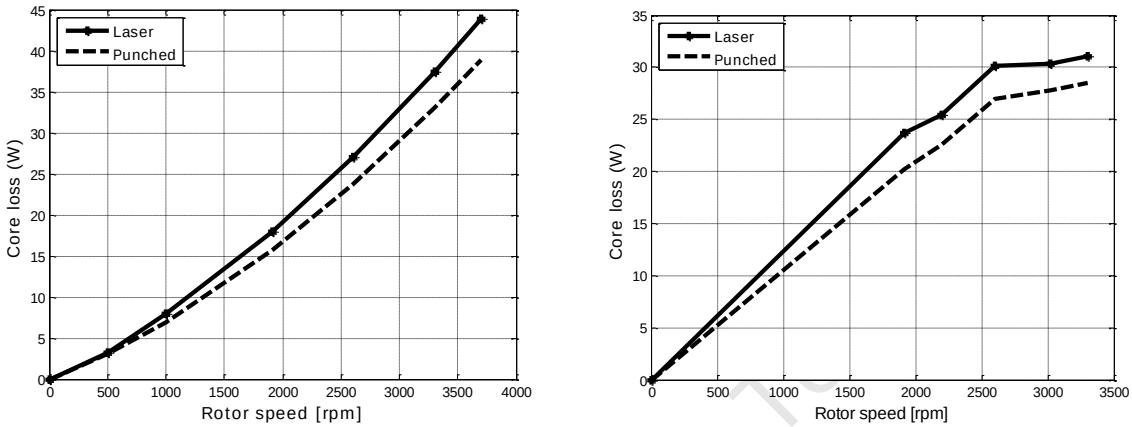

(a) No load (b) Under load

Fig. 4.17 Calculated core loss results at no-load and under load

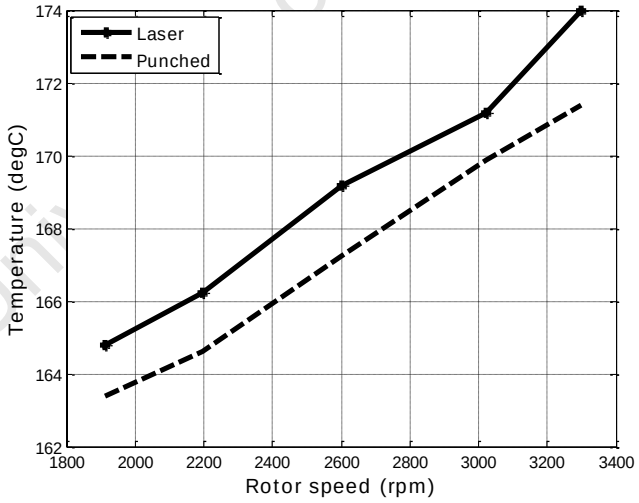

Fig. 4.18 PM motor laser and punched temperature results

4.5 CONCLUSIONS

- A promising tool to predict core losses is examined in electric machines. The model is applicable to both sinusoidal and non-sinusoidal cases. Furthermore, the model has a physical basis for the variation of the loss coefficients and good alignment with experimental data from the induction motor and toroid frame. The new model error range is 1.1% - 7.6% while the FEM (Bertotti) % error is between -8.5% - +44.7%.

- The modified Steinmetz model under estimates losses (0 - 35% error) at all tested frequencies.

- An alternative method is also presented which requires direct loss measurement from test frame; Toroid or Epstein. This method predicts the loss accurately although it requires the availability of advanced testing equipment and laminations.

- The motor heating is affected by the accuracy of the core loss measurement data and calculation formulae.

Chapter 5

5. PM MACHINE DESIGN AND INTERGRATION OF NEW CORE LOSS FORMULA INTO FLUX2D SOFTWARE

5.1 OVERVIEW

This chapter presents a Low Voltage High Current traction motor design with restrictions on physical size, maximum operating temperature and cooling. The design is performed using three software packages (Flux2D, PCBDC and FEMM) for comparison and validation. Emphasis is made on core loss calculations using each package. The prototype test results are presented and the effects of manufacturing on core losses are addressed. Finally, the integration procedure of the new core loss formula into the Flux2D software is addressed. Flux2D is used because MAGSOFT is part of the consortium.

5.2 TRACTION MOTOR APPLICATION AND SPECIFICATION

5.2.1 Motor Application

A Permanent Magnet Synchronous Motor (PMSM) is designed to drive a 24V battery-operated pallet truck in Figure 5.1. The drive schematic is shown in Figure 5.2. The motor is predicted to offer higher efficiency when compared to AC and DC motors of the same size and rating currently used in this application. This is due to the significant reduction in losses in the absence of rotor windings and brushes. The projected benefits of this design are longer battery lifespan and extended operating cycles.

Fig. 5.1 Battery-operated pallet truck (Raymond website)

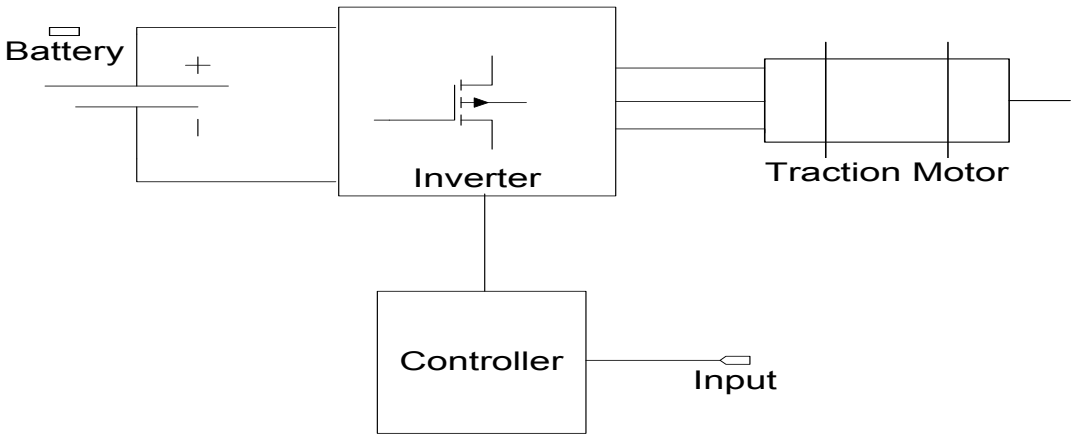

Fig. 5.2 Drive schematic of a battery-operated pallet truck

5.2.2 Motor Specification

The nominal voltage of the battery is 24Vdc. The motor is required to develop a full-load torque of 12 Nm at 1912 rpm base speed with minimum voltage of 21Vdc to account for battery discharge. Its power rating is therefore 2.4 kW at that speed. The maximum speed is 3300 rpm with a minimum torque of 4 Nm. The expected efficiency is above 80% at high speed in order to compete with DC and AC machines of the same size. The above specification must be met with the inverter voltage limited at $14.5V_{ac}$ line voltage at the motor terminals, maximum winding operating temperature below 180ºC and stator outer diameter below 120 mm. The motor should operate in both forward and braking modes without forced cooling.

5.3 MOTOR ELETROMAGNETIC DESIGN

5.3.1 Design Tools

The finite element (FE) tools used during the design are; a commercial FE software package, MagSoft Flux2D [27], and a freeware Finite Element Magnetic Method (FEMM) [32]. The later is flexible, i.e. it allows code modification and external programme linkages. The analytical tool used here is a commercial SPEED Brushless DC motor software (PCBDC) [15] coupled to Magnet2D FE package [33].

5.3.2 Design Challenges

The motor torque (alignment torque) is proportional to the back EMF voltage, and phase current divided by speed. The main problem is the low motor terminal voltage ($14.5V_{LLrms}$) resulting in high currents in order to reach the desired torque values. High currents lead to severe thermal conditions which limit the size and power capability of the motor. Heating becomes a major challenge especially when forced cooling is not provided. No fan is allowed for reliability reasons. Heat affects motor life and efficiency. To be specific, the magnets are exposed to demagnetization, and winding insulation to failure due to heat. All these require better quantification of winding and core losses.

The low terminal voltage also limits high speed operation and forces a delta winding configuration. Therefore, a sinusoidal EMF waveform is essential in order to eliminate circulating currents in the delta windings and to reduce torque ripple and heating. The EMF varies with temperature, creating a concern when sizing the motor, and start-ups during cold weather.

5.3.3 Motor Configuration

A four pole 24-slot radial PMSM with inset magnets in Figure 5.3 is chosen as the final design – a first of many designs envisaged for the traction motor project. The number of poles is optimized to meet the require speeds and torque while reducing core losses and increasing inductances required for high speed operations. The 24-slot configuration was initially chosen to fit closely to the lamination currently available for existing induction motors, with simple distributed windings to achieve sinusoidal back EMF and low torque ripple. The lamination material is a relatively inexpensive non-oriented steel with 0.35mm thickness. The outer diameter is 120mm and the stack length is 95mm. High energy Neodymium Iron Boron – NdFeB magnets are used.

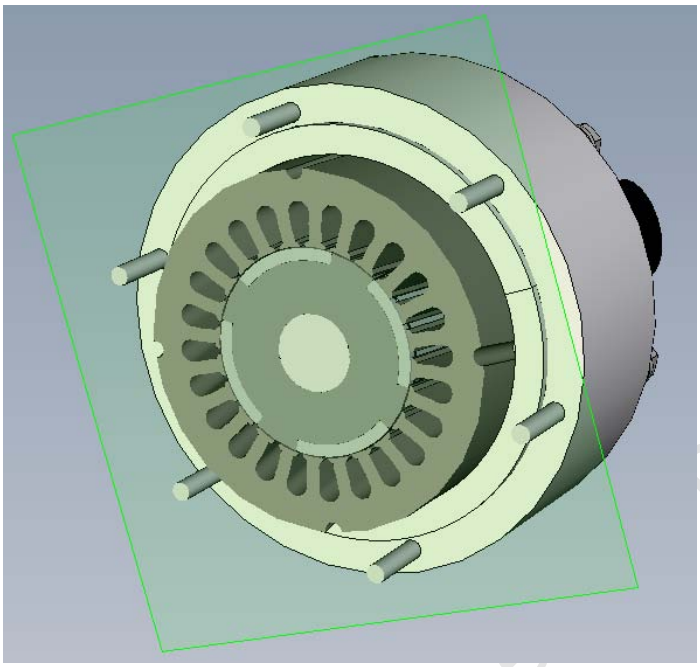

Fig. 5.3 PMSM 3D sectional view with housing

Figure 5.4 shows the surface and inset rotor magnet configurations analyzed using Flux2D and FEMM. The inset configuration offers additional reluctance torque for the same current and magnet volume without complicating the manufacture unduly.

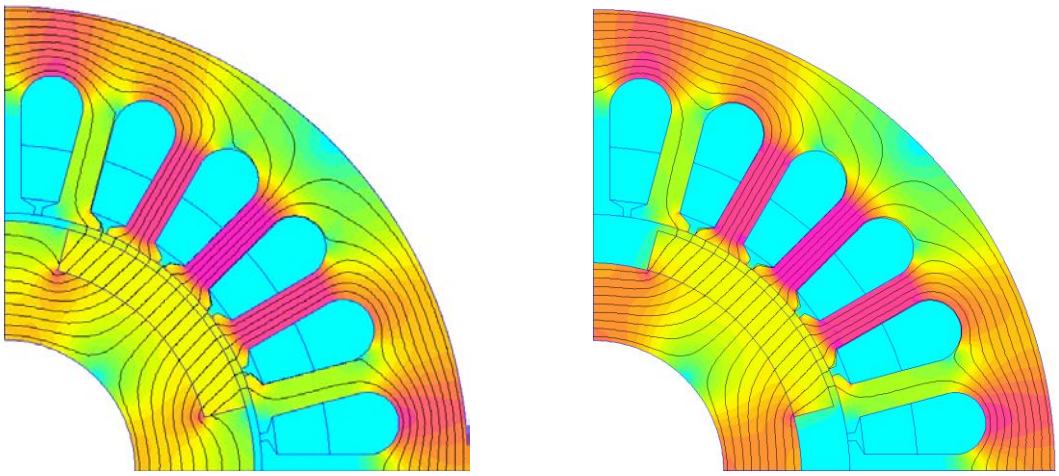

a) Inset magnet configuration b) Surface mount configuration

Fig. 5.4 PMSM rotor magnet configuration

The torque angle curves are obtained by fixing the rotor while the current vector of constant magnitude is rotated from 0 to 360 degree to cover the braking mode of operation. Figure 5.5 shows the torque angle curves displaying the benefits of the inset magnet motor. The torque can be as high as 10 – 15 % at the optimum angle (angle giving the maximum torque - 118 electrical degrees). Furthermore, the windage loss is reduced due to its cylindrical structure.

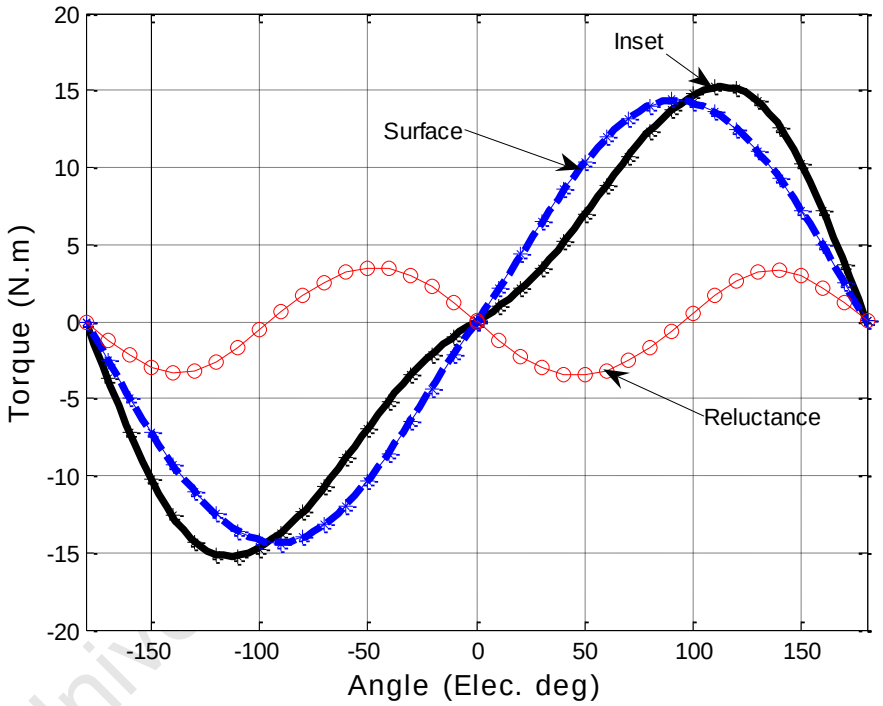

Fig. 5.5 Torque-Angle curves in forward and braking mode: FEMM (*) Flux (-)

The torque results in Figure 5.5 do not include rotor motion and therefore will not show any sign of torque ripple. Torque ripple analysis is discussed next.

5.3.4 Back EMF and Torque Design Results

Operating at the optimum angle and calculating torque under load resulted in a torque graph with significant ripples of about 33% referenced to the average torque as shown in Figure 5.6. The % ripple is calculated using the peak to peak torque ripple magnitudes. The ripple is visible at all speeds

along the torque speed envelope with rated current. The ripple peaks are a function of the number of slots.

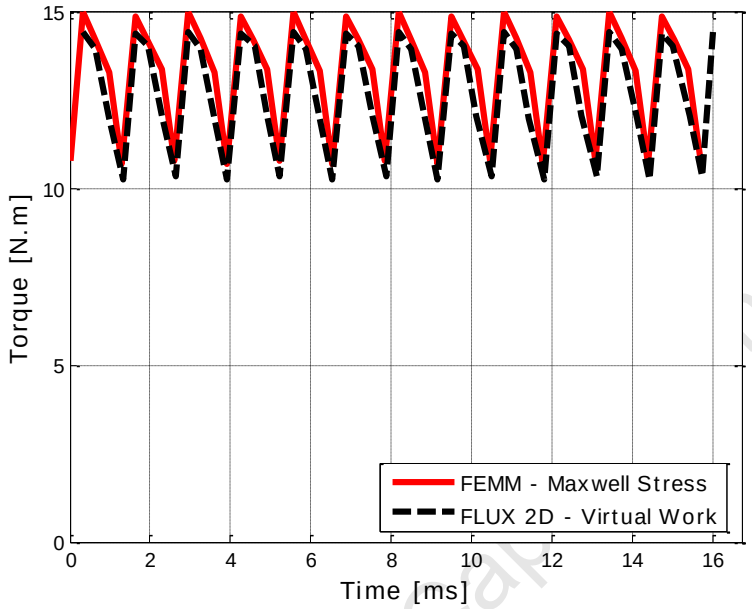

Fig. 5.6 Ripple Torque at 1912rpm using FEMM and Flux2D

The % torque ripple calculated using PCBDC in Figure 5.7 is about 15%. The difference is due to the methods used to calculate torque. FEMM uses the Maxwell Stress formula and Flux2D uses Virtual Work, these are in good agreement as indicated in Figure 5.6. The two methods require parameters such as flux density ***B***, Magnetic field ***H***, current density ***J*** and magnetic vector potential ***A***, all of which are available in FEA analysis. A detailed description of these methods is found in [34] [35]. PCBDC applies the analytical torque formula given by

$$T_e = T_{ei} + \frac{mp}{2} p \quad L_d - L_q \quad i_d i_q \tag{5.1}$$

Where T_{ei} is the average alignment torque calculated from the back EMF and current product divided by the angular speed [15]. The second term is the reluctance torque, where p is the pole pairs, L_d and L_q are d- and q-

axis synchronous inductance, respectively, i_d and i_q are d and q-axis current vector components in the rotor reference frame respectively. The torque components in (5.1) are calculated separately and summed up to get the total torque as shown in Figure 5.7.

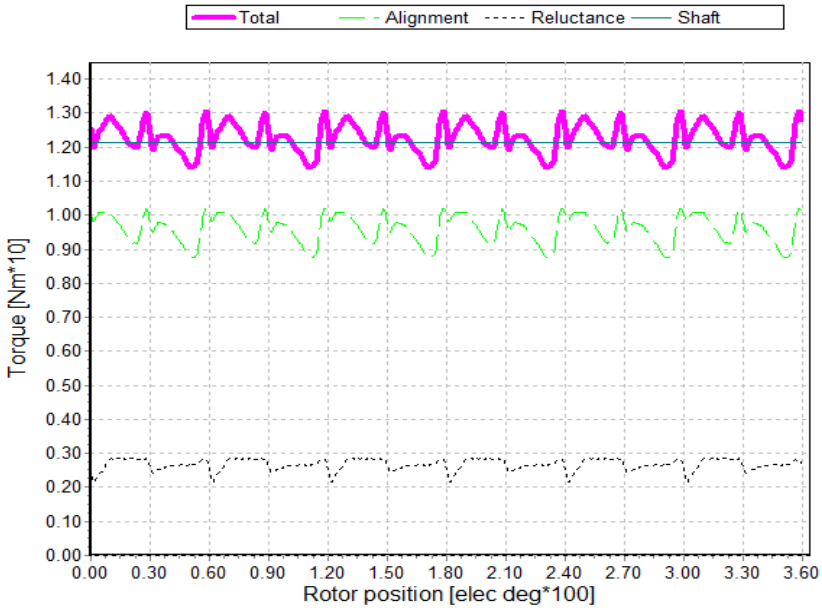

Fig. 5.7 Ripple Torque at 1912rpm using PCBDC

The torque ripple in both cases is caused by the non-sinusoidal EMF waveforms in Figures 5.8a and 5.8b, and amplified significantly by the large current magnitudes expected in this design.

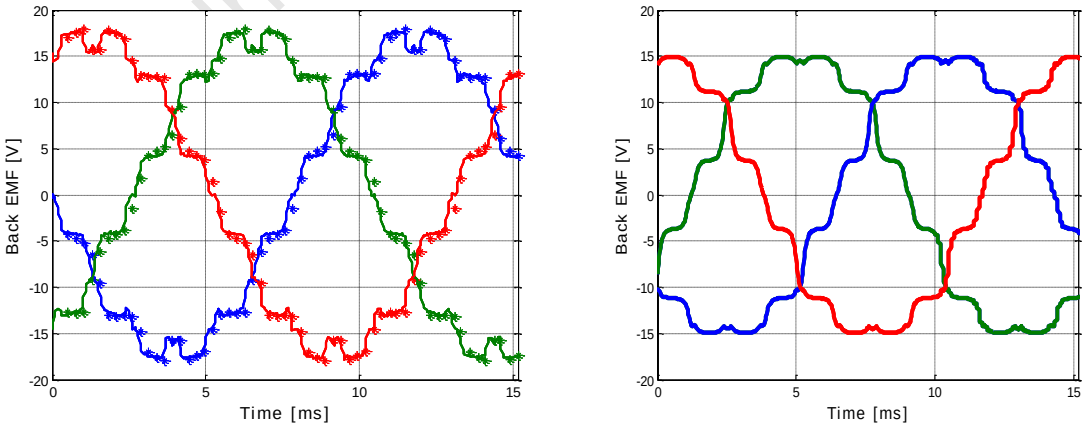

(a) FEMM (*) Flux2D (-) **(b)** PCBDC

Fig. 5.8 PMSM Back EMF at 1912rpm

The EMF waveshapes from PCBDC differ from the FEA at their peaks. It is difficult to produce an accurate EMF analytically when considering the complexity of the geometry (e.g. Slotting, saturation, field distribution, rotor position, etc.). The inductance is a function of rotor position and saturation, and its effects are included in the FEA simulations. The behavior of the EMF and inductance are difficult to quantify analytically during load conditions and this results in the difference in the ripple torque observed in Figures 5.6 and 5.7. However, the average torque values are similar.

The non-sinusoidal EMF waveforms in Figure 5.8 are improved by using parallel magnetized magnets, optimal magnet arc, short pitching or chording and ultimately skewing by one slot pitch. FEA is used to calculate the optimal magnet arc and slot opening for minimum cogging torque, while maintaining the rated torque. The effect of skewing and short pitching is shown in Figure 5.9. Short pitching by one slot or 30 electrical degrees reduces the 'belt harmonics', 5th and 7^{th}, while skewing removes higher harmonics; 13th, 15^{th}, etc. The third harmonic of very small magnitude (<2.8%) still exist. Short pitching by a further slot eliminates it completely but other harmonics become dominant and defeat the purpose. Also, a significant reduction in back EMF magnitude has been observed.

The back EMF is also affected by temperature as shown in Figure 5.10. This is due to the reduction of the temperature dependent remanent magnet flux density B_r and coercive force H_c. The EMF reduction from 25ºC to 155°C is 13% and increases further as the temperature rises. The magnets are sized not to demagnetize completely due to temperature and current while making it possible to start at low temperatures. The EMF is high at low temperatures and it can limit high speed operations due to the limited converter voltage.

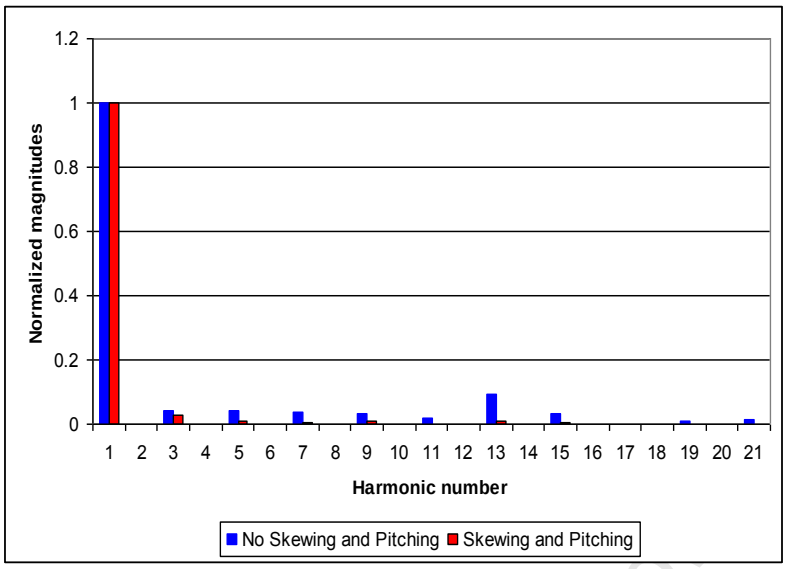

Fig. 5.9 Effect of skewing and short pitching by one slot

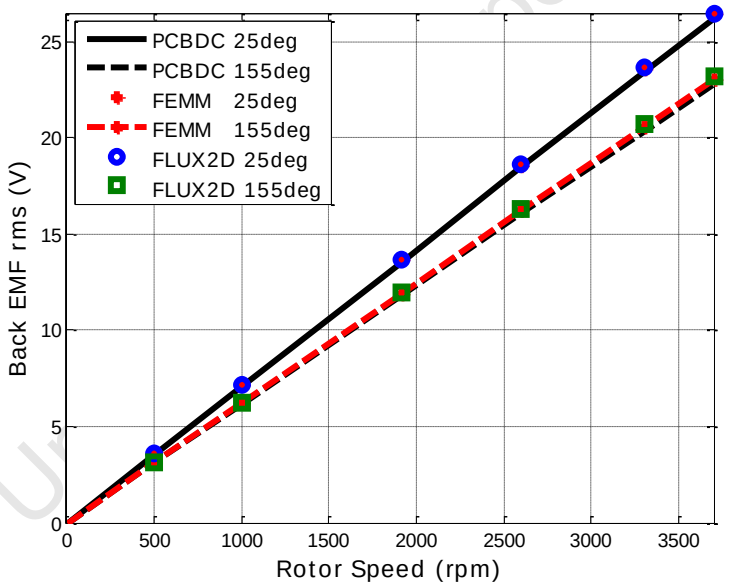

Fig. 5.10 Effect of temperature on back EMF rms

Skewing in two-dimensional FEMM is achieved by segmenting the geometry into different sections with the correct skew angle, analyzing them separately and summing the results. Figure 5.11 shows the phase back EMF obtained from four segments analysis. The waveform is close to sinusoidal. An

analytical expression can be deduced to calculate the EMF and Torque with any number of segments. Flux2D yields the same results and also has a built in 2D skewing capability using slices/segments. Figure 5.12 shows the skewed quasi-sinusoidal back EMF waveforms from the PCBDC software.

The torque waveform is recalculated with the quasi-sinusoidal back EMF achieved by pitching and skewing. The ripple is reduced from 33 % to less that 1% of the average torque as shown in Figure 5.13. Also, the cogging torque is reduced to 0.67% of the average torque.

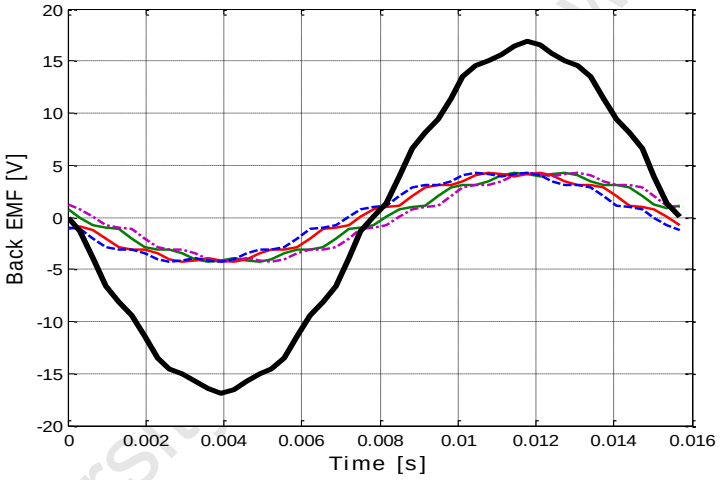

Fig. 5.11 Back EMF after skewing using FEMM

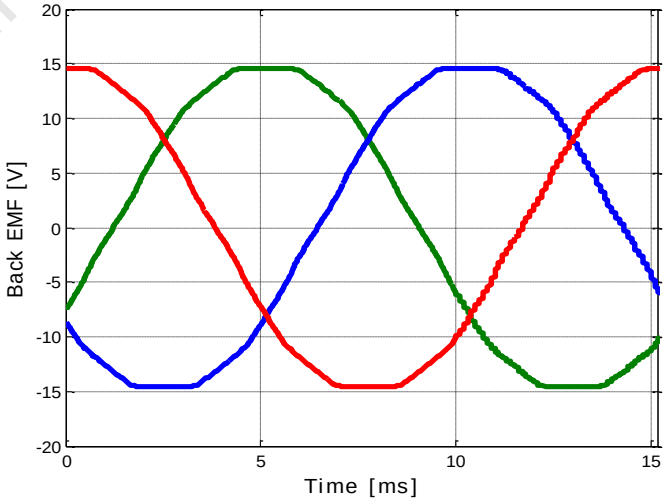

Fig. 5.12 Back EMF using PCBDC

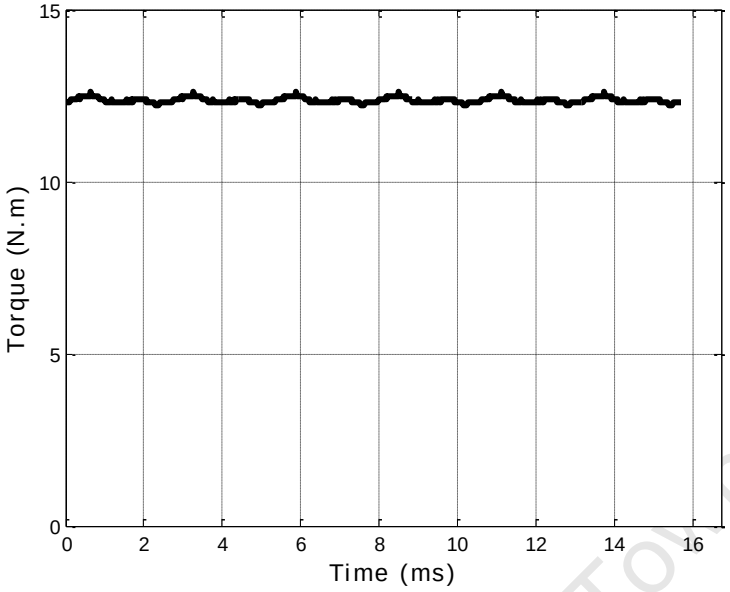

Fig. 5.13 Torque Ripple at 1912rpm: FE and PCBDC

5.4 MOTOR CORE LOSS CALCULATION

5.4.1 Core Loss Models in Machine Design Software's

Three core loss formulae have been used to calculate core losses during PMSM design process. Flux2D uses the Bertotti's formula with constant loss coefficients as indicated in (5.2) [27]. SPEED's PC-BDC software uses the modified Steinmetz model in (5.3) [15]. FEMM does not a have loss calculation model in its postprocessor and as a result, the new model given by (5.4) is tested using FEMM flux density waveform results.

$$\overline{P} = k_h {B_p}^2 f + \frac{\sigma d^2}{12}\frac{1}{T}\int\left(\frac{dB}{dt}\right)dt + \frac{k_{ex}}{\sqrt{2}\pi^{1.5}}\frac{1}{T}\int\left|\frac{dB}{dt}\right|^{1.5} dt \qquad (5.2)$$

$$\overline{P} = k_h {B_p}^{a+bB_p} f + \frac{k_e}{2\pi^2}\left[\frac{dB}{dt}\right]_{rms} \qquad (5.3)$$

$$\overline{P} = P_h(f, B_p) + \frac{k_{ex}(f)}{2\pi^2}\frac{1}{T}\int\left(\frac{dB}{dt}\right)^2 dt + \frac{k_{ex}(f, Bp)}{\sqrt{2}\pi^{1.5}}\frac{1}{T}\int\left|\frac{dB}{dt}\right|^{1.5} dt \qquad (5.4)$$

The PCBDC software is an analytical tool and does not produce flux density distributions in various sections on the motor as shown by density plots in Figure 5.4. Hence, only averaged alternating flux density curves are available. ***B*** is generally a rotating vector represented by two components, B_{rad} and B_{theta} (or B_y and B_x). Equations (5.2) – (5.4) show the scalar flux density, which could be any of the two components. To simplify loss calculations in finite elements (Flux2D), the loss component due to B_x and the loss component due to B_y are calculated separately and then summed to get the total core losses including the rotational effects. In the stator of the PM motor during no-load conditions, B_{rad} is dominant representing the stator tooth flux B as shown in Figure 5.14, and B_{theta} the yoke flux B as shown in Figure 5.15. Since only alternating flux density waveforms are available in PCBDC, the rotational losses are accounted for by extending the tooth area to include some parts of the yoke. This is the area where the flux ***B*** changes directions. A triangle, with the base at the tooth root and apex touching the stator outside diameter, is considered part of the tooth and losses are calculated inside the triangle without removing the added mass from the yoke loss calculations.

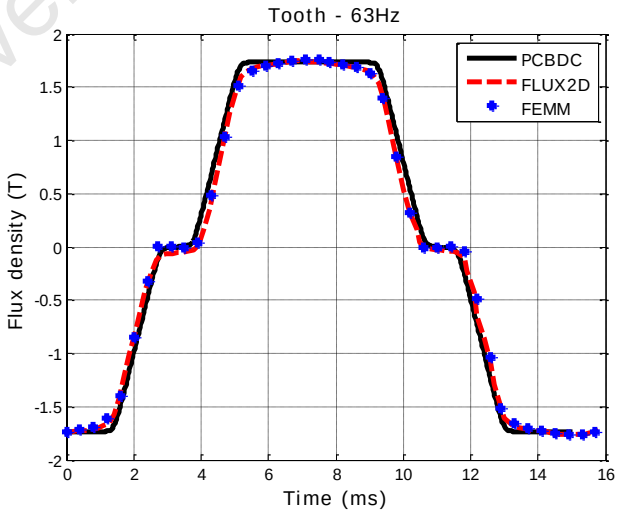

Fig. 5.14 Average no-load stator tooth flux density at 63Hz

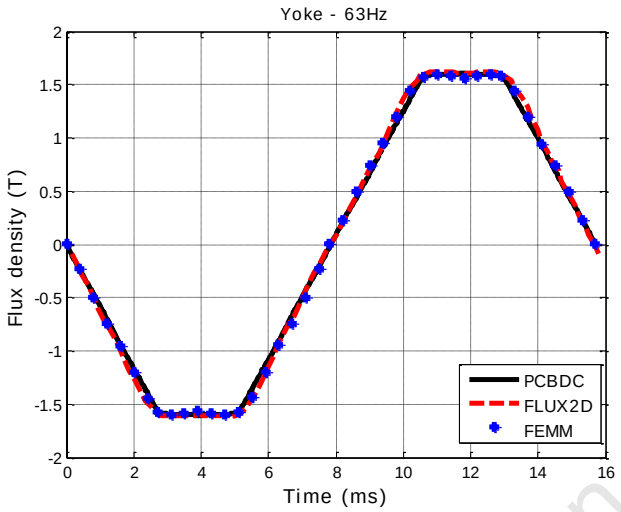

Fig. 5.15 Average no-load stator yoke flux density at 63Hz

5.4.2 Core Loss Calculation at no-load and under Load

Figure 5.16 shows the loss calculations at no-load. PCBD predicted higher losses than Flux2D. It can be deduced that the difference is due to the two methods applied to account for rotational magnetic losses, since the tooth and yoke alternating flux densities are the same from all softwares as shown in Figures 5.14 and 5.15. The new model loss results are obtained using FEMM which follows the same procedure applied in Flux2D. The loss prediction is higher than Flux2D.

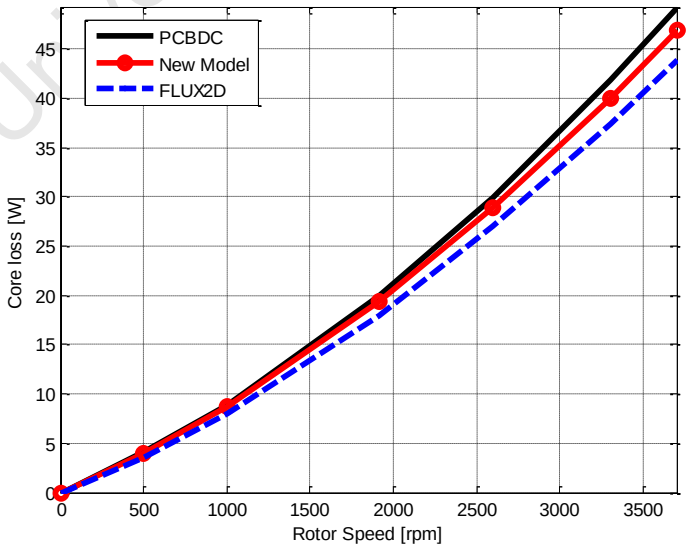

Fig. 5.16 Core loss predicted results at no-load

Core loss calculation under loaded conditions is very important since it has direct impact on the motor performance such a temperature rise, torque and efficiency. Figure 5.17 shows the core loss predicted results using Flux2D, PCBDC and FEMM (new model) under loaded conditions at various speeds. There is a significant difference between the FEA results and PCBDC results as speed increases. The PCBDC software is an analytical tool which cannot calculate the tooth and yoke flux density waveforms accurately under load, especially for salient pole machines. The reaction between the armature and magnet excitations is very difficult to quantify analytically in order to produce the correct flux density waveforms for Inset Mount machines. Figure 5.18 and 5.19 show good correlation of the yoke and tooth flux densities using Flux2D and FEMM. The shapes and the magnitudes of the waveforms are the cause of higher losses while the PCBDC assumes lower flux densities waveforms with incorrect shapes. The waveform shapes are vital for the eddy current loss component calculations. The new model predicts higher losses than Bertotti's formula.

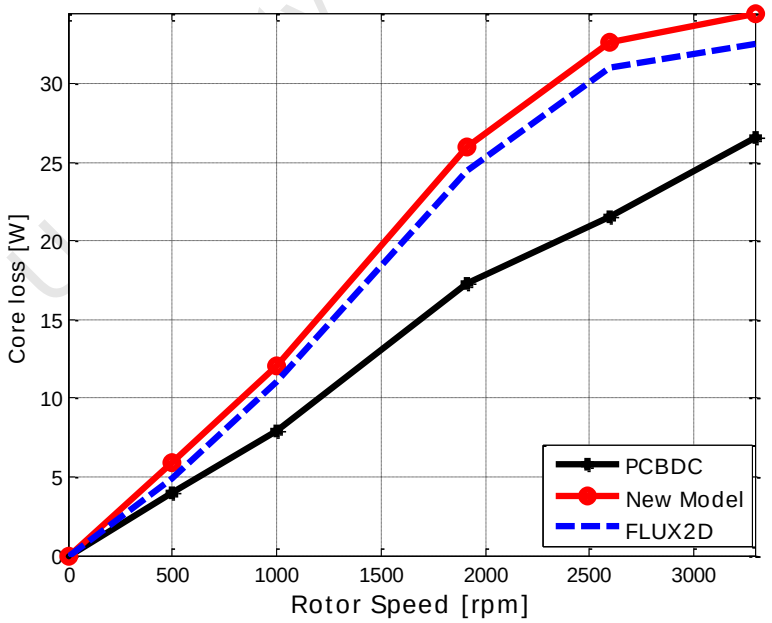

Fig. 5.17 Core loss predicted results under load

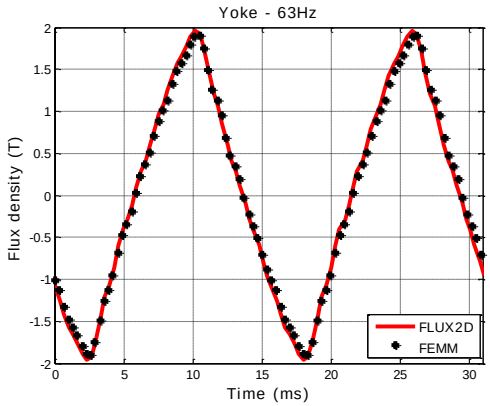

Fig. 5.18 Stator yoke flux density

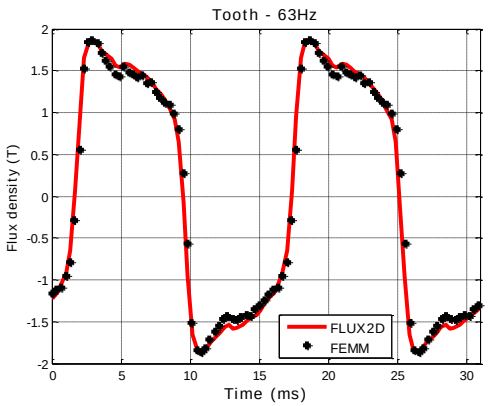

Fig. 5.19 Stator tooth flux density

Designing a motor using PCBDC core loss results will surely produce a higher efficiency and cooler machine than Flux2D or FEMM (new model) in paper, assuming Flux2D results as reference. In practice, it is better to over predict than under predict losses and efficiency. The core losses are also affected by temperature and skewing.

5.4.3 Effect of Skewing and Temperature on Core Losses

Skewing alters the flux density waveforms towards the desired sinusoidal shape, thereby, reducing the dynamic or rate dependant losses (eddy and excess losses). The increase in temperature reduces core losses due to the increase in lamination resistance and reduction in magnet flux density. Figure 5.20 shows the calculated no-load core loss results obtained at 25°C and 155°C, before and after skewing, from 0 - 3300rpm. The average loss drop due to temperature is 17% and 6% due to skewing. Core loss reduction due temperature has also been reported in literature based on the measurement perform on the Epstein Test bench discussed in Chapter 2.

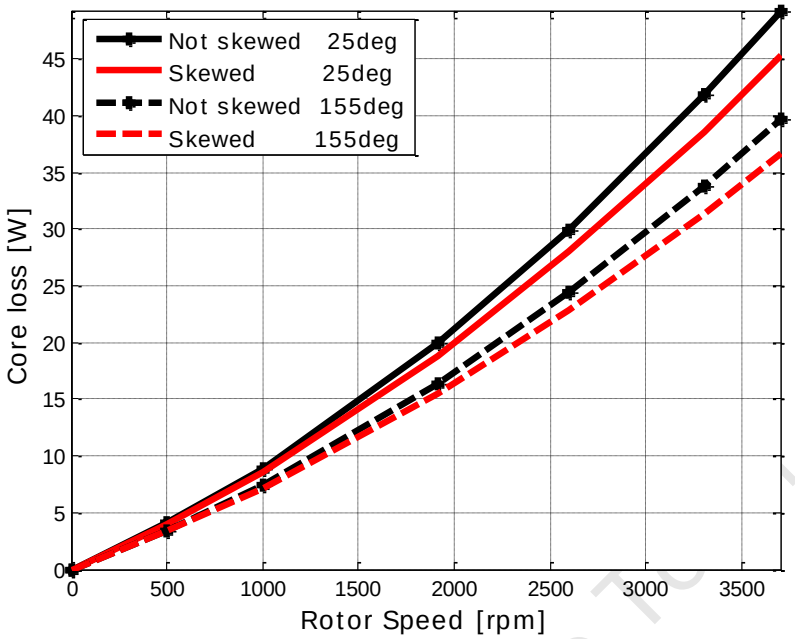

Fig. 5.20 Effect of skewing and temperature on core loss

5.5 MOTOR PROTOTYPING

5.5.1 Motor Assembly

Figure 5.21 shows the traction motor in different stages of assembly. The magnets are segmented which reduces the magnet eddy current losses due to slot harmonics. Search coils are inserted together with the winding. Thermocouples are glued to the end winding and core to determine motor temperature.

Fig. 5.21 PMSM Motor prototyping

5.5.2 Back EMF Measured Results

The motor was mounted on a test bed which consists of an inline torque transducer and a 5.5 kW dynamometer as shown in Figure 5.22. The back EMF was measured from 0 – 3300rpm and the desired sinusoidal waveforms were observed from the scope as shown in Figure 5.23. The EMF waveform spectrum in Figure 5.24 shows the comparison between

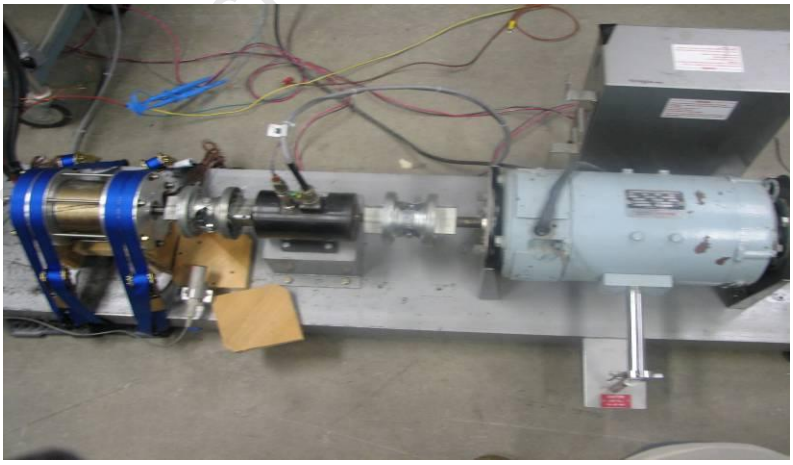

Fig. 5.22 Motor test bed

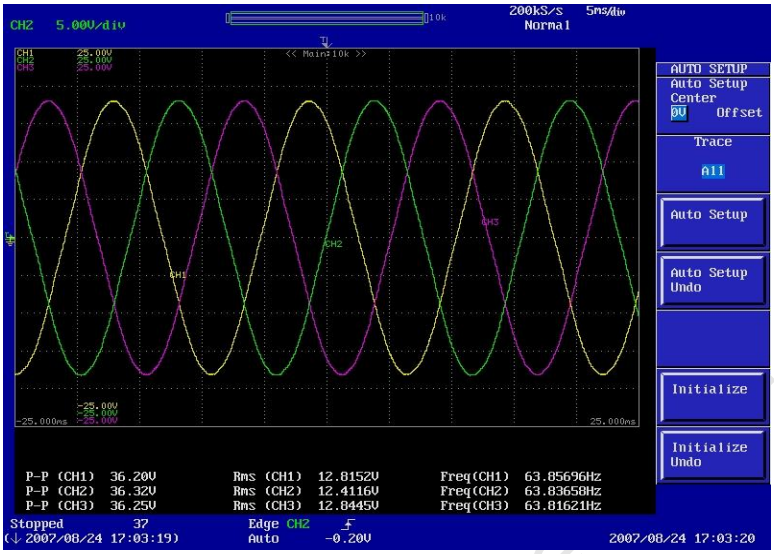

(a) 1912 rpm- Base speed

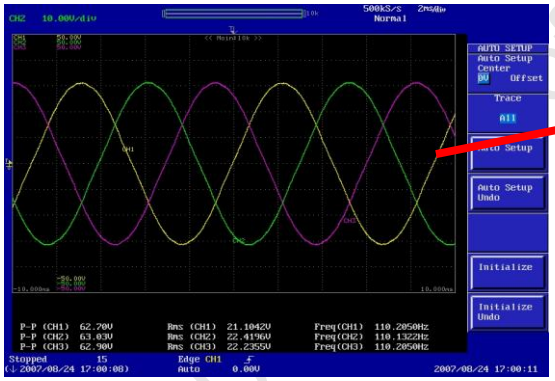

(b) 3300 rpm- Maximum speed

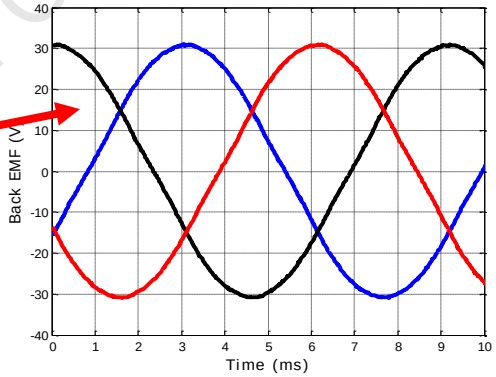

(c) Enlargement of graph (b)

Fig. 5.23 PMSM Back EMF captured in scope

the simulated and measured back EMF. The measured back EMF has insignificant third harmonic component compared to the simulation.

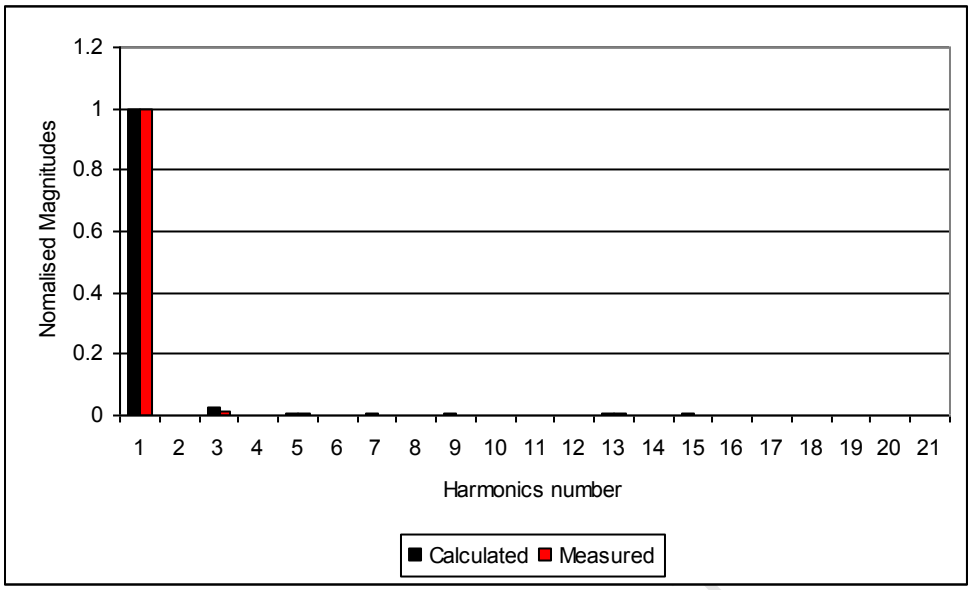

Fig. 5.24 Measured and calculated back EMF Spectrum at no-load

Figure 5.25 shows the comparison between the measured and the calculated back EMF *rms* values. There is a slight deviation (<6%) at high speeds. This is attribute to the fact that there is magnet flux reduction during measurement due to increase in temperature caused by rotational losses (core loss and windage and friction). The calculated EMF is done at constant temperature of 25°C.

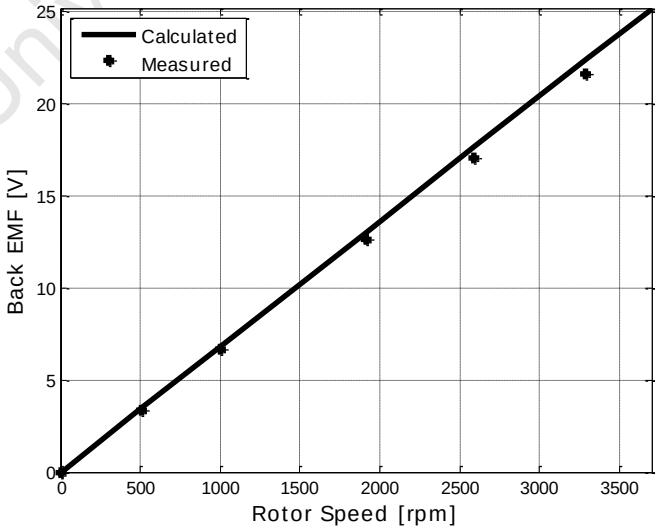

Fig. 5.25 Measured and calculated back EMF rms values at no-load

5.5.3 Core Loss Measurement Results

The motor rotational losses (core loss and windage and friction) are measured at no-load. An identical motor is built without rotor magnets in order to quantify the windage and friction losses. The measured mechanical losses (windage and friction losses) are then subtracted from the rotational losses to get the core losses.

In part of the core loss measurements, the tooth and yoke search coils EMFs are also captured. Figure 5.26 shows the locations of the search coils. The captured waveforms are shown in Figure 5.27 at 1912 rpm no-load speed. The measured and simulated EMF waveforms obtained from PCBDC, FEMM and Flux2D softwares have similar shapes and magnitudes (<1% error). The EMF waveforms in Figure 5.27 are used to calculate core losses instead of using the flux density waveforms ($e = NAdB/dt$). The core loss results are shown in Figure 5.28 using the new model. Also, the search coil voltage waveforms allow core loss estimation at any load conditions.

The measured and predicted core loss results are shown in Figure 5.28. There is a significant difference (47% - 53.6%) between the measured and predicted losses using the new model. The difference is attributed to the manufacturing techniques used. The stator laminations were welded together in order to form a core. Initially, only three welds at 120° apart were approved in order to limit the eddy current paths. During the hand winding process, the laminations were becoming loose and three more welds were added uniformly. The welds increased the eddy current paths, which in turn increase the total measured losses. Moreover, the laminations were not annealed to relief stress after cutting. The loss calculation formulae do not account for the manufacturing effects since they are not generic and therefore difficult to quantify accurately. A scaling factor approach based on experimental results can be implemented to improve the loss calculation formula. This work is included in the recommendation section.

The simulation showed insignificant rotor core and magnet loss since the slot harmonics are very small in this design. The loss predicted using search coil EMFs are also shown in Figure 5.28. They all predict slightly lower that FEMM (New Model) because they do not account for all flux density components.

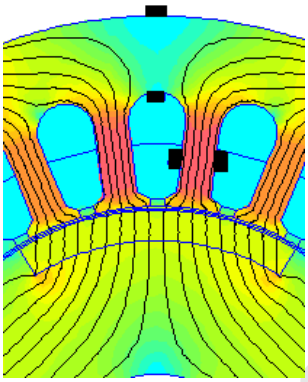

Fig. 5.26 Stator yoke and tooth search coils positions

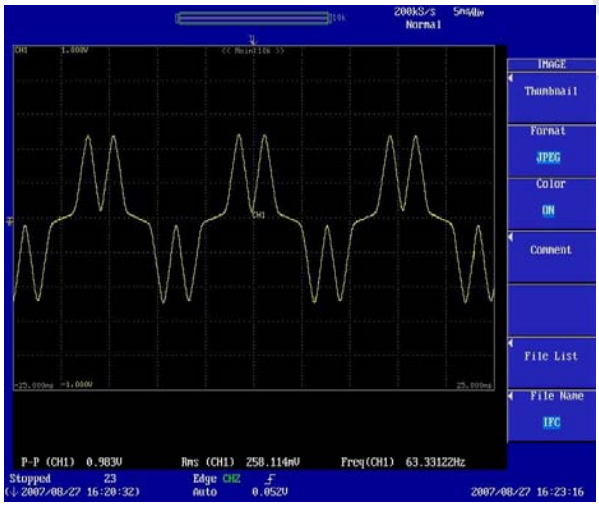

(a) Measured Tooth EMF

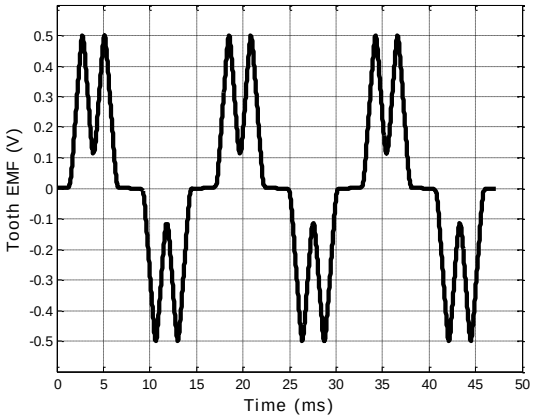

(b) Simulated Tooth EMF

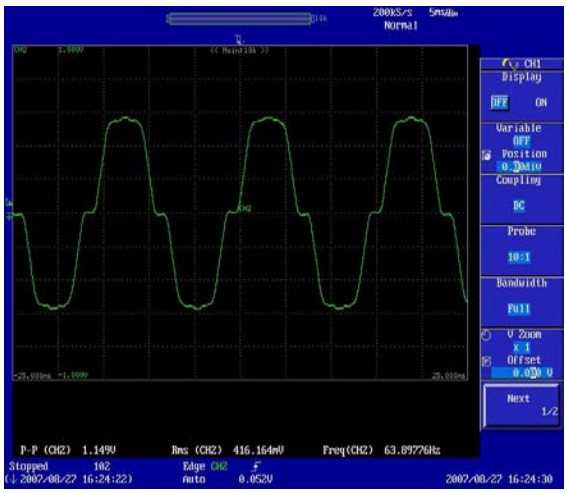

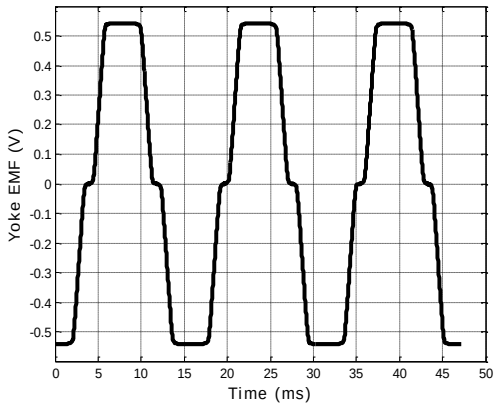

(c) Measured Yoke EMF **(d) Simulated Yoke EMF**

Fig. 5.27 Measured and simulated search coil EMFs

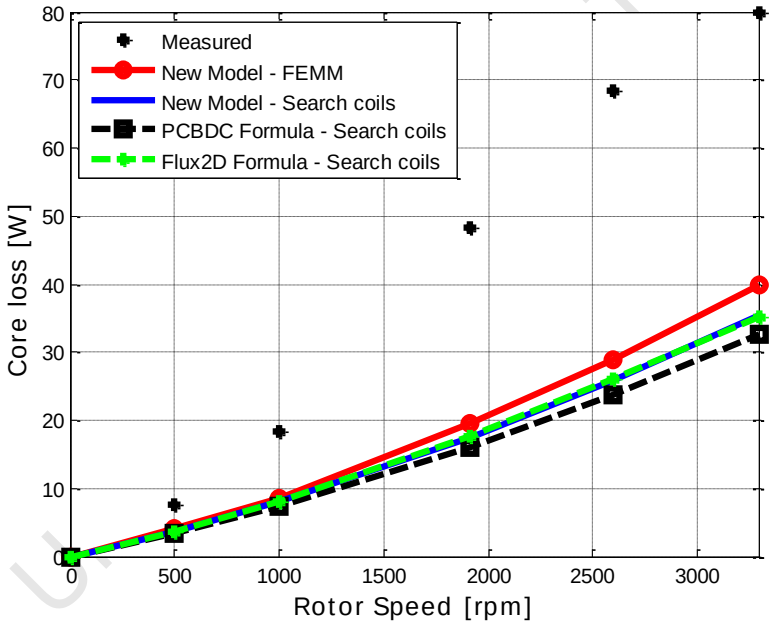

Fig. 5.28 PMSM measured and calculated core loss results at no-load

5.5.4 Torque results

Figure 5.29 shows 1% - 5% difference between the measured and predicted (solid line) average torque results. The motor meets the required torque-speed points (dots). Further performance tests are to be done in order to qualify the motor to the intended application.

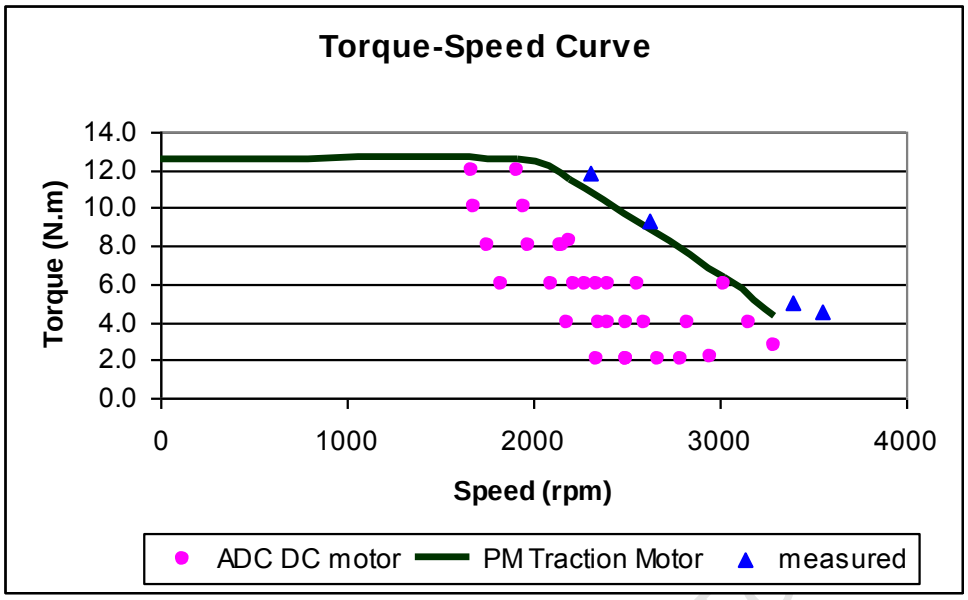

Fig. 5.29 PMSM measured and calculated torque results

5.6 INTEGRATION OF NEW MODEL INTO FLUX2D SOFTWARE

The improved model has shown good correlation with measurements from test frames and electrical motors in Chapter 3 and Chapter 4. The model has been tested with both sinusoidal and non-sinusoidal flux density waveforms in Chapter 3 and found to be better that Bertotti's formula currently used in Flux2d and 3D. Before integration of the new formula is presented, the Flux 2D procedure for loss calculation is reviewed.

5.6.1 Loss Calculation in Flux2D FE Software

The core loss calculation in Flux2D is done in the post-processing stage of the design simulation using the formula in (5.5). The formula has been copied directly from the Flux2D manual [27].

$$\frac{1}{T}\int_0^T dP_{TOT}(t)dt = k_h {B_m}^2 f k_f + \frac{1}{T}\int\left[\sigma\frac{d^2}{12}\left(\frac{dB}{dt}(t)\right)^2 + k_e\left(\frac{dB}{dt}(t)\right)^{3/2}\right]k_f\,dt \qquad (5.5)$$

Where k_f is the stacking factor, B_m is the peak flux density, k_h and k_e are hysteresis and excess loss coefficients. f is the frequency of the flux density waveform B and T is the period. d is the lamination thickness and σ is the material conductivity. The instantaneous loss dP_{TOT} in watts per unit volume is defined in the manual as

$$dP_{TOT} = k_h B_m{}^2 f + \pi^2 \frac{\sigma d^2}{6} \left(B_m \cdot f \right)^2 + k_e \left(B_m \cdot f \right)^{3/2} \times 8.67 \qquad (5.6)$$

Equation (5.6) is represented incorrectly as instantaneous loss. It is actually the average loss over one electrical cycle. This equation is used when calculating loss coefficients k_h and k_e provided material properties d and σ are known. Only two loss data are required from the steel manufacturer. The coefficient calculation is done by the user outside the program.

There is a graphic user interface (GUI) that is used to enter core loss coefficients and other material properties before loss estimation. Figure 5.30 show the GUI with default values. Once all the parameters are entered, core losses can be estimated in different parts of the motor geometry where there is relative rate of change of flux density (e.g. stator, rotor, etc).

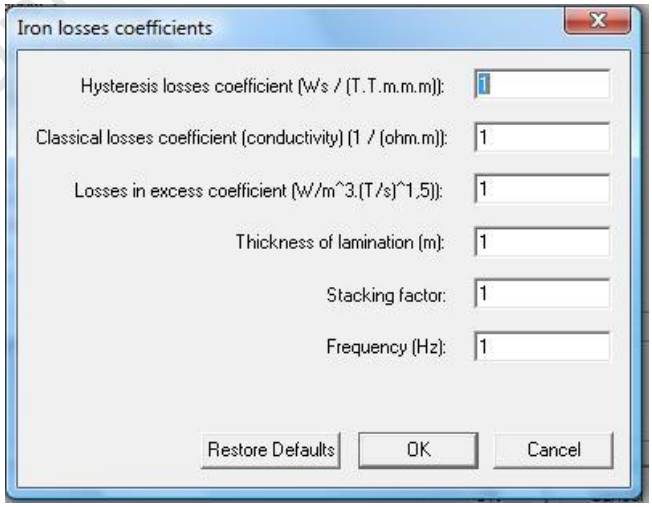

Fig. 5.30 FLUX 2D Loss coefficient GUI

Suppose the stator core loss is of interest, the flux density waveform components are available at each point on the stator core from the post processor as shown in Figure 5.31. This includes the flux density magnitude, B_x and B_y components since flux density is a vector. The loss is calculated for each component to include the rotating vectors and then added up to give the total losses.

Figure 5.32 shows the core loss output graph over one electrical cycle calculated in 'transient magnetic mode with rotor motion' but in steady state conditions. The correct value of losses is given by the average value over one period as indicated in (5.5). The exact average value is calculated using Flux2D mathematical tools.

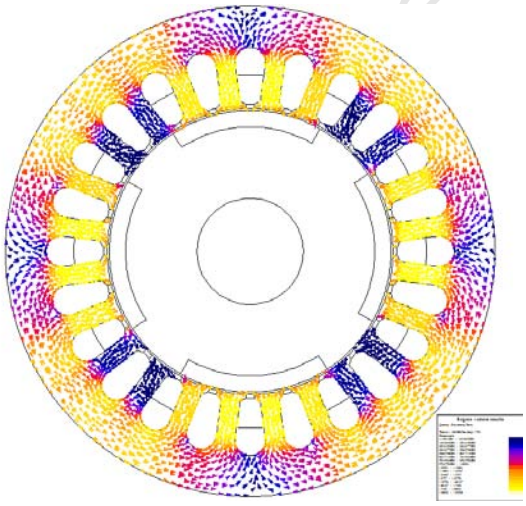

Fig. 5.31 PMSM stator flux density vectors: Yellow Max, Blue min

5.6.2 Integration of New Formula into Flux 2D FE Software.

The new formula in (5.7) has variable loss coefficients and therefore requires loss data vs. flux density at four or more different frequencies in order to calculate the coefficients.

$$P = P_h(f, B_p) + k_e(f) f^2 B_p^2 + k_{ex}(f, B_p) f^{1.5} B^{1.5} \qquad (5.7)$$

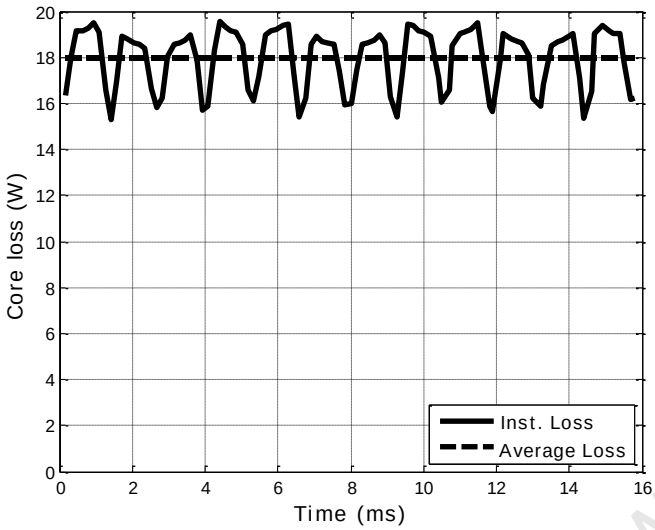

Fig. 5.32 Loss calculation result from Flux 2D at no-load

The loss data requirement is significantly higher than that required in the current Flux2D formula. The availability of the data is not a problem since the EMERF group is developing a material core loss database at low and high frequencies.

A program is developed in MATLAB and Excel to calculate the coefficients and is summarized as follows:

Enter measured core loss data:
Loss vs. flux density at various frequencies or loss vs. frequency at various densities.

Hysteresis loss coefficient:
Plot Loss/frequency vs. frequency at various flux densities and extrapolate the curves to zero frequency. Plot loss vs. flux density and fit a curve to obtain hysteresis loss per cycle.

Eddy current loss coefficient:
Check the skin effect and use the correct equation to calculate the eddy current coefficient k_e

Excess loss coefficient:

Plot k_{ex}, obtained from loss separation vs. frequency at various flux densities and fit a curve to obtain c and d coefficients. The c and d coefficients are

then plotted vs. flux density and fitted to get a general for k_{ex} as a function of flux density and frequency.

The calculated loss coefficients can then be used in the Flux2D program with the new formula in (5.4) to obtain the average loss over one electrical cycle.

5.7 CONCLUSIONS

- The Low Voltage High Current traction motor is designed using three software packages for comparison and validations. Skewing and short pitching techniques are analyzed and implemented to reduce the large torque ripple due to non-sinusoidal EMF and current amplification. The core losses and back EMF are affected by skewing and temperature. The torque calculation methods have an impact on the torque ripple magnitudes.

- PCBDC software core loss model under estimates core losses during load conditions in salient pole machines due to inaccuracies in flux density calculations.

- The measured losses are higher that calculated losses due to the welds imposed on the stator core. The manufacturing of the laminations and core assembly techniques affect the core loss results and there are no generic scaling factors.

- The procedure to integrate the new formula into Flux2D is highlighted.

Chapter 6

6. CONCLUSIONS AND RECOMMENDATIONS

6.1 CONCLUSIONS

Based on the findings presented in this report, the following conclusions are drawn:

On Core Loss Measurements

- The two core loss measurement formulae yield similar results for different testing frames and materials at various frequencies. The core loss results from the developed laboratory test bench shows good correlation with the new commercial Donart test equipment. The repeatability of the two test equipment is acceptable.

- The new 200-turn non-traditional Epstein frame measures losses at high frequencies and high flux densities with acceptable accuracy, surpassing the 352-turn and 280-turn frames capabilities. The 280-turn EMERF Epstein frame results are extended from 1kHz to 6kHz and achieved higher flux density than the standard 352-turn frame.

- The Single Sheet Tester core loss results are averaged for comparison with Epstein results. The SST is calibrated by the Epstein results. The core loss results measured from small unannealed toroidal fixture are higher than Epstein, a representation of the practical situation in motor design. Better correlation with standard Epstein is observed with the large toroid.

- Core loss measurements are affected by frame and sample configuration, preparation, arrangement, annealing and correction

factors. The user has to be aware of these effects in order to make a proper choice before designing and adjustment during the design process.

On Core Loss Modeling

- The Steinmetz and classical formulae predict the same core losses at various frequencies and materials provided the loss coefficients are recalculated at frequency of concern. The skin effect must be accounted for when using classical formula at high frequencies. Limited loss data affect loss prediction at higher frequencies, resulting in a significant deviation from measurements, especially for the classical formula. The Steinmetz constant, n =1.6, is not generically applicable to all materials. The modified Steinmetz model does not necessary predict better results that the original Steinmetz's formula, especially at high flux densities.

- Berttoti's formula shows improvement when compared to the classical model with physical basis, especially when estimation is done with limited loss data. However, Bertotti's formula still under estimates losses at high flux densities. Also, the formula is invalid at high frequencies.

- Core loss prediction at frequencies not used during loss coefficient calculations is not recommended for conventional core loss models

- The proposed model performs better than the modified Steinmetz used in SPEED PCBDC Software and Bertotti's model used in Cedrat/Magsoft Flux 2D/3D. The model shows good correlation with measured results under both sinusoidal and non-sinusoidal excitations.

On Application of New Core Loss Formula

- A promising tool to predict core losses is tested in electric machines. The model is applicable to both sinusoidal and non-sinusoidal cases. Furthermore, the model has a physical basis for the variation of the loss coefficients and good alignment with experimental data from the induction motor and toroid frame. The new model error range is 1.1% - 7.6% while the FEM (Bertotti) % error is between -8.5% - +44.7%.

- The modified Steinmetz model under estimates losses (0 - 35% error) at all tested frequencies.

- An alternative method is also presented which requires direct loss measurement from test frame; Toroid or Epstein. This method predicts the loss accurately although it requires the availability of advanced testing equipment and laminations.

- The motor heating is affected by the accuracy of core loss measurement data and calculation formulae

On PM Machine Design and Integration of New Formula into Flux2D

- The Low Voltage High Current traction motor is designed using three software packages for comparison and validations. The torque calculation methods have an impact on the torque ripple magnitudes. The core losses and back EMF are affected by skewing and temperature.

- PCBDC software core loss model under estimates core losses during load conditions in salient pole machines due to inaccuracies in flux density calculations.

The measured core losses are higher that calculated losses due to the welds imposed on the stator core. The manufacturing of the laminations and core assembly techniques affect the core loss results and there are no generic scaling factors.

- The procedure to integrate the new formula into Flux2D Software is highlighted.

6.2 SUMMARY OF THE THESIS

Chapter 2 describes the core loss measurement concept and compares test frames and new test equipment. The effect of frame and sample configuration on core loss measurements is presented. A full description and comparison of old and recent core loss models using measurements from chapter 2 is presented in Chapter 3. Development and testing of new core loss formula using resent core loss results at low and high frequencies, sinusoidal and non-sinusoidal excitations is presented in Chapter 3. Chapter 4 examines the applicability and accuracy of the improved model in induction machines and PM synchronous machines. An alternative method of core loss prediction in machine design without using the core loss formulae is developed using core loss measurements described in Chapter 2. The PM synchronous machine design using different softwares and integration of new formula into MAGSOFT Flux2D is presented in Chapter 5. Emphasis is made on core loss calculations using models described in Chapter 3.

6.3 RECOMMENDATIONS

- There is a need to continue with characterization of materials at high frequency and high flux densities. This will support novel designs operating at these specifications.

- The new core loss model has been tested on the induction motor and the permanent magnet synchronous motor operating with non-

sinusoidal flux density waveforms. Switched reluctance machines also have non-sinusoidal waveforms in the laminations. Further testing is recommended for switched reluctance machines.

- The choice of peak permeability when calculating skin effect. This is subjected to debate since μ varies with flux density.

- The loss calculation formulae do not account for the manufacturing effects since they are not generic and therefore difficult to quantify accurately. One of the assembling techniques is welding. The position and number of welds have an impact on core losses. A scaling factor approach based on experience and test results from several machines can be use to improve the loss calculation formula. The predicted results are also affected by the test frames used and cutting stresses. Further study on the effects of laminations manufacturing and assembling procedures on core loss formula is recommended.

6.4 CONTRIBUTIONS

International conference papers:

[1] M.J. Manyage, P. Pillay, "Low Voltage High Current PM Traction Motor Design Using Recent Core Loss Results", 42nd IAS Annual Meeting, New Orleans, USA, Sep 23-27, 2007.

[2] M. J. Manyage, T.L. Mthombeni, P. Pillay, A. Boglietti. "Improved Prediction of Core Losses in Induction Motors", IEEE IEMDC 2007, Antalya, Turkey, May 3-5, 2007.

[3] M.J. Manyage, P. Pillay, " New Epstein Frame for Core Loss Measurements at High Frequencies and High Flux Densities", Submitted to the 43rd IAS Annual Meeting in Canada, 2008.

REFERENCES

[1] C. P. Steinmetz, "On the law of hyesteresis: Part i," *Trans. Ame. Inst. Elect. Engrs.*, vol. 9, pp. 3 – 51, 1892.

[2] G. Bertotti, "Hysteresis in Magnetism," *Academic Press, Inc*. 1998

[3] G. McPherson and R.D. Laramore," Introduction to Electrical machine and Transformers" 2nd ed. John Wiley & Sons, 1990. pp20-24.

[4] Annual Book of ASTM Standards, "Section 3: Metal test methods and analytical procedures", Volume 03.04, 2006.

[5] S.L. Burgwin," Measurement of core loss and ac permeability with 25cm epstein frame," ASTM 44th Annual Meeting Chicago, Ill,, June 23-27,1941

[6] T. L. Mthombeni, P. Pillay, R. M. W. Strnat, "New Epstein Frame for Lamination Core Loss Measurements Under High Frequencies and High Flux Densities", IEEE Transactions on Energy Conversion, Vol. 22, Issue 3, Sept. 2007, pp. 614 – 620.

[7] T.L. Mthombeni, "Improved lamination core loss measurement and calculations," *PhD. Thesis*, Clarkson university, NY, US, April 2006.

[8] T. L. Mthombeni and P. Pillay, "Core losses in motor laminations exposed to high frequency or non-sinusoidal excitation," *IEEE Trans. on Indus. Applications*, vol. 40, no.5, pp. 1325–1332, Sept/ Oct 2004.

[9] C. D. Graham, "Physical origin of losses in conducting ferromagnetic materials," *Journal of Applied Physics*, vol. 53, no. 11, pp. 8276–8280, November 1982.

[10] G. Bertotti, "General properties of power losses in soft ferromagnetic materials," *IEEE Trans. Magnetics*, vol. 24, no. 1, pp. 621–630, January 1988.

[11] D. M Ionel, M. Popescu, S. J. Dellinger, T.J.E. Miller, R.J. Heideman and M.I McGilp, "On variation with flux and frequency of the core loss Coefficients in electrical machines," *IEEE Trans. on Indus. Applications*, vol. 42, no. 3, May/June 2006, pp. 658-667.

[12] D. M Ionel, M. Popescu, S. J. Dellinger, R.J. Heideman and M.I McGilp, "Computation of core losses in electrical machines using improved models

for laminated steel," *IEEE 41st IAS Annual Meeting*, 8-12 Oct 2006.

[13] H. Domeki, Y. Ishihara, C. Kaido, Y. Kawase, S. Kitamura, T. Shimo-mura, T. Yamanda, N. Takahashi, and K. Yamazaki, "Investigation of benchmark model for estimating iron loass in rotating machine," *IEEE Trans. on Magnetics*, vol. 40, no. 2, March 2004.

[14] Y. Chen and P. Pillay, "An improved formula for lamination core loss calculations in machines operating with high frequency and high flux density excitation," *IEEE 37th IAS Annual Meeting*, vol. 2, pp. 759–766, 13-18 Oct. 2002.

[15] T. J. E. Miller and M. I. McGilp, PC-BDC 6.5 *for windows-software*. Glasgow, UK.: SPEED Laboratory, Uni. Glasgow, 2004.

[16] G. Bertotti, "Physical interpretation of eddy current losses in ferromagnetic materials. I. Theoretical considerations," *Journal of Applied Physics, vol. 57, no. 9, pp. 2110-2117, 15 March 1985.*

[17] G. Bertotti, "Space-time correlation properties of the magnetization process and eddy current losses: Theory," *Journal of Applied Physics, vol. 54, no. 9, pp. 5293-5304, September 1983.*

[18] F. Deng, "An improved iron loss estimation for permanent magnet brushless machines," *IEEE Transactions on Energy Conversions*, vol. 14, no. 4, pp. 1391 – 1395, December 1999.

[19] K.J. Tseng and S.B. Wee "Analysis of flux distribution and core loss in interior Permanent Magnet Motor," *IEEE Transactions on Energy Conversions*, vol. 14, no. 4, pp. 969 – 975, December 1999.

[20] A. Boglietti, A. Cavagnino, M. Lazzari, and M. Pastorelli, "Predicting iron losses in soft magnetic materials with arbitrary voltage supply: An engineering aproach," *IEEE Transactions on Magnetics*,, vol. 39, no. 2, March 2003.

[21] G. R. Slemon and X. Liu, "Core losses in permanent magnet motors," *IEEE Transactions on Magnetics*, vol. 26, no. 5, pp. 1653 – 1655, September 1990.

[22] T.L.Mthombeni and P.Pillay, "Physical Basis for the Variation of Lamination Core Loss Coefficients as a Function of Frequency and Flux Density." IECON, France, 2006.

[23] M.J. Manyage, P. Pillay, "Low Voltage High Current PM Traction Motor Design Using Recent Core Loss Results", 42nd IAS Annual Meeting, New Orleans, USA, Sep 23-27, 2007.

[24] M. J. Manyage, T.L. Mthombeni, P. Pillay, A. Boglietti. "Improved Prediction of Core Losses in Induction Motors", IEEE IEMDC 2007, Antalya, Turkey, May 3-5, 2007.

[25] T. L. Mthombeni, P. Pillay, and A. S. Naidu, "Lamination core loss measurements in machines operating with pwm or non-sinusoidal excitation," *IEEE International Electric Machines and Drives Conference*, vol. 2, pp. 742 – 746, 1-4 June 2003.

[26] A. Boglietti, A. Cavagnino, T. L. Mthombeni and P. Pillay, "Comparison of lamination iron losses supplied with pwm voltages: Us and european experiences," *IEEE IEDMC*, 2005.

[27] Flux 2D V9.3.2, Magsoft Corporation, http://www.magsoft-flux.com/.

[28] Maxwell 2D V11, Ansoft Corporation, http://www.ansoft.com/

[29] A. Boglietti, A. Ferrraris and M. Lazzari, "Induction motor iron losses measurement with a static converter supply using a slotless rotor test bench," *IEEE Transactions on Magnetics*, Vol. 30, No. 6, pp 4599-4601, November 1994.

[30] C.A. Hernandez-Aramburo, T.C. Green and A.C. Smith. "Estimating rotational iron losses in an Induction Machine," *IEEE Transactions on Magnetics*, Vol. 39, No. 6, pp 3527-3533, November 2003.

[31] G. Bertotti, A. Boglietti, M. Chiampi, D. Chairabaglio, F. Fiorillo and M. Lazzari, "An improved estimation of iron losses in rotating electrical machines," *IEEE Transactions on Magnetics*, Vol. 27, No. 6, pp 5007-5009, November 1991.

[32] FEMM V4.0, D. Meeker, "Finite Element Method Magnetics", http://femm.foster-miller.net

[33] Magnet2D V6.25, Infolytica Corporation, http://www.infolytica.com

[34] S.J. Salon," Finite element analysis of electrical machines" Kluwer Academic Publishers, 1995. pp 98-110.

[35] N. Bianchi," Electrical machines analysis using finite element" Taylor and Francis Group, 2005. pp 69-70.

[36] P. Mlambo-Ngcuka," Energy efficiency strategy of the republic of South Africa," Department of Minerals and Energy, Republic of South Africa, March 2005.

[37] T.J.E Miller, "Brushless Permanent-Magnet and Reluctance Motor Drives" Oxford University Press Inc., New York, 1989.

[38] D.C Hanselmam, "Brushless Permanent-Magnet Motor Design," McGraw-Hill, Inc., New York, 1994.

[39] L Xu, L. Ye, L Zhen and A. El-Antably "A New Design Concept of Permanent-Magnet Machine for Flux Weakening Operation," *IEEE Trans. Ind. App.*, Vol. 31, no. 2, pp. 373-378, Mar/Apr. 1995.

[40] T. Sebastian, "Temperature Effects on Torque Production and Efficiency of PM Motors Using NdFeB Magnets," *IEEE Trans. Ind. Appl.*, Vol. 31, no. 2, pp. 353-357, Mar/Apr. 1995.

[41] R.F. Schiferl and T.A Lipo, "Power Capability of Salient Pole Permanent Magnet Synchronous Motor in Variable Speed drive and Application", *IEEE Trans. Ind. Appl.*, Vol. 26, no. 1, pp. 115-123, Jan/Feb. 1990.

[42] T. Sebastian and G.R Slemon, "Operating Limits of Inverter-Drive Permanent-Magnet Motor Drives", *IEEE Trans. Ind. Appl.*, Vol. IA 23, no.2. pp. 327-333, Mar./Apr. 1987.

[43] D. Staton, A. Boglietti and A. Cavagnino, "Solving the More Difficult Aspects of Electric Motor Thermal Analysis," *IEEE Trans. Energy Conv.,* Vol. 20, no. 3 pp. 620-628, Sep. 2005.

[44] J.F. Gieras, "Analytical Approach to Cogging Torque Calculation on PM Brushless Motors," *IEEE Trans. Ind. Appl.*, Vol. 31, no. 2, pp. 353-357, Mar/Apr. 1995.

[45] B. Sneyers, D.W. Novotny and T.A. Lipo "Field weakening in Buried Permanent Magnet AC motor Drives" *IEEE Trans. Ind. Appl.*, Vol. IA-21, no. 2, pp. 353-357, Mar/Apr. 1985.